

Expansion Microscopy: Scalable and Multiplexed Nanoscale Imaging

by

Fei Chen

B.S. Electrical Engineering
California Institute of Technology, 2011

Submitted to the Department of Biological Engineering
in Partial Fulfillment of the Requirements for the Degree of

Doctor of Philosophy in Biological Engineering

at the

Massachusetts Institute of Technology
February 2017

© 2017 Massachusetts Institute of Technology. All rights reserved.

Signature redacted

Signature of author _____

Department of Biological Engineering
February 22, 2017

Signature redacted

Certified by _____

Edward S. Boyden
Professor of Biological Engineering, Brain and Cognitive Sciences, Media Arts and Sciences
Thesis Supervisor

Signature redacted

Accepted by _____

Mark Bathe
Professor of Biological Engineering
Chair, Graduate Program Committee



ARCHIVES

Thesis Committee Members

Peter T. C. So, Ph.D.

Professor of Biological Engineering and Mechanical Engineering
Thesis Committee Chair

Scott R. Manalis, Ph.D.

Professor of Biological Engineering and Mechanical Engineering
Thesis Committee Member

Edward S. Boyden, Ph.D.

Professor of Biological Engineering, Brain and Cognitive Sciences, Media Arts and Sciences
Thesis Supervisor

Table of Contents

ABSTRACT.....	1
ACKNOWLEDGEMENTS.....	2
CHAPTER ONE: INTRODUCTION.....	4
SUPER-RESOLUTION MICROSCOPY.....	4
EXPANSION MICROSCOPY.....	5
CITATIONS TO PUBLISHED WORK AND ACKNOWLEDGEMENTS TO CO-AUTHORS	8
CHAPTER TWO: EXPANSION MICROSCOPY, A SCALABLE SUPER-RESOLUTION MICROSCOPY PLATFORM	9
INTRODUCTION.....	9
RESULTS.....	9
DISCUSSION	12
FIGURES.....	14
<i>Figure 1-1: Expansion microscopy (ExM) concept.</i>	14
<i>Figure 1-2: Expansion microscopy physically magnifies with nanoscale isotropy, enabling super-resolution imaging on diffraction-limited microscopes.</i>	15
<i>Figure 1-3: Super-resolution imaging of synapses and neurons in intact mammalian brain tissue using ExM.</i> 17	
<i>Figure 1-4: Scalable 3D super-resolution microscopy of mouse brain tissue.</i>	19
SUPPLEMENTARY INFORMATION	20
METHODS	28
<i>Labels for ExM:</i>	28
<i>Cultured cell preparation and staining:</i>	28
<i>Brain tissue preparation and staining:</i>	29
<i>In situ polymer synthesis:</i>	29
<i>Digestion and expansion:</i>	30
<i>Optical clearing measurements:</i>	31
CHAPTER THREE: PROTEIN RETENTION EXPANSION MICROSCOPY	34
INTRODUCTION.....	34
RESULTS.....	34
DISCUSSION	38
FIGURES.....	40
<i>Figure 3-1. Post-expansion antibody delivery, after epitope-preserving homogenization</i>	40
<i>Figure 3-2. Retention of fluorescent protein (FP) and antibody fluorescence signals in proExM and proExM of FP fusions.</i>	42
<i>Figure 3-3. Validation of proExM in different mammalian tissue types</i>	44
<i>Figure 3-4. proExM of mammalian brain circuitry.</i>	46
<i>Figure 3-5. Workflows for expansion microscopy with protein retention.</i>	48
SUPPLEMENTARY INFORMATION	49
METHODS	64
CHAPTER FOUR: NANOSCALE IMAGING OF RNA WITH EXPANSION MICROSCOPY	71

INTRODUCTION.....	71
RESULTS.....	71
DISCUSSION.....	75
FIGURES.....	77
<i>Figure 4-1. Design and validation of ExFISH chemistry.</i>	77
<i>Figure 4-2. Serially hybridized and multiplexed ExFISH.</i>	78
<i>Figure 4-3. Nanoscale imaging of RNA in mammalian brain.</i>	79
SUPPLEMENTARY INFORMATION	80
METHODS	92
REFERENCES	99

Abstract

Microscopy has facilitated the discovery of many biological insights by optically magnifying small structures in cells and tissues. However, the resolution of optical microscopy is limited by the diffraction of light to ~200-300 nm, comparable or larger to the size of many subcellular structures. In this thesis, we describe a suite of tools based on a novel super-resolution microscopy approach called Expansion microscopy. Expansion microscopy (ExM) physically expands tissues so that the resolution of ordinary microscopes is increased ~5 times by leveraging the swelling properties of polyelectrolyte hydrogels. Ordinary microscopes used with ExM are more accessible and faster than the specialized optical systems designed to image beyond the diffraction limit (e.g., STORM/PALM, STED, SIM), while yielding similar performance. Expanded tissues are also optically clear, allowing for unprecedented super-resolution imaging in thick tissues and facile reagent diffusion into the sample.

We have since developed a variant of ExM, called protein retention ExM, in which proteins are directly anchored to the swellable gel using a commercially available cross-linking molecule. This strategy enables ExM of genetically encoded fluorescent proteins and commercial fluorescently labeled secondary antibodies. With these advancements, ExM can be carried out with purely commercial reagents and represents a simple extension of standard histological methods used to prepare samples for imaging.

Furthermore, we have developed a variant of the ExM technology that enables RNA molecules to be directly linked to the ExM gel network via a small molecule linker and isotropic expansion. This technology, termed ExFISH, enables visualization of RNAs with nanoscale precision and single molecule resolution. We have demonstrated that the covalent anchoring of RNA also enables robust repeated washing and probe hybridization steps, opening the door to combinatorial multiplexing strategies. By leveraging these benefits, we have further developed *in situ* analysis tools which allow for highly multiplexed imaging of RNA identity and location with nanoscale precision in intact tissues.

Taken together, these tools allow for spatially mapping molecular information onto cell types and tissue structures which could be invaluable for spatially complex biological processes such as brain function, cancer heterogeneity and organismal development.

Acknowledgements

To start, I would like to thank my advisor, Ed Boyden. Ed is, to quote Lin-Manuel Miranda, nonstop; he is truly one of the most dedicated scientists I know, both to his science, but also to his students and trainees. Ed has taught me how to think critically about scientific problems, opened my eyes with his unique approach to technology development, and has also given me great insight into the qualities of the type of mentor and advisor that I aspire to be.

I am deeply grateful for my thesis committee, Peter So and Scott Manalis, who have both been supportive of my research from the beginning. Peter is always upbeat and has provided invaluable guidance on microscopy. I'm grateful for all the advice and intellectual discussion with Scott over the years, and I look forward to the opportunity of potentially embarking on future projects.

I am also thankful for George Church, who has been a mentor to me since we started our close collaboration on *in situ* sequencing and provided valuable advice and inspiration in the past couple of years. Arjun Raj has been a great collaborator and provided invaluable advice on FISH experiments and was kind enough to let us shadow his lab to debug our FISH experiments. I also want to thank Mark Bathe and Peng Yin for helpful discussions and collaborations in work I did earlier in my Ph.D.

I will be forever grateful to the mentors who have shaped my path in science. Going back to high school, I am especially thankful for Hector Morales, who inspired my love for math and science, and put up with my antics. At Caltech, Glen George taught me most of what I know about electrical engineering. During the summer after my freshman year at college, I was lucky to be part of an amazing IGEM team led by Christina Smolke, an experience that spurred my interest in biological engineering. Niles Pierce and Richard Murray brought me into the world of DNA nanotechnology, which has proven to be a great foundation to explore other problems in biological engineering. In my undergraduate years, I was mentored by Harry Choi, who not only showed me how to be a good experimental scientist, but who also became a great friend and has since then provided invaluable advice in life.

For the past 5 years, the Boyden lab has become a second home to me. I am thankful to have such bright and kind individuals to call my peers, co-conspirators, and friends. Daniel Schmidt and Yongku Cho were the first to introduce me to the Boyden lab and graciously took the time to train me. As they have launched their own independent careers, I have missed their presence and camaraderie in the lab, but am gladdened by their successes and willingness to give advice whenever needed.

Developing and augmenting the Expansion Microscopy (ExM) technology was an undeniable highlight of my Ph.D.; it would not have been possible without my co-inventor Paul Tillberg, who took a seemingly crazy idea from inception to a reality with me. Oz Wassie and Shahar Alon have

been an indispensable team through the ups and downs of figuring out how to apply ExM in situ; I count myself truly lucky to have such dedicated and perseverant partners.

Science does not happen in a vacuum, and I would like to thank the many collaborators who have made the development of our work possible both in and out of the lab—in particular, Kiryl Piatkevich, Evan Daugharthy, Allison Cote, Jae-Byum Chang, Yongxin Zhao, Andrew Payne, Sam Rodrigues, Dan Goodwin, Anu Sinha, Jay Yu, and Shoh Asano.

The core facilities at MIT have greatly facilitated my work; in particular, I would like to thank Koli Taghizadeh at the Center for Environmental and Health Sciences for her expertise on HPLC and Wendy Salmon and the Keck Imaging facility at the Whitehead Institute for all her help and discussions in microscopy.

I am grateful to the following friends and colleagues who have kept me active both mentally and physically—Jonathan Gootenberg and Omar Abudayeh for the chats over coffee, the Boyden Ball (Z) team for discussions on and off the court, and Adam Marblestone for being always available to bounce off ideas, theories, and the construction of any phrases I needed help with writing.

Since we've met in 2010, Allen Lin has been a close friend and partner-in-crime for all things science and otherwise. He has enabled me to break down doors, both literally and figuratively, for the sake of friendship and scientific inquiry. Mark Scott is a remarkable scientist and a kindred spirit in engineering, board games, and moving escapades. It has been an honor to share in the little moments and big occasions of life with you.

I would like to thank my friends in the MIT graduate departments: Nikita Pak, Alec Nielsen, Thomas Segall-Shapiro, Vyas Ramanan, Noah Jakimo, Brian Allen, and others for making this experience memorable and fun along the way.

I'm eternally grateful for my parents, Sufang Yang and Dexi Chen — your love and sacrifice has meant the world to me.

Finally, I dedicate this thesis to my loving wife, Debbie, who means the world to me. You have been ever by my side these last 5 years, full of patience and support and taught me the meaning of love and dedication. Here's to our future adventures...

Chapter One: Introduction

Super-resolution Microscopy

Fluorescence microscopy, through EGFP fusion proteins and indirect immunofluorescence is a fundamental technology for biologists. However, the diffraction limit of light prevents interrogation of cellular structures with traditional fluorescence microscopy less than 250 nm¹. Structure in biology beyond the diffraction limit of light is ubiquitous; almost all subcellular compartments are beyond the diffraction limit. In particular, in neuroscience, sub-cellular structures are highly important. Subcellular compartments of neurons such as presynaptic terminals, postsynaptic spines, and intracellular organelles have highly intricate distributions of biomolecules. The average synaptic active zone diameter is ~300 nm, i.e. at the diffraction limit, thus, any sub-synaptic structure cannot be accessed with diffraction limited microscopy². In presynaptic terminals alone, hundreds of proteins, ranging from scaffolding proteins, to proteins involved with fusing synaptic vesicles to the membrane, to mediators of synaptic plasticity, are localized for functional transmission of neuronal signaling^{3,4}. Furthermore, the shape of axons, dendrites, and spines are clearly important for neuronal function, plasticity and development. Finally, in the brain, at the tissue level, millions of neurons are arranged with nanoscale connectivity.

In the past decade, several new technologies have emerged to allow for optical microscopy below the diffraction limit. These approaches allow for ultrastructural examination of cells and tissues, a realm previously limited to electron microscopy, with light microscopy. Light microscopy has many advantages over electron microscopy which include ease of sample preparation, ease of protein labeling, simultaneous multi-color imaging, and compatibility with *in vivo* imaging.

Current super-resolution microscopy techniques broadly fall into two main classes. First, single molecule localization microscopy techniques (STORM, stochastic optical reconstruction microscopy; PALM: Photo-activated localization microscopy) which utilize different strategies to image a sparse sub-set of fluorophores to collect and fit statistics about the localization of single fluorophores^{5,6}. STORM can achieve 20 nm lateral and 60 nm axial resolutions, and in the best cases less than 5 nm lateral resolution^{7,8}. However, the high SNR requirements for single molecule localization requires often requires the use of TIRF and specialized EMCCD cameras. Furthermore, by temporally spacing out single fluorophore emissions, acquisitions can be up to 40 minutes per image for the highest resolution images⁸.

Second, techniques which sculpt the illumination light to obtain higher spatial frequency information. In structured illumination microscopy (SIM), a factor of two resolution improvement

can be achieved by spatially mixing a structured illumination pattern to bring the high-frequency information into the pass-band of the microscopy⁹. In STED (Stimulated Emission Depletion) and RESOLFT (Reversible Saturable Optical Fluorescence Transitions) a subdiffraction limited excitation spot can be generated with a de-excitation donut through either stimulated emission or photoswitchable fluorophores¹⁰⁻¹⁴. Typically achievable resolutions range from 50 nm laterally. Due to their point-scanning nature STED and RESOLFT can achieve much faster imaging speeds than STORM/PALM. STED and RESOLFT both require specialized optics for the generation of the de-excitation donut, and, furthermore, STED requires very powerful lasers to enable de-excitation through stimulated emission. RESOLFT imposes less optical limitations, however, it requires specialized photoswitchable fluorophores¹⁵. Both STED/RESOLFT and SIM are limited in imaging depth due to short working distance high NA objectives, and the detrimental effects of tissue scattering on the fidelity of the structured illumination patterns.

Expansion Microscopy

Given the current limitations of super-resolution imaging technologies, we reasoned the development of a simple, inexpensive, and easy-to-use methodology that enables nanoscale resolution imaging of fixed cells and tissues which will allow 3D large volume reconstructions would be an invaluable addition to the available tool set of super-resolution microscopy. Furthermore, by approaching the problem from a sample modification, as opposed from an optical engineering, standpoint, we allow the technology to be easily adopted for traditional, widely accessible diffraction limited microscopes.

In chapter two, we describe the approach we developed, Expansion Microscopy (ExM), to achieve super-resolution microscopy through transferring biological structure information to an expandable hydrogel while preserving relative spatial information. While there are many different classes of expandable hydrogels in the literature, which span the gamut of polymer composition and expansion mechanism, in this work we will focus on hydrogels composed of co-polymers of polyacrylate and polyacrylamide.

Poly-acrylate have many advantageous characteristics for our application. Acrylate is the simplest carboxylic acid acrylic monomer, and the expansion characteristics of poly-acrylate gels are well documented¹⁶. The expansion of polyacrylate hydrogels is toggled by salt, and the gel exhibits a remarkable ability to absorb water, allowing the hydrogel to increase >100 times in volume.

We utilize hydrogels formed via free radical polymerization of acrylate monomers and crosslinker (bis-acrylamide) along with an acrylamide co-monomer. We found that the acrylamide increases the mechanical strength of the gel. We perform *in situ* polymerization by first allowing small molecule monomers and crosslinkers to permeate the biological sample, thereby forming a composite network of hydrogel and the fixed biomolecules within the biological specimen. This

approach has been demonstrated more than 20 years previously and, in addition, was separately developed in parallel for clearing based technologies while ExM was being developed^{17,18}.

In our initial exploration of swelling of fixed biological samples with *in situ* polymerized acrylate gels, we found that the gel swelling does expand and preserve biological features, but the heterogeneous nature of the hydrogel/biological sample composite leads to anisotropic expansion and artifacts. We reasoned that these artifacts are due to the mechanical heterogeneity of the hydrogel/tissue composite, as there is a chemically cross-linked biological network which interpenetrates the hydrogel. Thus, we engineered a solution to this heterogeneity by chemically anchoring the structural information of interest into the hydrogel and destroying the underlying biological network. To do so, we have developed a method to anchor fluorophores from immunostaining into the gel network during polymerization, following which the biological network is destroyed by a combination of chaotropic agents, detergents and Proteinase K, a potent and nonspecific proteolytic enzyme.

This strategy of transferring biological molecules onto the ExM hydrogel, followed by disruption of the biological structure has been generalized throughout this work. This transfer is facilitated by DNA-conjugated antibodies in Chapter Two, wherein gel-anchorable trifunctional labels consisting of a fluorophore, a binding site, and the gel anchorable moiety is synthesized via custom-oligonucleotide synthesis. This approach allowed us to rapidly prototype anchoring chemistries as well as demonstrate the feasibility of the ExM strategy.

However, these custom labels requires end-users to carry out conjugation reactions that they may not be familiar with and also prevents the use of genetically encoded fluorescent proteins (FPs). In Chapter Three, we describe a variant of ExM, called protein retention ExM, in which proteins, rather than labels, are anchored to the swellable gel using a commercially available cross-linking molecule. Using this strategy, we have demonstrated expansion microscopy of cells and tissues with retention of signals from genetically encoded fluorescent proteins and commercial fluorescently labeled secondary antibodies. With these advancements, expansion microscopy can be carried out with purely commercial reagents and represents a simple extension of standard histological methods used to prepare samples for imaging.

In addition to anchoring proteins to the expandable gel matrix, in Chapter Four, I outline approaches to specifically anchor nucleic acids, so that DNA and RNA molecules can be expanded with high yield and spatial fidelity (**Fig. 2A**). The expanded environment is 99% water, and the proteolytic digestion of ExM isolates the anchored nucleic acids in a quasi-*in vitro* environment. Furthermore, the ability to surround biomolecules with pure, user-specified chemical environments will vastly open up analytical possibilities, converting the difficult *in situ* environment into a more reliable classical biochemical environment that allows for facile reagent exchanges and physical space for signal amplification. More fundamentally, temporal barcoding through iterative imaging of transcripts requires that individual RNAs are spatially resolved, this

rapidly becomes challenging for imaging large panels of many RNAs without the high resolution afforded by ExM.

Combined with improved ExM chemistries for higher resolution and dedicated imaging platforms for expanded specimens, this thesis builds the framework for a multi-modal transcriptomic, genomic, and proteomic ExM toolset which enables holistic mapping of mapping molecular information onto cell types and structures which could be invaluable for understanding complex biological systems

Citations to published work and acknowledgements to co-authors

Collaboration was essential to all of the work described here, and I am pleased to acknowledge the following co-authors for associated publications:

Chapter two appears as: Chen, F.*, Tillberg, P.W.*, Boyden, E.S. (2015) Expansion Microscopy, *Science*.

We would like to acknowledge Wendy Salmon and Eliza Vasile for assistance with confocal and SR-SIM imaging. We would like to acknowledge Nikita Pak for assistance with perfusions. We would also like to acknowledge, for helpful discussions, Brian Chow, Adam Marblestone, George Church, Jae-Byum Chang, Juan Enriquez, Ishan Gupta, Mehran Kardar, and Alex Wissner-Gross.

Chapter three appears as: Tillberg, P.W.*, Chen, F.*, Piatkevich, K.D., Zhao, Y., Yu, C.-C., English, B.P., Gao, L., Martorell, A., Suk, H.-J., Yoshida, F., DeGennaro, E.M., Roossien, D.H., Gong, G., Seneviratne, U., Tannenbaum, S.R., Desimone, R., Cai, D., Boyden, E.S. (2016) Protein-retention expansion microscopy of cells and tissues labeled using standard fluorescent proteins and antibodies, *Nature Biotechnology*.

We'd like to additionally thank Nikita Pak for helping with perfusions. We would like to acknowledge Wendy Salmon and Eliza Vasile for assistance with confocal and SR-SIM imaging. We'd like to acknowledge Jae-Byum Chang, Juan Enriquez, and Asmamaw Wassie for additional discussions.

Chapter four appears as: Chen, F.*, Wassie, A.T.*, Cote, A.J., Sinha, A., Alon, S., Asano, S., Daugharthy, E.R., Chang, J.-B., Marblestone, A., Church, G.M., Raj, A., Boyden, E.S. (2016) Nanoscale Imaging of RNA with Expansion Microscopy, *Nature Methods*.

I'd like to additionally acknowledge Wendy Salmon W.M. Keck Facility for Biological Imaging at Whitehead Institute for Biomedical Research for assistance on lightsheet imaging as well as useful imaging discussions. S. Olenych from Carl Zeiss microscopy provided imaging filters for the lightsheet. I'd also like to thank Harry Choi and Niles Pierce for discussions and advice on HCR design and experiments.

*denotes equal contribution

Chapter Two: Expansion Microscopy, a Scalable Super-resolution Microscopy Platform

Introduction

Microscopy has facilitated the discovery of many biological insights by optically magnifying images of small structures in fixed cells and tissues. Much effort has been invested, accordingly, in the design and implementation of lenses of increasing refracting power and quality. We here report that physical magnification of the specimen itself is possible. Polymerizing electrolyte monomers directly within a sample into an electrically charged polymer network, followed by solvent exchange, results in specimen expansion. By covalently anchoring specific molecules within the specimen to this polymer network and proteolytically digesting endogenous biological structure, we found that samples could be expanded isotropically ~4.5-fold in linear dimension. We discovered that this isotropic expansion applies to nanoscale structures, and thus this method, which we call expansion microscopy (ExM), can effectively separate molecules located within a diffraction limited volume, to distances great enough to be resolved with conventional microscopes. ExM represents a new modality of magnification, and enables scalable, multi-color super-resolution imaging of fixed cells and tissues.

Results

We sought to implement physical magnification by adopting a well-known property of polyelectrolyte gels: dialyzing them in pure water causes expansion of the polymer network into extended conformations (**Fig. 1A**¹⁶). The ExM process starts with chemically fixed and permeabilized brain tissue (**Fig. 1B**), into which we infused sodium acrylate, a monomer commonly used to produce super-absorbent materials (^{19,20}), along with the co-monomer acrylamide and the crosslinker N-N'-methylenebisacrylamide. After triggering *in situ* free radical polymerization with ammonium persulfate (APS) initiator and tetramethylethylenediamine (TEMED) accelerator in the presence of salt, we treated the embedded brain tissue extensively with protease to homogenize the mechanical characteristics of the tissue-polymer composite. Following proteolysis, dialysis of the processed specimen in deionized water resulted in a 4.5-fold linear expansion, without distortion at the level of gross anatomy (**Fig. 1C**). The brain tissue thus expanded through this process is transparent (**Supp. Fig. 1**), since it consists almost entirely of water.

We developed a fluorescent labeling strategy compatible with the proteolytic treatment and subsequent tissue expansion described above. We designed a custom fluorescent label (**Fig. 1D**) that can be incorporated directly into the polymer network. This label is tri-functional, comprising a methacryloyl group capable of participating in free radical polymerization, a chemical fluorophore for visualization, and an oligonucleotide that can hybridize to a complementary

sequence attached to an affinity tag (e.g., a secondary antibody) (**Fig. 1E, 1F**). Thus, the fluorescent tag is targeted to a biomolecule of interest, yet remains anchored covalently to the polymer network throughout the ExM process.

We performed fluorescence imaging using ExM, examining microtubules in fixed HEK293 cells that were labeled with the tri-functional label and imaged with confocal laser scanning microscopy pre- vs. post-ExM processing. The post-ExM image (**Fig. 2B**) was registered to the pre-ExM image (**Fig. 2A**) via a similarity transformation (i.e., only global scaling, rotating, and translating), resulting in visually indistinguishable images. To quantify the isotropy of ExM, we calculated the deformation vector field between the two images via a non-rigid registration process (**Supp. Fig. 2**). From this vector field, we quantified the root-mean-square error of feature measurements post-ExM, and found that for both short and long distances, the errors in length were small (<1% of distance, for errors larger than the imaging system point spread function size) (**Fig. 2C**, $n = 5$ samples). Throughout the paper, all distances measured in the post-expansion specimen are reported divided by the expansion factor (see **Methods**).

We next compared pre-ExM images taken on a conventional super-resolution microscope to post-ExM images taken on a confocal microscope. Specifically, we labeled features traditionally used to characterize the performance of super-resolution microscopes, including microtubules (^{21,22}) and clathrin coated pits ²³, and imaged them with a super-resolution structured illumination microscope (SR-SIM) pre-ExM, and a spinning disk confocal post-ExM. Qualitatively (**Fig. 2D, 2E**), the images were similar, and quantitatively (**Fig. 2I**), measurement errors were again on the order of 1%, and well within the point spread function size of the SR-SIM microscope ($n = 3$ samples). Microtubule networks appeared more sharply resolved in ExM (**Fig. 2G**) than with SR-SIM (**Fig. 2F**). ExM clearly resolved individual microtubules that could not be distinguished with SR-SIM (**Fig. 2H**). Microtubules imaged with ExM presented a full width at half maximum (FWHM; representative microtubule shown in **Fig. 2J**) of 83.6 ± 5.3 nm (mean \pm standard deviation, $n = 24$ microtubules from 3 samples). This FWHM reflects the resolution of ExM convolved by the width of the labeled microtubule. To estimate the resolution of ExM, we deconvolved (as in ²⁴) our observed microtubule FWHM by the known immunostained microtubule width (55 nm ²³), conservatively ignoring the width of the tri-functional label, and obtained a resolution for ExM of ~ 60 nm. This conservative estimate is comparable to the diffraction limited confocal resolution (~ 250 nm lateral resolution ²⁵) divided by the observed expansion factor (~ 4.5).

A comparison of clathrin-coated pits imaged with ExM vs. SR-SIM provides an independent demonstration of the nanoscopic isotropy and high resolution of ExM. Clathrin coated pits were well resolved (**Fig. 2K, 2L**). ExM resolved the central nulls of the pits better than SR-SIM (**Fig. 2M, 2N**). Clathrin-coated pit radii measured via ExM and SR-SIM were highly correlated, with a slope of 1.001 (total least squares regression, confidence interval .013 with $P < 0.05$, $n = 50$ pits from 3 samples) (**Fig. 2O**). 49 of the 50 points lay within a half-pixel distance

of the unity slope $y = x$ line, suggesting that variation in the ExM vs. SR-SIM comparison was within the digitization error of the measurement.

We next applied ExM to fixed intact brain tissue. Slices of brain from Thy1-YFP-H mice²⁶, containing parts of the cortex and hippocampus, were stained with a tri-functional label bearing Alexa 488, using anti-GFP primary antibodies. Slices expanded $\sim 4x$, similar to the expansion factor in cultured cells, suggesting that ExM works similarly in intact tissue. We compared pre- vs. post-ExM images taken on an epifluorescence microscope. As with cultured cells, the post-ExM image (**Fig. 3A**) was registered to the pre-ExM image (**Fig. 3B**) via a similarity transformation. The registered images closely matched, although some features moved in or out of the depth of field, due to the axial expansion post-ExM. Quantitatively, post-ExM measurement errors (**Fig. 3C**, $n = 4$ cortical slices) were between 2 and 4%.

Taking advantage of the modular architecture of the tri-functional label, we synthesized tri-functional labels with different colors and oligonucleotides (see **Methods**), to enable multicolor ExM. We obtained pre- (**Fig. 3D**) vs. post-ExM (**Fig. 3E**) images of Thy1-YFP-H mouse cortex with ExM labels directed against YFP (green) and the pre- and post-synaptic scaffolding proteins Bassoon (blue) and Homer1 (red). In the pre-ExM image, Bassoon and Homer1 staining form overlapping spots at each synapse (**Fig. 3F**) without resolvable structure, while the post-ExM image (**Fig. 3G**) shows clearly distinguishable pre- and post-synaptic labeling, and greater detail in synaptic structure. A previous study imaged synapses in intact mouse brain tissue, using STORM microscopy, and obtained a distance between Bassoon and Homer1 synaptic scaffolds (in the mouse ventral cortex and the olfactory bulb) of ~ 150 nm²⁷. We quantified the distance between the Bassoon and Homer1 scaffolds, as measured by ExM. We fit the distributions of Bassoon and Homer1 staining intensity, taken along the line perpendicular to the synaptic cleft (**Fig. 3H**, boxed region), to Gaussian distributions (**Fig. 3I**). The Bassoon-Homer1 separation, calculated as the difference between the means for the Gaussian distributions of each color, was 169 ± 32.6 nm (**Fig. 3J**, $n = 277$ synapses from 4 cortical slices), similar to the previous results obtained via STORM.

To explore whether expanded samples, scanned on fast diffraction limited microscopes, could support scalable super-resolution imaging, we imaged a volume of the adult Thy1-YFP-H mouse brain spanning $500 \mu\text{m} \times 180 \mu\text{m} \times 100 \mu\text{m}$, with three labels (**Fig. 4A**; anti-GFP, green; anti-Homer1, red; anti-Bassoon, blue). The diffraction limit of our confocal spinning disk microscope (with 40x, 1.15 NA, water immersion objective), divided by the expansion factor, yields an estimated resolution of ~ 70 nm laterally and ~ 200 nm axially. Shown in **Fig. 4A** is a 3D rendered image of the whole dataset (see **Supp. Movie 1** for animated rendering); zooming into regions of interest within the raw dataset, nanoscale features emerge (**Fig. 4B-D**). For example, we performed a volume rendering of the YFP-expressing neurons in a subset of CA1 stratum lacunosum moleculare (slm), revealing detailed spine morphology (**Fig. 4B** and **Supp. Movie 2**). Focusing on a representative dendrite in CA1 slm, we observed the post-synaptic protein Homer1 to be well localized to dendritic spine heads, with the presynaptic molecule Bassoon in close

apposition (**Fig. 4C** and **Supp. Movie 3**). Examination of a mossy fiber bouton in the hilus of the dentate gyrus reveals the fine structure of invaginations into the bouton by spiny excrescences of the opposing dendrite, as observed previously via electron microscopy²⁸ (**Fig. 4D** and **Supp. Movie 4**). Pre-synaptic Bassoon and post-synaptic Homer1 are visible within and adjacent to the bouton, respectively, as expected. Thus, ExM enables multiscale imaging and visualization of nanoscale features, but across length scales relevant to understanding large-scale neural circuits.

Discussion

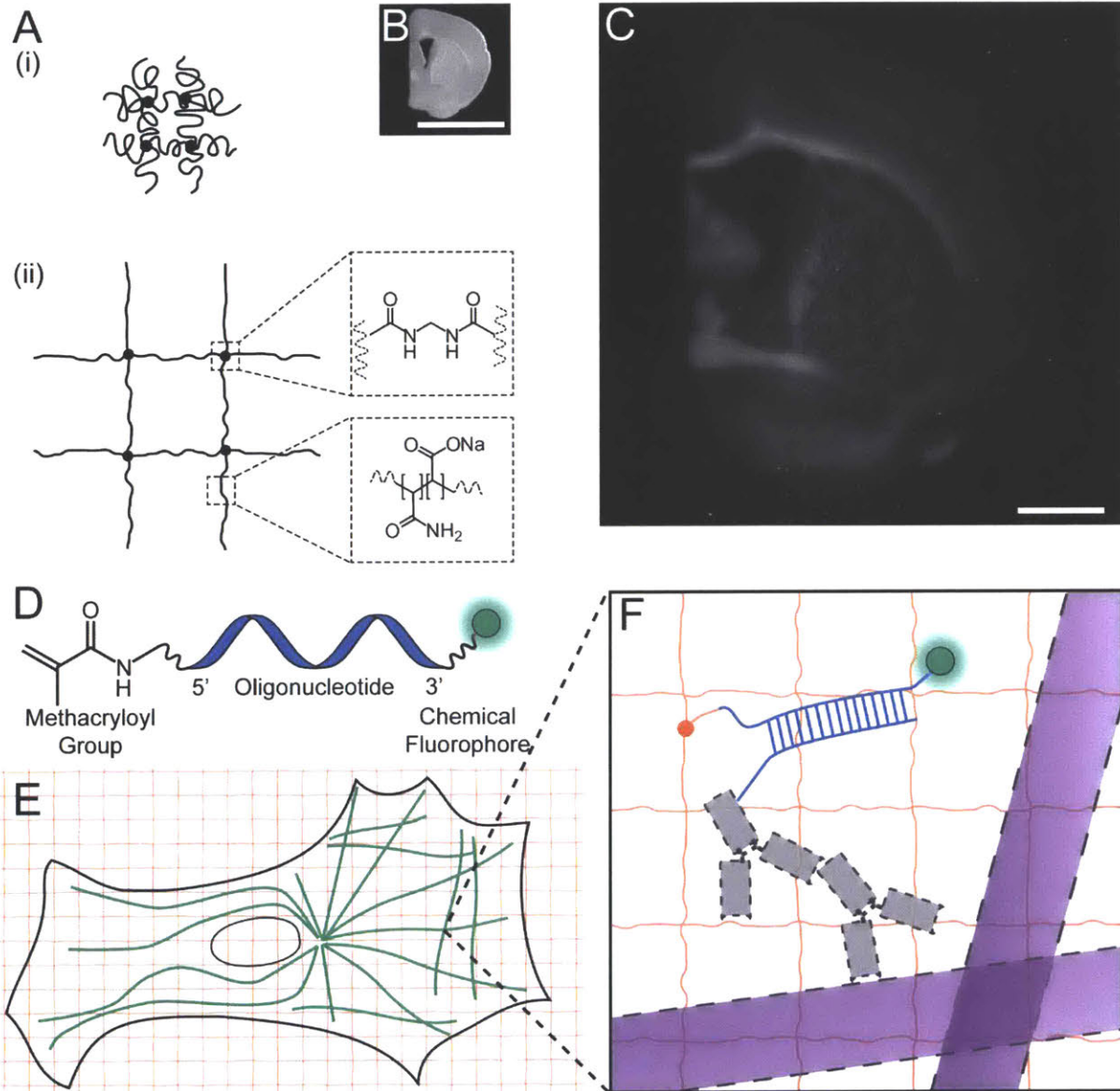
In summary, we report the discovery that fixed cells and tissues can be physically magnified, with isotropic nanoscale resolution (~ 60 nm lateral resolution), through *in situ* polymer synthesis and chemically driven polymer swelling. We achieved roughly two orders of magnitude of volumetric expansion, facilitated by anchoring fluorescent tags to the polymer network, followed by disruption of endogenous biomolecular structures to homogenize the mechanical properties of the sample. We discovered that ExM preserves nanoscale features through multiple independent comparisons, including before-and-after comparisons of stereotyped features, as well as comparisons to SR-SIM microscopy.

Super-resolution imaging methods are slower than their diffraction limited counterparts because they must resolve more voxels per unit volume. ExM achieves this effect by expanding the voxels physically. The speed of voxel acquisition compares favorably to other high-speed super-resolution methods such as parallel RESOLFT¹³. The physical magnification of ExM, however, enables super-resolution imaging with several fundamental new properties. The expansion is isotropic, meaning that axial resolution is improved by the same factor as lateral resolution. Because the magnification is not dependent on the fluorophores involved, ExM can achieve super-resolution with multiple standard fluorophores, on a diffraction-limited microscope. Super-resolution imaging is often performed within ~ 10 μm of the sample surface due to low signal-to-noise, scattering and refractive index mismatch. Here, we demonstrated 3-color super-resolution imaging of a large volume of brain tissue over an axial extent of 100 μm with a standard spinning disk confocal microscope. Because the ExM-processed sample is almost entirely made of water, eliminating scattering, ExM may empower very fast imaging methods like light sheet fluorescence microscopy²⁹ to become super-resolution methods. Since the sample is physically larger, any mechanical errors in post-expansion sectioning, microscope stage movement, thermal drift, and other sources of measurement error, are effectively divided by the expansion factor, making the microscopy more robust.

Although acrylate esters have been used as components of antigen-preserving embedding resins for electron microscopy^(30, 31), ExM represents the first use of an embedded polyelectrolyte gel, used here to expand the specimen. The fundamental resolution of ExM is likely a complex function of physical parameters such as the spatial density of cross-links of the polymer. The high performance of ExM suggests that despite statistical fluctuations in polymer chain length at the

molecular scale, at the nanoscale distances here examined, these fluctuations average out, yielding the observed isotropy. By tuning the materials used for ExM, yet higher resolutions may be possible, as well as further degrees of expansion.

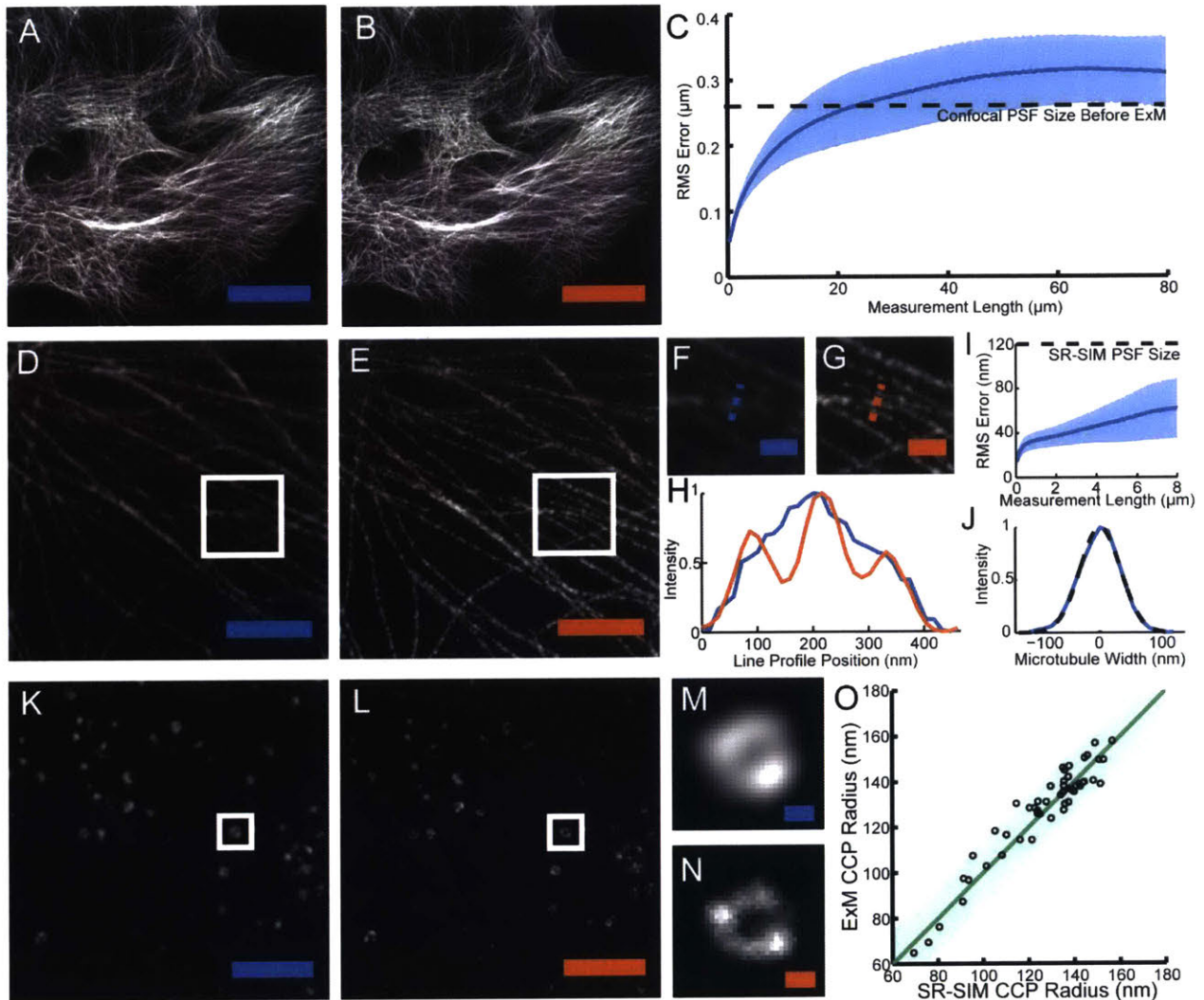
Figure 1-1: Expansion microscopy (ExM) concept.



(A) Schematic representation of a collapsed polyelectrolyte polymer network (i) in high salt, showing crosslinker (dot) and polymer chain (line), and expanded polymer network (ii) after dialysis with H₂O. (B) Photograph of a fixed mouse brain tissue section. (C) Photograph of the tissue of (B), after ExM, under intense side illumination. (D) Schematic of fluorescent label that can be targeted to a biomolecule, anchored to the gel, and retained after protein digestion. (E) Schematic of antibody stained microtubules (green) embedded within the polymer network (orange). Oligonucleotide labels as in (D) are hybridized to complementary oligonucleotides

covalently attached to secondary antibodies and incorporated during gel synthesis. (F) Fluorophores (green) introduced via the DNA label of (D), and hybridized (blue) to the oligo-bearing secondary antibody bound via the primary antibody (gray) to the microtubules (purple), are incorporated into the gel (orange lines) via the methacryloyl group (orange dot) and remain after digestion of all proteins (dotted lines). Scale bars: (B), (C) 5 mm.

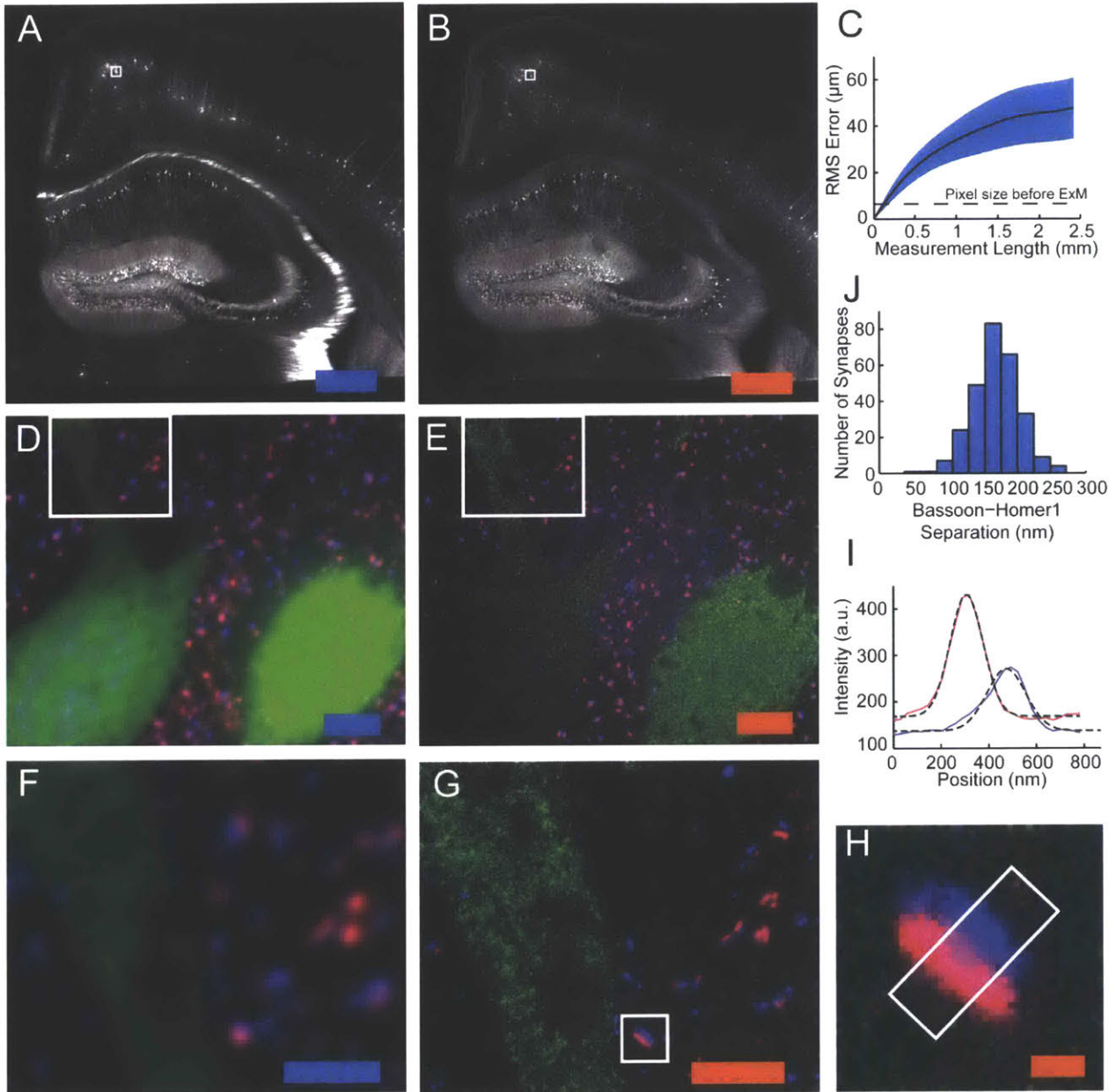
Figure 1-2: Expansion microscopy physically magnifies with nanoscale isotropy, enabling super-resolution imaging on diffraction-limited microscopes.



Throughout this figure, we compared images acquired via a conventional microscopy method (blue scale bars), vs. images acquired post-expansion (orange scale bars). (A), (B) Laser scanning confocal microscopy (LSM) image of microtubules (40x, 1.30 NA) (A) and post-expansion LSM image of the same sample (20x, 0.8 NA) (B). (A) and (B) are maximum intensity projections (MIPs) of 1.5 μm thickness (in pre-ExM distance units). (C) Root-mean-square (RMS) length measurement error of pre- vs. post-ExM confocal images of cultured cells (blue line, mean; shaded

area, standard deviation; $n = 5$ samples). **(D)**, **(E)** Super-resolution structured illumination microscopy (SR-SIM) image of immunostained microtubules **(D)** (100x, 1.40 NA used here and throughout the rest of this figure), and post-expansion image of the same sample taken on a spinning disk confocal **(E)**. **(D)** and **(E)** are MIPs of 1 μm thickness (in pre-ExM distance units). **(F)**, **(G)** Magnified views of boxed regions of **(D)** and **(E)** respectively. **(H)** Profiles of microtubule intensity taken along the blue and orange dotted lines in **(F)** and **(G)**, and plotted using the same colors, demonstrating ExM resolution vs. SR-SIM resolution. **(I)** RMS length measurement error of ExM vs. SR-SIM images (blue line, mean; shaded area, standard deviation; $n = 5$ samples). **(J)** Line profile of the width of a representative microtubule (blue line), with Gaussian fit (black dotted line). **(K)**, **(L)** SR-SIM image of immunostained clathrin coated pits (CCPs) **(K)**, and post-expansion image of the same sample imaged with spinning disk confocal **(L)**. **(K)** and **(L)** are MIPs of 500 nm thickness (in pre-ExM distance units). **(M)**, **(N)** Magnified views of a single CCP in the boxed regions of **(K)** and **(L)** respectively. The SR-SIM image **(M)** is depicted interpolated such that the pixel size is the same as that of the ExM image **(N)**. **(O)** Scatterplot of radii of individual CCPs measured via angular averaging of the radial intensity profile. The CCP radius measured from the ExM image is plotted against the radius measurement in SR-SIM. The green line represents the line $y = x$, and the shaded green region represents half-pixel width of digitization error in both x and y . Scale bars for pre- vs. post-ExM images: **(A)** 20 μm , **(B)** 20 μm (physical size post-expansion, 81.6 μm); **(D)** 2 μm , **(E)** 2 μm (9.1 μm); **(F)** 500 nm, **(G)** 500 nm (2.27 μm); **(K)** 2 μm , **(L)** 2 μm (8.82 μm); **(M)** 100 nm, **(N)** 100 nm (441 nm).

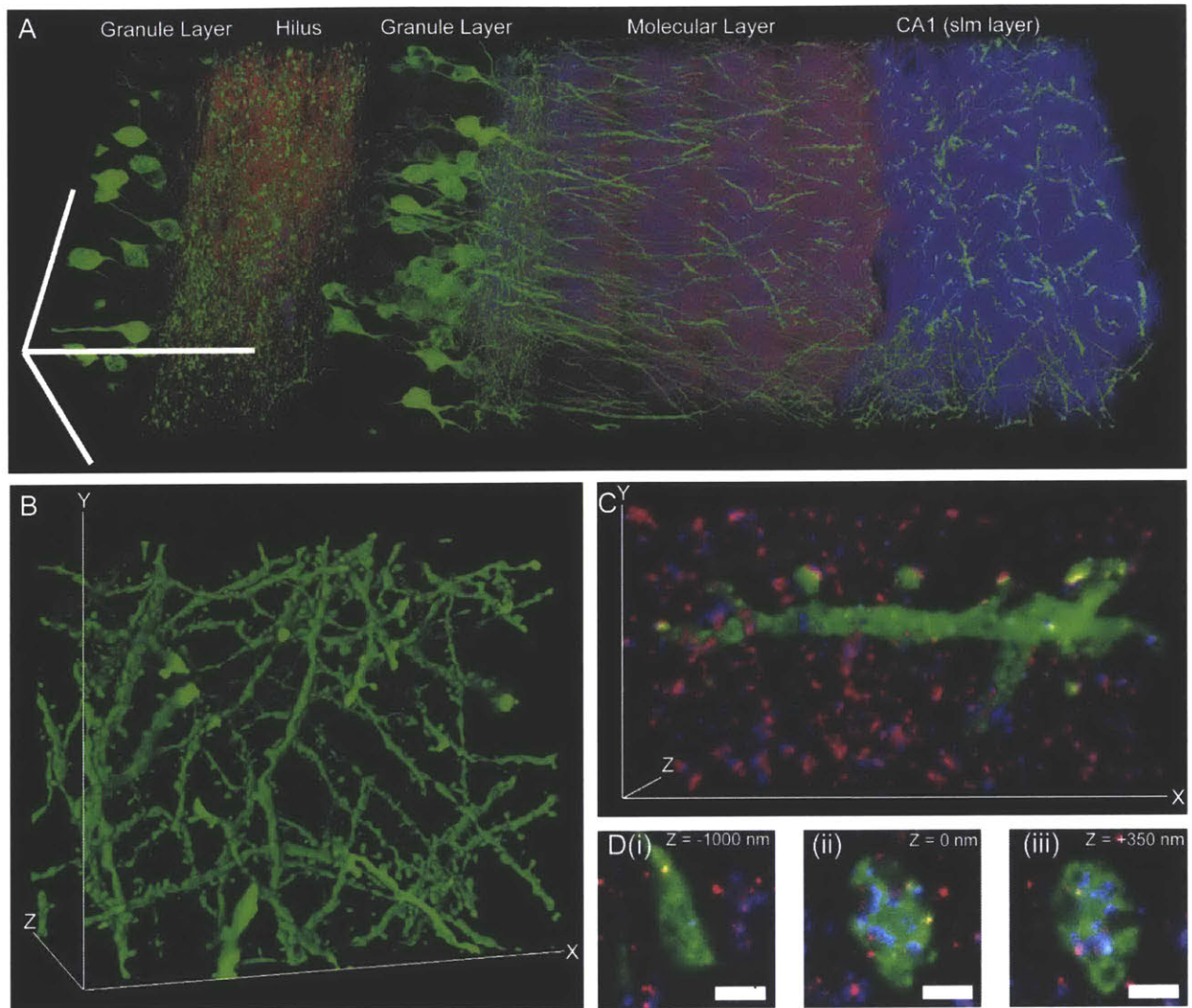
Figure 1-3: Super-resolution imaging of synapses and neurons in intact mammalian brain tissue using ExM.



(A), (B) Widefield fluorescence images of Thy1-YFP mouse brain (e.g., cortex and hippocampus), showing anti-GFP staining (white) pre- **(A)** vs. post- **(B)** expansion (4x, 0.13 NA used for both of these panels). **(C)** Root-mean-square (RMS) length measurement error for pre- vs. post-ExM images of brain slices (blue line, mean; shaded area, standard deviation; $n = 4$ samples). **(D), (E)** Confocal fluorescence images of boxed regions in **(A)** and **(B)** respectively, stained with pre-synaptic (anti-Bassoon, blue) and post-synaptic (anti-Homer1, red) markers, in addition to anti-GFP (green), pre- **(D)** vs. post- **(E)** expansion (40x, water immersion, 1.15NA used for both of these panels, and throughout the rest of the figure). **(E)** is a maximum intensity projection of 4-z

slices chosen to match the axial extent in **(D)** as closely as possible. **(F)**, **(G)** Details of boxed regions in **(D)** and **(E)**. **(G)** is a maximum intensity projection of 4 z-slices chosen to match the axial extent in **(F)** as closely as possible. **(H)** Detail of single representative synapse highlighted in **(G)**. **(H)** is a single z-slice. **(I)** Staining intensity of the synapse of **(H)** as a function of position along the long axis of the white boxed region in **(H)** for Bassoon (blue) and Homer1 (red). Gaussian fits to these plots are included as dotted black lines. a.u., arbitrary units. **(J)** Bassoon-Homer1 separation ($n = 277$ synapses from 4 cortical slices), calculated from the means of their respective Gaussian fits. Scale bars for pre vs. post-ExM images: **(A)** 500 μm , **(B)** 500 μm (physical size post-expansion 2.01 mm); **(D)** 5 μm , **(E)** 5 μm (20.1 μm); **(F)** 2.5 μm , **(G)** 2.5 μm (10.0 μm) and **(H)** 250 nm (1.00 μm).

Figure 1-4: Scalable 3D super-resolution microscopy of mouse brain tissue.



(A) Volume rendering of a portion of hippocampus showing neurons (expressing Thy1-YFP, shown in green) and synapses (marked with antibodies against Bassoon (blue) and Homer1 (red)), with regions named at top. The 3D rendering is downsampled 8-fold from the acquired resolution. **(B)** Volume rendering of neurites in CA1 stratum lacunosum moleculare (slm) showing dendrites, and spines. **(C)** Volume rendering of representative dendritic branch in the slm of hippocampal area CA1. **(D)** Close-up of a mossy fiber bouton in the hilus of the dentate gyrus. Panels (i-iii) represent selected z-slices of the bouton showing its morphology and associated synapses. Scale bars: **(A)** 100 μm in each dimension; **(B)** 52.7 μm (x), 42.5 μm (y), and 35.2 μm (z); **(C)** 13.5 μm (x), 7.3 μm (y), and 2.8 μm (z); **(D)** (i-iii) 1 μm .

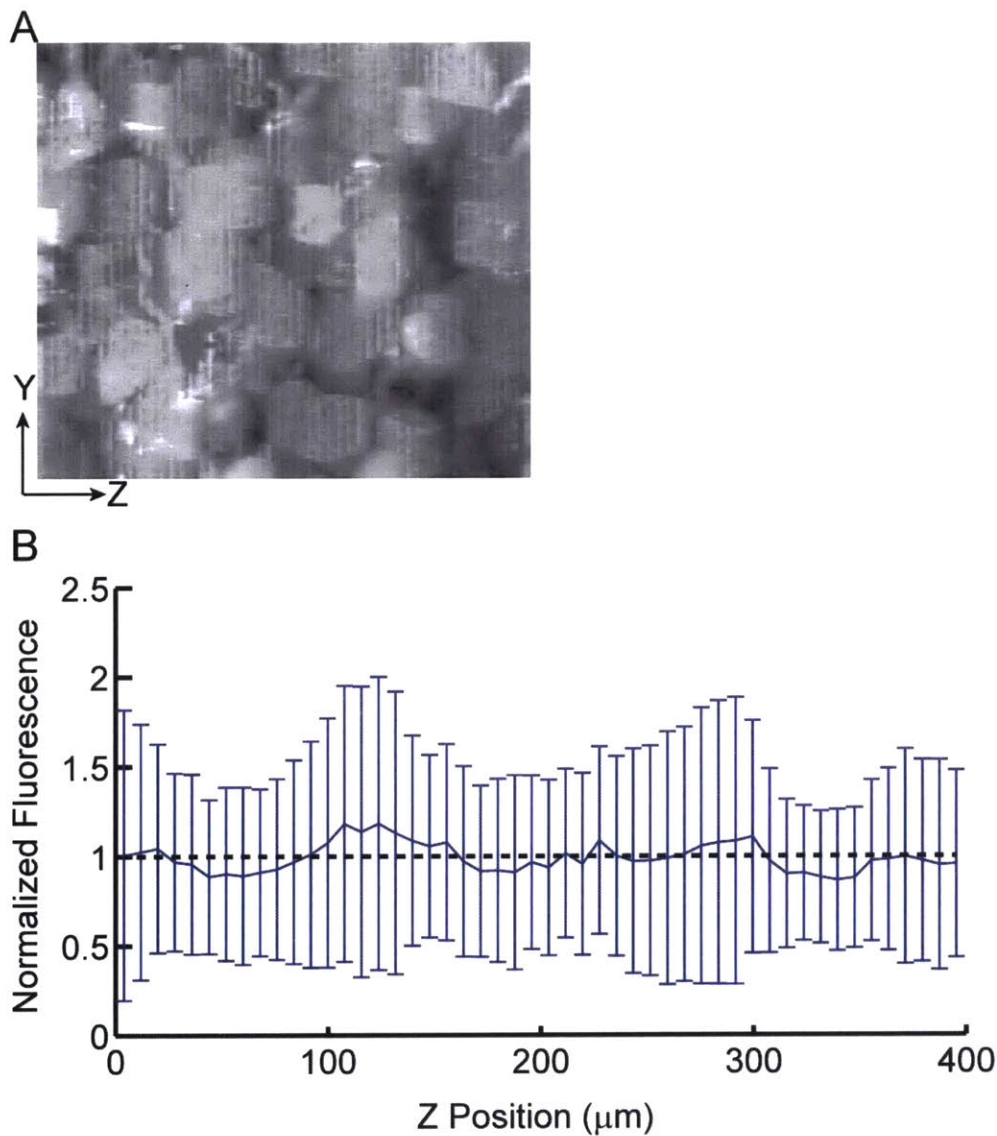


Figure S1. Residual YFP fluorescence as a function of depth in the slice, after digestion and expansion. Proteolysis during the ExM process significantly reduces endogenous YFP fluorescence in expanded samples of Thy1-YFP mouse brain. The residual YFP fluorescence can thus be imaged as a proxy for proteolytic homogeneity. **(A)** Maximum intensity projection in the X dimension of 25 Z stacks of pyramidal cells in the cortex of Thy1-YFP-H brain slices after overnight digestion and subsequent expansion, and processed to exclude high-brightness nuclei and background as described in the **Methods**. The length in the Z dimension is 400 μm in post-expanded units (almost all of the thickness of the 100 μm slice after $\sim 4.5\times$ expansion). **(B)** Mean fluorescence intensity across the stacks of **(A)**, normalized by overall mean fluorescence, plotted as a function of Z. Error bars, mean-normalized stack-to-stack standard deviation ($n = 25$ Z

stacks, 2 brain slices). Dotted line, visual reference for fluorescence equal to the mean. The lack of systematic variation of YFP fluorescence vs. depth demonstrates the uniformity of proteolytic digestion throughout the slice.

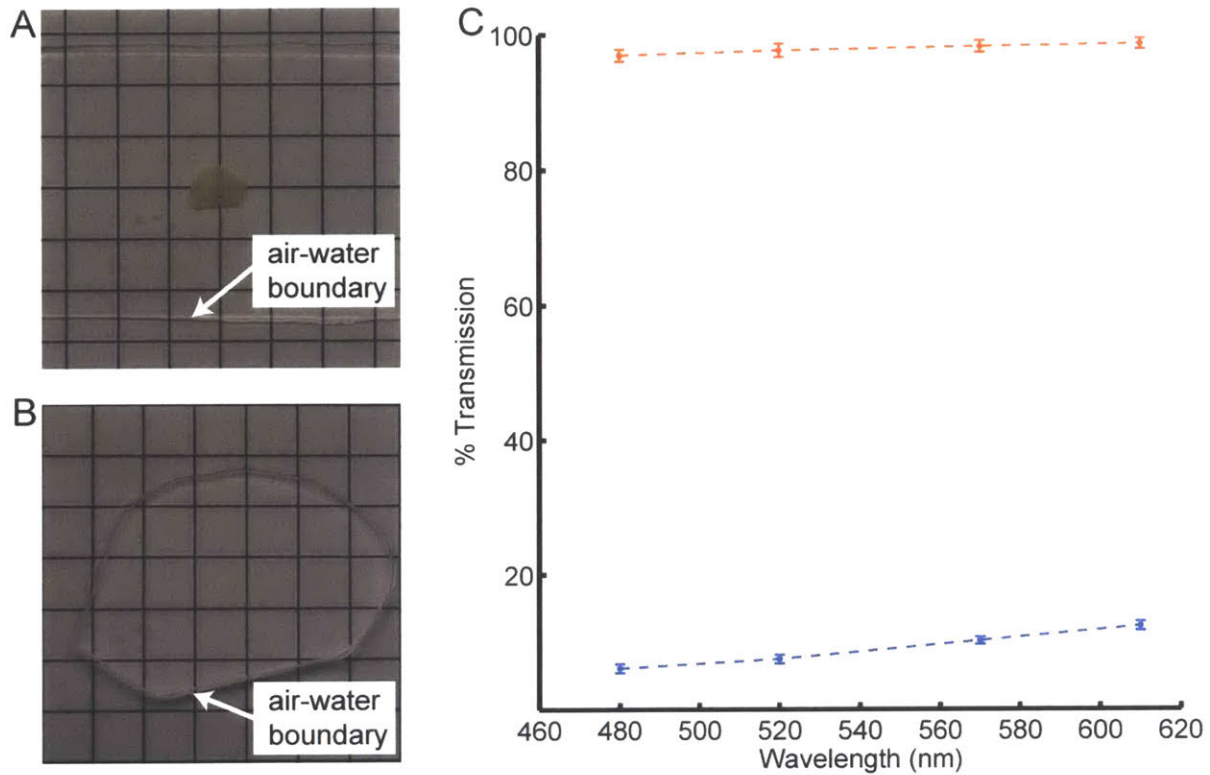


Figure S2. Optical clearing associated with ExM. Expansion significantly reduces scattering of the sample, since the sample is mostly water. A 200 μm fixed brain slice is opaque primarily due to scattering (A). However, the post-ExM sample is transparent (B). We quantified the transmittance of light through the tissue pre- (blue) vs. post- (orange) ExM processing (C).

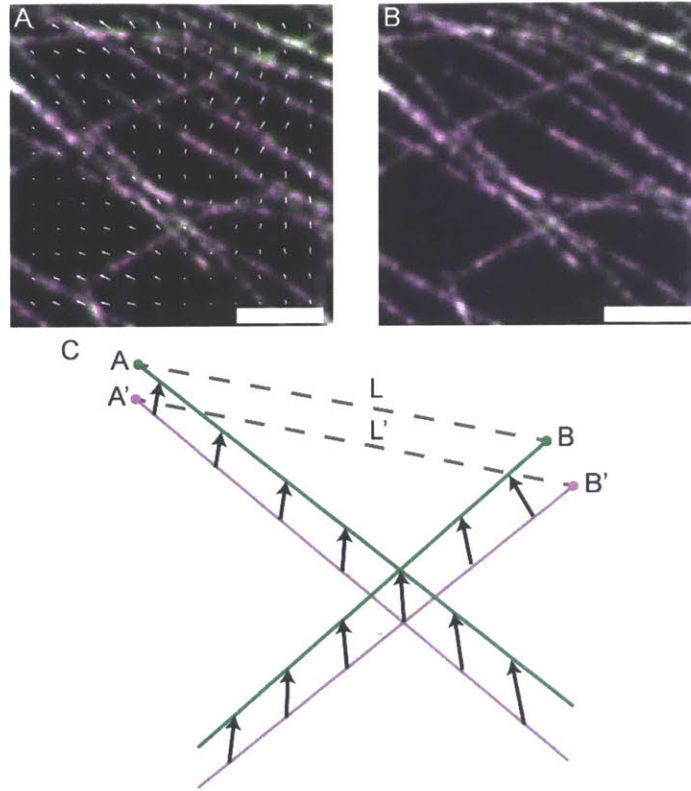


Figure S3. Quantification of Expansion Error Using Non-Rigid Registration. We quantified the error of ExM by deforming the post-ExM image via a non-rigid registration process to attempt an exact match to the pre-ExM image (in contrast to the similarity transform used in **Fig. 2A, 2B** and elsewhere). We used a B-spline based non-rigid registration algorithm (see **Methods**) which generates a vector field that maps the post-ExM image (**A**, magenta) to the pre-ExM image (**A**, green). In (**A**) the overlap between the pre- and post-ExM images appears white, and the deformation vector field (white arrows) is plotted with vector magnitudes scaled by factor of 2 for visibility. The post-ExM image after deformation (**B**, magenta) colocalizes with the pre-ExM image (**B**, green; overlap appears white). Using this deformation field, we can calculate the error of ExM for various length measurements. This is schematized in (**C**): the magenta lines, representing structures in the post-ExM image, are mapped to the green lines, representing the pre-ExM image, via the vector field depicted by black arrows. Measurement L' along the line segment $A'B'$ in the post-ExM image is mapped to measurement L along the line segment AB in the pre-ExM image. The ExM error is calculated as $|L-L'|$, i.e. the difference between the deformation vectors AA' and BB' . Using the deformation field generated we can calculate the ExM error between all extracted features in the pre- vs. post- images. Scale bars: 1 μm .

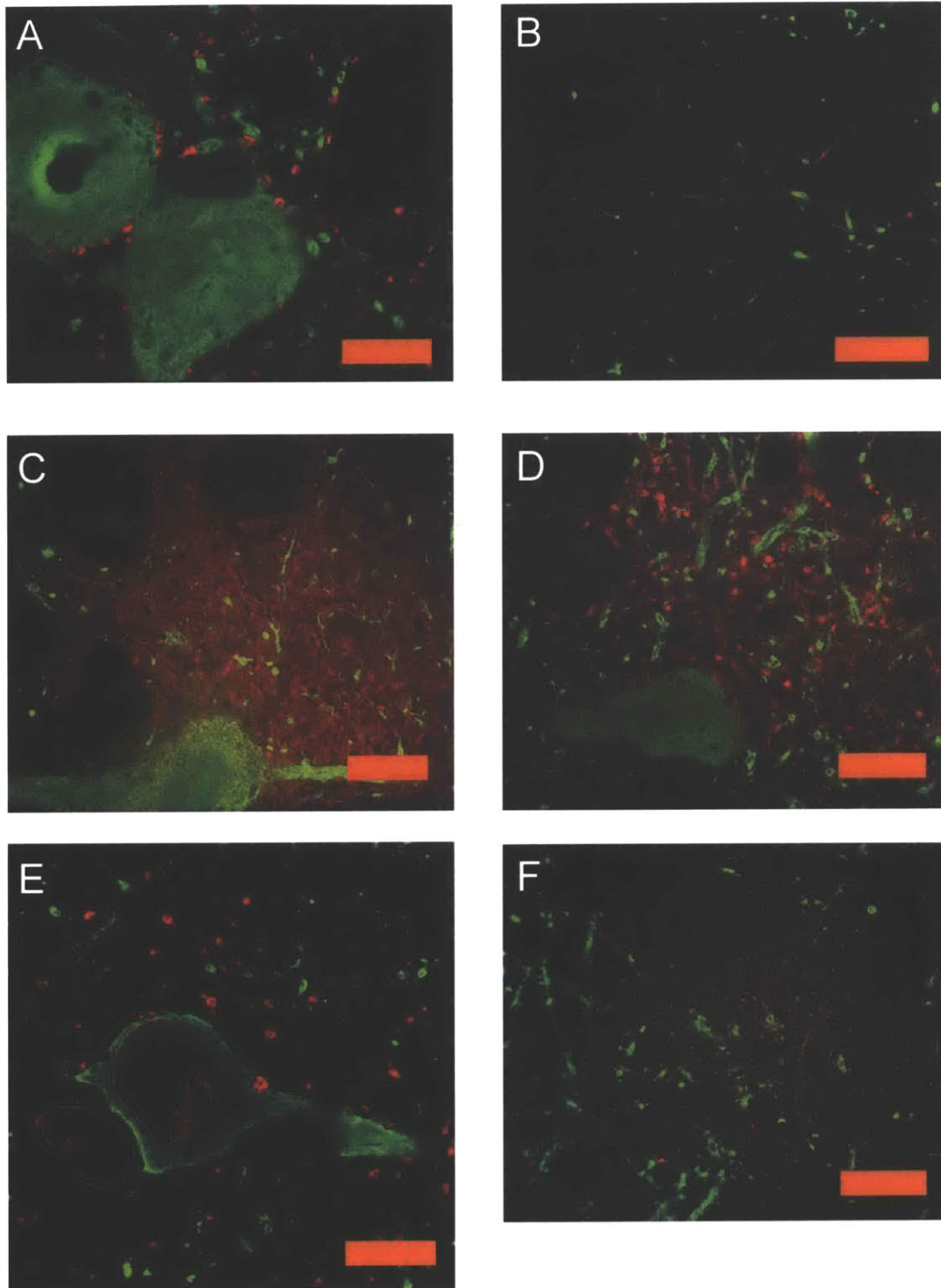


Figure S4. ExM imaging of antibodies of interest in neuroscience and biology. Confocal images of expanded Thy1-YFP mouse brain cerebral cortex sections stained with anti-GFP (green) and antibodies against other proteins (red) as follows: **(A)** GAD65/67³², **(B)** ChAT³³, **(C)** CaMKII³⁴, **(D)** GABA³⁵, **(E)** Lamin A/C³⁶, **(F)** NMDAR2a/b³⁷. Scale bars: **(A)** 10 μ m in

pre-expansion units (physical size post-expansion, 45 μ m); (B) 10 μ m (47 μ m); (C) 10 μ m (40 μ m); (D) 10 μ m (44 μ m); (E) 10 μ m (43 μ m); (F) 10 μ m (43 μ m).

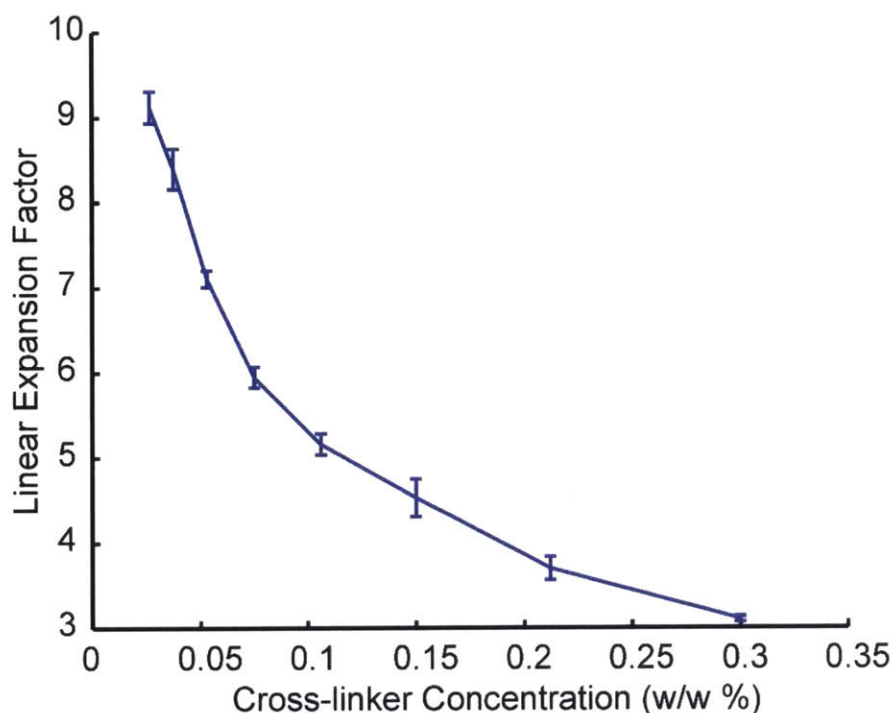


Figure S5. Expansion factor vs. cross-linking. Linear expansion factor for gels cast without specimens, as a function of the concentration of cross-linker used. Error bars represent standard deviation (n = 4 samples).

Supplementary Tables

Table S1. Fluorescence retention during ExM chemical steps.

Fluorescence Retention After Gelation		
	Percent Retention	Standard Deviation (%)
Alexa 488	57.2	2.9 (n = 2 slices)
Atto 565	76.2	0.5 (n = 2 slices)
Atto 647N	58.5	2.8 (n = 2 slices)
Covalent Anchoring Efficiency During Gelation		
	Percentage Anchored	Standard Deviation (%)
Acrydite DNA	87.2	1.1 (n = 4 gels)

Table S2. Chemicals list and suppliers.

	Chemical Name	Supplier	Part Number
ExM Gel or Preparation	Sodium Acrylate	Sigma	408220
	Acrylamide	Sigma	A9099
	N,N'-Methylenebisacrylamide	Sigma	M7279
	Ammonium Persulfate	Sigma	A3678
	N,N,N',N'-Tetramethylethylenediamine	Sigma	T7024
	4-Hydroxy-TEMPO	Sigma	176141
Fluorescent Dyes	Alexa 488 NHS ester	Life Technologies	A-20000
	Atto 565 NHS Ester	Sigma	72464
	Atto 647N NHS Ester	Sigma	18373
Hybridization Buffer	Dextran Sulfate	Millipore	S4030
	SSC	Life Tech.	15557
	Yeast tRNA	Roche	10109495001
	Normal Donkey Serum	Jackson Immunoresearch	017-000-001

Fixation and Permeabilization	Paraformaldehyde	Electron Microscopy Sciences	15710
	Glutaraldehyde	Electron Microscopy Sciences	16020
	Triton X-100	Sigma	93426
	Glycine	Sigma	50046
	PBS	Life Technologies	70011-044
Protein Digestion	Proteinase K	New England Biolabs	P8107S
	Ethylenediaminetetraacetic acid	Sigma	EDS
	Guanidine HCl	Sigma	G3272
	Tris-HCl	Life Technologies	AM9855

Table S3. DNA sequences and modifications used for tri-functional labels.

All DNA sequences were ordered from Integrated DNA Technologies, and adapted from ³⁸. Each strand for antibody conjugation consists of two 20bp domains separated by two bases of A/T.

Name	Sequence	Modifications
Antibody A	CCGAATACAAAGCATCAACG AA GGTGACAGGGATCACAATCT	5' Amine
Antibody B	TACGCCCTAAGAATCCGAAC TT GCATTACAGTCCTCATAAGT	5' Amine
Antibody C	GACCCTAAGCATAACATCGTC TT GACTACTGATAACTGGATTG	5' Amine

Two complementary tri-functional label domains hybridize to each strand conjugated to an antibody. Each antibody strand corresponds to one color of dye.

Name	Sequence	Modifications
A1	CGTTGATGCTTTGTATTCGG	5' Acrydite 3' A488
A2	AGATTGTGATCCCTGTCACC	5' Acrydite 3' A488
B1	GTTCGGATTCTTAGGGCGTA T	5' Acrydite 3' Atto 565
B2	ACTTATGAGGACTGTAATGC T	5' Acrydite 3' Atto 565
C1	GACGATGTATGCTTAGGGTC T	5' Acrydite 3' Atto 647N
C2	CAATCCAGTTATCAGTAGTC T	5' Acrydite 3' Atto 647N

Table S4. Monomer solution recipe.

Component	Stock concentration*	Amount (mL)	Final concentration*
Sodium acrylate	38	2.25	8.6

Acrylamide	50	0.5	2.5
N,N'-Methylenebisacrylamide	2	0.75	0.15
Sodium chloride	29.2	4	11.7
PBS	10x	1	1x
Water		1	
Total		9.5**	

*All concentrations in g/100 mL except PBS

This solution is stored as 0.95 mL aliquots, with initiator, accelerator and inhibitor (as needed; see **Methods) added to bring the final volume up to 1 mL per aliquot immediately before each experiment.

Methods

Labels for ExM:

DNA sequences on secondary antibodies were synthesized with 5' amine modification (Integrated DNA Technologies) and conjugated to the antibodies (Jackson ImmunoResearch, Affinipure donkey antibodies) using a commercial kit (Solulink, Antibody-Oligonucleotide All-in-One Conjugation Kit). For the tri-functional label, the oligonucleotides were synthesized with a 3' amine modification and a 5' Acrydite modification (Integrated DNA Technologies), then conjugated to dyes (Alexa 488, Atto 565 and Atto 647N) modified with NHS-ester chemistry per the dye manufacturer's directions (see **Supp. Table 2** for sequences). We found that Cy5 undergoes strong bleaching during polymerization, most likely due to the radical reactivity of its simple linear conjugated backbone. Tri-functional labels were purified via reverse-phase HPLC, lyophilized, and re-suspended in ddH₂O.

Cultured cell preparation and staining:

HEK293-FT cells (Invitrogen) were cultured in Culturewell Chambered Coverglasses (Invitrogen) per manufacturer's instructions. All solutions below were made up in 1x phosphate buffered saline (PBS), and incubations carried out at room temperature. To preserve microtubule ultrastructure, cells were fixed, as in ²³, in 3% formaldehyde/0.1% glutaraldehyde for 10 minutes, followed by reduction with 0.1% NaBH₄ for 7 minutes, and quenching in 100 mM glycine for 10 minutes. For clathrin, cells were fixed in 4% formaldehyde for 10 minutes followed by quenching in 100 mM glycine for 10 minutes. Cells were permeabilized with 0.2% Triton X-100 for 15 minutes at room

temperature and blocked with 5% normal donkey serum for one hour. Specimens were incubated with primary antibodies (Sheep Anti-Tubulin, Cytoskeleton ATN02; Rabbit Anti-Clathrin, Abcam ab21679) in blocking buffer at a concentration of 10 μ g/mL for 1-4 hours, and then washed in PBS three times for 5 minutes each. Specimens were incubated with DNA-labeled secondary antibodies in DNA hybridization buffer (2x saline-sodium citrate (SSC) buffer, 10% dextran sulfate, 1 mg/mL yeast tRNA, 5% normal donkey serum) at a concentration of approximately 10 μ g/mL for 1-4 hours, then washed in PBS as for primary. Specimens were incubated with tri-functional labels in hybridization buffer at a concentration of 0.5 ng/ μ L overnight, then washed three times in 1x PBS.

Brain tissue preparation and staining:

All procedures involving animals were in accordance with the US National Institutes of Health Guide for the Care and Use of Laboratory Animals and approved by the Massachusetts Institute of Technology Committee on Animal Care. Thy1-YFP-expressing mice were anesthetized with isoflurane and perfused transcardially with ice cold 4% paraformaldehyde. Brains were dissected out, left in 4% paraformaldehyde at 4°C for one day, and then sunk in 30% sucrose with 100 mM glycine for one day (because some tissues were slated for thin-slice cryotomy in anticipation of expediting antibody staining time, but this turned out not to be necessary). Slices greater than 60 μ m thick were sliced on a vibratome (Leica VT1000S). Slices were permeabilized and blocked in 1x PBS with 0.1% Triton X-100 and 2% normal donkey serum (slice blocking buffer) for at least six hours. Slices were incubated with primary antibodies (Chicken Anti-GFP, Millipore AB16901; Rabbit Anti-Homer1, Synaptic Systems 160003; Mouse Anti-Bassoon, Abcam ab101772) in slice blocking buffer at a concentration of 10 μ g/mL for 6-12 hours, and then washed in slice blocking buffer four times, for thirty minutes each time, changing solutions in between. Slices were incubated with DNA-labeled secondary antibodies in hybridization buffer plus 0.1% Triton X-100 at a concentration of approximately 10 μ g/mL for 6-24 hours, then washed in slice blocking buffer as for primary. Specimens were incubated with tri-functional labels in hybridization buffer plus 0.1% Triton X-100 at a concentration of 1 ng/ μ L for 6-12 hours, then washed in slice blocking buffer as for primary.

***In situ* polymer synthesis:**

Monomer solution (1x PBS, 2 M NaCl, 8.625% (w/w) sodium acrylate, 2.5% (w/w) acrylamide, 0.15% (w/w) N,N'-methylenebisacrylamide) was mixed, frozen in aliquots, and thawed before use. Prior to embedding, monomer solution was cooled to 4°C to prevent premature gelation. Concentrated stocks (10% w/w) of ammonium persulfate (APS) initiator and tetramethylethylenediamine (TEMED) accelerator were added to the monomer solution up to 0.2% (w/w) each. For slices, the inhibitor 4-hydroxy-2,2,6,6-tetramethylpiperidin-1-oxyl (4-hydroxy-TEMPO) was added up to 1 ppm (w/w) from a 100 ppm (w/w) stock to inhibit gelation during diffusion of the monomer solution into tissue sections. Stained cells or tissue slices were incubated with the monomer solution plus APS/TEMED (and 4-hydroxy-TEMPO for slices) at 4°C for one

minute, 30 minutes or 45 minutes for cultured cells, 100 μm slices and 200 μm slices respectively, and then transferred to a humidified 37° C incubator for two hours. Slices were incubated with 100-fold excess volume of monomer solution.

Specimen-free gels (**Supp. Fig. 3**) were cast with the same recipe as for cultured cells except with a variable amount of cross-linker, in forms constructed from two coverslips separated by a silicone gasket 1 mm thick, with circular holes 5.2 mm in diameter. Gels were expanded as with cultured cells, but without needing digestion. Diameters of expanded gels were measured using Vernier calipers to find the linear expansion factor.

Digestion and expansion:

Proteinase K (New England Biolabs) was diluted to 200 $\mu\text{g}/\text{mL}$ in digestion buffer (50 mM Tris (pH 8), 1 mM EDTA, 0.5% Triton X-100, 0.8 M guanidine HCl) and applied directly to gels in at least ten times volume excess. For cells, gels were formed in a Culturewell Chambered Coverglass (Invitrogen), and the chamber walls removed before adding digestion buffer in order to improve access of enzyme to the embedded cells. For tissue slices, gel chambers were constructed with two pieces of coverglass separated by spacers on either side of the tissue section (for 100 μm sections, #1 coverglasses were used for spacers and for 200 μm sections, two # 1 coverglasses were used for spacers). The gels were then incubated in digestion buffer for greater than 12 hours. Digested gels were next placed in excess volumes of doubly de-ionized water for 0.25-2 hours to expand, with longer times for thicker gels. This step was repeated 3-5 times in fresh water, until the size of the expanding sample plateaued.

Imaging:

Cultured cells. Super-resolution structured illumination microscope imaging was performed on a Deltavision OMX SIM microscope with 100x 1.40 NA (Olympus) oil objective. Stained cells were imaged with SlowFade Gold (Invitrogen) antifade reagent for suppression of photobleaching and refractive index matching for pre-expansion imaging. Pre-expansion imaging was performed on a Zeiss Laser Scanning Confocal (LSM710) with 40x 1.30 NA oil objective at 1 Airy unit and Nyquist sampling.

Post-expansion imaging was performed on a Perkin Elmer spinning disk (CSU-10 Yokogawa) confocal or a Zeiss LSM 710. Briefly, expanded samples were placed in glass-bottom six-well plates (In Vitro Scientific) and held in place by surrounding with low-melting point agarose. Images were taken at with 1 Airy unit and Nyquist sampling on the LSM 710 on a 20x 0.8 NA (Zeiss) air objective. Images on the Perkin Elmer were taken on a 100x 1.40 NA (Zeiss) oil objective.

Brain slices. To quantify expansion factor for tissue slices, specimens were imaged on a Nikon Ti-E epifluorescence microscope. Otherwise, tissue slices were imaged using an Andor spinning disk (CSU-X1 Yokogawa) confocal system with a 40x 1.15 NA water immersion objective (Nikon).

For pre-ExM confocal imaging, stained slices were treated with an anti-fade buffer (0.05% (w/w) p-phenyldiamine, 20 mM Tris (pH 8.5), 100 mM NaCl). Expanded slices were sandwiched between coverslips of appropriate size (e.g., 45 x 60 mm), forming a chamber which was then backfilled with water and sealed with epoxy. Specimens encapsulated in this way were stable for at least a few days without needing a controlled, humidified environment.

For large volume imaging of the mouse hippocampus, the encapsulated expanded specimen was tiled with an array of 12 by 5 Z stacks with ~20% overlap at the boundaries (Nikon). The tiled stacks were downsampled by a factor of 8 for 3D rendering and reconstructed with the ImageJ stitching plugin³⁹. Imaging of these 60 confocal Z-stacks, in three colors, with filter switching between each color (required for the low-crosstalk imaging using CMOS cameras in the spinning disk microscope), took ~27 hours.

Optical clearing measurements:

Transmission measurements of tissue sections before and after expansion were performed using transmitted white light illumination on a Nikon Ti-E inverted microscope with pass-band filters (480/20, 520/20, 572/20, 610/38) to quantify wavelength dependence. Briefly, 200 μm thick tissue sections were imaged before expansion and after expansion with a 4x 0.13 NA objective with tiling to cover the entire area of the slice. Light transmission was calculated by measuring the transmission intensity of a circular region of interest centered on the tissue slice normalized by the average light transmission absent of the tissue slice.

Microscopy analysis:

Spinning disk confocal image processing. Standard flatfield correction was performed as needed due to uneven illumination background. Specifically, background was subtracted with a 200 pixel wide ‘rolling ball’ algorithm as implemented in ImageJ (i.e., **Fig. 2E, 2L, Fig. 4**).

Expansion degree calculation. The expansion degree was determined by choosing two landmarks that could be clearly identified in both pre- and post-expansion images, measuring the distance between these landmarks, and calculating the ratio of this measurement pre- vs. post-expansion. These manually chosen points were used to register the images to each other using a similarity transform (i.e., translation, rotation, and scaling) and the resulting registered images were inspected visually to confirm reasonable registration over the entire specimen.

Non-rigid registration for analysis of measurement errors. Pre- and post-ExM images were first histogram equalized (i.e., for the entire histogram of pixel intensities across each image; Matlab) to each other. Masks were generated to exclude regions with no features by applying a Gaussian blur with a standard deviation of 8 pixels and manually choosing an intensity threshold below which to exclude pixels that were part of the background. (Gaussian blur was used only to generate masks, not for subsequent image processing.) Non-rigid registration between the images was performed using a B-spline-based registration package in Matlab⁴⁰ using manually selected

control points carrying a penalty weight of 1. Registration was performed in four stages with B-spline grids increasing in density from 64 pixels per grid point to 8 pixels per grid point. Analysis of measurement error was performed as schematized in **Supp. Fig. 2**.

Microtubule full width at half maximum (FWHM): Intensity profiles perpendicular to microtubule orientation was taken averaging over a line profile width of 10 pixels (~150 nm). Intensity profiles were fit to a Gaussian using the Matlab 'fit' function and the FWHM calculated from the Gaussian fit.

Quantification of clathrin coated pit (CCP) radii: Super-resolution structured illumination microscope (SR-SIM) and ExM images of CCPs were first aligned via similarity transform using 2 control points across the field of view. CCPs were identified by visual inspection of ExM z-stacks, and were selected with a rectangular region of interest (ROI, ~2x diameter of pit) so that there were no neighboring pits or background punctate staining within an ROI. For each pit selected in the analysis, its ROI was used to crop the ExM image and corresponding SR-SIM image. A maximum intensity projection of the ExM image corresponding to the same depth of field as the SR-SIM image was chosen to adjust for different optical sectioning thickness, corresponding to ~2 ExM planes (~60 nm/plane in pre-expansion units) for each SR-SIM z-plane (125 nm/plane) chosen. CCP radii were calculated with angular averaging of a radial line profile originating from the centroid of each CCP, with the centroid calculated from the Otsu-binarized image. The angular radial line profile was fit using the Matlab 'fit' function to the sum of 2 Gaussians. The CCP radius was determined to be the half maximum of the fitted angular line profile.

Synapse quantification: Synapses were identified by visual inspection of ExM z-stacks. Candidate instances of closely apposed Bassoon and Homer1 antibody-stained spots were selected from a maximum intensity projection of each stack. Each candidate was then inspected in the original z-stack and selected for inclusion in the analysis if it did not meet any of the following rejection criteria: synapses that were not oriented perpendicular to the imaging plane were recognized when the stained spots shifted continuously between consecutive z-slices, and were rejected; synapses with coincident punctate background staining were rejected; complex assemblies of synapses (e.g., with multiple pre- or post-synaptic terminals) were rejected; synapses that were excessively curved (e.g., relative to the 10-pixel line width, see below) were rejected. For each synapse selected for inclusion in the analysis, a line profile perpendicular to the synaptic cleft was chosen. The staining intensity for Bassoon and Homer1 was analyzed along each line profile, averaging over a width of 10 pixels (~300 nm). The resulting intensity distributions were fit to Gaussian distributions with a DC offset using the Matlab 'fit' function. Any synapses with a resulting goodness of fit, for either Homer1 or Bassoon, of less than 0.9 were rejected. The Bassoon-Homer1 separation was calculated as the separation between the means of the two distributions for each synapse.

Chapter Three: Protein Retention Expansion Microscopy

Introduction

We recently developed a technology that enables imaging of thick preserved specimens with nanoscale precision⁴¹. In this technique, which we call expansion microscopy (ExM), the optical diffraction limit is circumvented by physically expanding a biological specimen prior to imaging, thus bringing sub-diffraction limited structures into the size range viewable by a conventional diffraction-limited microscope. Thus, ExM enables imaging of biological specimens at the voxel rates of a diffraction limited microscope, but with the voxel sizes of a super-resolution microscope. Such samples are transparent, and index-matched to water, as the expanded material is >99% water. Our original ExM protocol worked by labeling biomolecules of interest with a gel-anchorable fluorophore. Then, a swellable polyelectrolyte gel was formed throughout the sample, so that it incorporated the labels. Finally, the sample was treated with a nonspecific protease to homogenize its mechanical properties, followed by dialysis in water to result in unimpeded physical expansion of the polymer-specimen composite. All of the chemicals can be purchased except the gel-anchorable label, which requires custom chemical synthesis. Ideally one could perform ExM with solely off-the-shelf chemicals, as in conventional fluorescent immunohistochemistry.

Here, we report a variant of ExM, which we call protein retention ExM (proExM), in which proteins, rather than labels, are anchored to the swellable gel, using a commercially available cross-linking molecule. We explored less disruptive methods than nonspecific proteolysis, such as antigen retrieval and the usage of targeted proteases, and found that these strategies enabled many retained native proteins to be antibody labeled after expansion. We directly compared the staining brightness for antibody targets using these methods, and found stronger signal with post-disruption than pre-gelation staining, for several targets. However, these methods require optimization on a per-target basis and in some cases result in defects in uniform tissue expansion. To develop an optimization-free method that is compatible with existing labeling methods, we demonstrate that genetically encoded fluorescent proteins and conventional fluorescently labeled secondary antibodies and streptavidin that are directly anchored to the gel exhibit preserved fluorescent signals even when subjected to the nonspecific proteolytic digestion from the original ExM protocol. Furthermore, an increase in digestion temperature allowed this protocol to generalize to a diversity of mammalian tissue types with varying mechanical properties. proExM is thus a simple extension of standard histological methods used to prepare samples for imaging.

Results

Strong protease digestion (i.e., with proteinase K) enabled isotropic expansion in the original ExM protocol. We asked whether native proteins could be chemically anchored to the

ExM gel and stained with antibodies in the expanded state. As a first experiment, we used a modified approach with reduced proteolysis, in hopes of epitope preservation. To incorporate proteins into the polymeric gel we used the succinimidyl ester of 6-((Acryloyl)amino)hexanoic acid (Acryloyl-X, SE, abbreviated AcX, Life Technologies), which modifies amines on proteins with an acrylamide functional group. Borrowing from denaturing SDS-PAGE⁴² and antigen retrieval protocols⁴³, we treated gel-embedded tissues in an alkaline detergent-rich buffer for one hour in an autoclave, and found ~4x expansion of Thy1-YFP mouse brain samples (**Fig. 1a**, showing endogenous YFP pre-treatment; **Fig. 1b**, showing post-expansion labeling with anti-GFP). We found that antibodies could indeed be delivered successfully post-expansion (**Fig. 1c-e**). As a second treatment strategy, we exposed gel-embedded tissues to LysC, which cuts proteins at Lys residues (in contrast to nonspecific proteinase K)^{44,45} (**Supplementary Fig. 1**). Post-expansion staining in both cases was highly variable depending upon antibody identity (e.g., compare lamin A/C examined with three different protocols, **Fig. 1f(i-iii)**), to images obtained in the original ExM protocol, **Supp. Fig. 4** of ref. 1; additional examples, **Supplementary Fig. 2**). For some antibodies, post-expansion staining appeared to result in brighter signal compared to pre-gelation staining (Tom20, **Fig. 1g(i)** vs **h(i)** (autoclaved); GFP, **Fig. 1g(ii)** vs **h(ii)** (autoclaved); PSD-95, **Fig. 1g(iii)** vs **Fig. 1h(iii)** (LysC)). However, the variability (**Supplementary Fig. 2**) and incomplete homogenization (**Supplementary Fig. 3**) suggested that the strong proteolysis of the original ExM protocol was necessary for reliable expansion.

We next sought to devise a strategy that would combine the convenience of direct protein anchoring with strong proteinase K treatment. It is known that green fluorescent protein (GFP) exhibits extraordinary stability to proteases^{46,47}. We hypothesized that GFP and GFP-like fluorescent proteins (FPs) might retain their fluorescence after the proteolytic digestion of the original ExM method, if they were retained in the polymer-specimen composite using AcX. We discovered that treatment with AcX followed by the standard ExM workflow, including proteinase K digestion, can preserve GFP fluorescence in the expanded gel with high efficiency ($65 \pm 5\%$ preservation; mean \pm std. dev.; $n = 4$; **Fig. 2a, 2b** and **Supplementary Fig. 4**). Because of the utility of this protocol, we termed the process of AcX treatment of a fixed specimen, followed by gelation, strong digestion, expansion, and imaging as protein retention expansion microscopy (proExM).

We systematically examined persistence of fluorescence for various FPs in the proExM workflow. We selected 20 widely used FPs with spectra ranging from the blue to the near-infrared (**Supplementary Table 1**). Selected FPs were fused to histone proteins and expressed in human embryonic kidney (HEK293FT) cells. To assess FP performance in proExM, we compared images of live cultures vs. after-proExM images of the same cells (**Fig. 2a**). Most FPs retained more than 50% of their live fluorescence intensity after proExM ($n = 4$ samples each; **Fig. 2a, 2b**, **Supplementary Table 1**), comparable to the persistence of small-molecule fluorophores in the original ExM protocol⁴¹.

Having seen that FPs could persist sufficiently to report signals even after a strong digestion process, we next sought to determine if other signals might persist. We discovered that

proExM anchors, and preserves the fluorescence of, commercial fluorescently conjugated secondary antibodies. Following gelation and digestion, specimens labeled with secondary antibodies bearing a variety of small-molecule fluorophores retained ~50% of their initial brightness ($n = 3$ samples each; **Fig. 2c**; **Supplementary Table 2**). In the original ExM protocol, custom conjugation of secondary antibodies to enable labeling with a gel-anchorable fluorophore was required⁴¹. proExM, in contrast, allows commercial secondary antibodies to be used in place of these custom formulations. In addition to antibodies, we also observed preservation of signals from fluorescently labeled streptavidin. Using streptavidin, we imaged probes designed to capture cysteine-S-nitrosation using a previously developed chemical method, SNOTRAP⁴⁸, thus demonstrating the imaging of S-nitrosation signals with proExM (**Supplementary Fig. 5**). This protocol also points towards the possibility of anchoring other protease-resistant tags to the polymer, followed by gelation, digestion, expansion, and imaging, as a potentially generalized strategy.

Although the digestion step was the same as for our originally validated ExM protocol, suggesting that nanoscale isotropy would be preserved, we further validated proExM by performing imaging of immunostained microtubules in cultured cells with super-resolution structured illumination microscopy (SR-SIM) (**Fig. 2d**) before proExM and confocal (**Fig. 2e**) imaging after proExM, as we did to validate our original ExM protocol⁴¹. We quantified the root-mean-square (RMS) error of feature measurements after proExM over length scales between 0 and 20 microns, and found that RMS errors were ~1-2% of the measurement distance (**Fig. 2f**).

We performed proExM followed by confocal microscopy to image several fusion proteins bearing genetically encoded fluorophores (i.e., unstained) in cultured HeLa cells. We first examined fusions of tubulin, clathrin and keratin (**Fig. 2g-k**), which we and others have commonly used as stereotyped structures to demonstrate super-resolution imaging of cells^{21,23,49,50}. The tubulin-mClover fusion presented a microtubule full-width at half-maximum (FWHM) of 67 ± 8 nm ($n = 16$ microtubules in 3 samples) (**Fig. 2h, 2i**), suggesting a resolution of better than 70 nm^{23} . We also imaged clathrin-mEmerald in HeLa cells obtaining excellent definition of the nulls in the middle of the pits (**Fig. 2j**). Dual-color proExM imaging of fusion proteins containing mEmerald and mRuby2, two of the genetically encoded fluorophores in our screen, yielded excellent images as expected (keratin-mRuby2 and clathrin-mEmerald, **Fig. 2k**; paxillin-mEmerald and actin-mRuby2, **Fig. 2l**). We examined the stability of four photoswitchable FPs during proExM (**Supplementary Fig. 6, Supplementary Table 3**). We imaged cells expressing histone 2B-Dendra and mEos2-tubulin fusions with PALM microscopy (**Supplementary Fig. 6**), demonstrating preservation of photoswitching fluorophores compatible with PALM (although validating resolution claims for post-ExM PALM is beyond the scope of this paper).

To assess the performance of proExM in three-dimensional tissues, we performed proExM on four different mouse tissue types (brain, pancreas, lung and spleen, **Fig. 3a-d**). Mouse brain expressing YFP under the Thy1 promoter (Thy1-YFP) in a sparse subset of neurons expands without distortion at the millimeter scale following treatment with proteinase K as described for cultured cells (**Fig. 3a**, top vs. bottom). Pancreas, spleen and lung have different mechanical

properties than brain (e.g., more connective tissue), which hinders expansion following room temperature proteinase K digestion. We antibody stained the intermediate filament vimentin as a marker of connective tissue to examine the isotropy of expansion in these diverse tissue types. We observed that, with a slight modification in the digestion temperature to the optimum of the proteinase K enzyme (60° C for 4 hours), proExM allows for expansion of pancreas, lung, and spleen tissue, with excellent preservation of tissue morphology at the millimeter length scale (**Fig. 3b-d**, top vs. bottom). High-resolution diffraction-limited microscopy of the tissue before (**Fig. 3e, 3f**) vs after proExM (**Fig. 3e, 3g**) shows the resolution improvement of proExM. We quantified the isotropy of expansion by measuring the root-mean-square (RMS) error of feature measurements after proExM in the microscale (<100 μm) for pancreas, lung and spleen tissue. The RMS errors were small (1-3% of the measurement distance) and similar among all three of the tissue types (**Fig. 3h**) at this length scale.

To examine the isotropy of expansion at the nanoscale, we performed SR-SIM (**Fig. 3i, 3j**) and proExM confocal imaging (**Fig. 3i, 3k**) on vimentin staining in the pancreas. Again, we observed small RMS errors on the order of 1-5% of the measurement length for measurements between 0 and 25 microns (**Fig. 3l**, $n = 4$ fields of view from 2 samples). We performed a similar analysis on mouse brain cortical tissue stained with antibodies against Tom20, a mitochondrial marker, and imaged with SR-SIM before (**Fig. 3m, 3n**) and confocal after (**3o**) proExM processing using proteinase K digestion at room temperature. RMS errors for this tissue type were between 1-3% of the measurement length, between 0 and 40 microns (**Fig. 3p**, $n = 3$ specimens)

Transgenic animals expressing FPs, as well as animals expressing FPs after viral gene delivery, are routinely used in biology for labeling proteins and cells in intact tissues and organisms. We applied proExM for visualization of FPs expressed in intact mammalian brain tissue, including the brains of mice (**Supplementary Fig. 7**) and a rhesus macaque (**Fig. 4a-c**), obtaining images that as expected showed minimal macroscale distortion after expansion (e.g., compare **Fig. 4a** vs **4b**). Using a high magnification lens on a conventional confocal microscope, dendritic spine morphology was easily resolved after expansion, with even thin spine necks visible (**Fig. 4c** inset, arrow).

We applied proExM for imaging of mouse brain circuitry expressing virally delivered Brainbow3.0^{51,52}, which marks neurons with random combinations of membrane anchored FPs. These FPs are antigenically distinct to allow for subsequent amplification via antibodies. Following proExM, antibody staining and morphology are preserved in brain tissues (**Fig. 4d** vs **4e**). Confocal imaging allows for large volume, multi-color super-resolved imaging of the Brainbow sample (**Fig. 4f**). Side-by-side comparison of confocal images before (**Fig. 4g**) and after (**Fig. 4h**) expansion shows how axons and dendrites too close to resolve before expansion can be clearly resolved after expansion (**Fig. 4g, h**).

Discussion

We here report that it is possible to directly anchor proteins to a swellable gel synthesized throughout a biological sample, by applying a commercially available small molecule cross-linker prior to gelation. This protein retention ExM (proExM) strategy can be used to perform nanoscale imaging of immunostained cells and tissues (**Fig. 5**, top), as well as samples expressing various FPs (**Fig. 5**, middle). ProExM variants can support post-expansion antibody delivery, potentially increasing brightness of staining and antibody access (**Fig. 5**, bottom).

We show that native proteins anchored in this way can retain epitope functionality and be labeled post-expansion if the nonspecific proteolysis of ExM is replaced with modified post-gelation homogenization treatments. Such approaches may overcome the limitations inherent to delivering antibodies in the crowded environment of native tissue⁵³⁻⁵⁷. For example, closely packed epitopes may bind antibodies poorly in dense tissue, but better access antibodies after expansion. We have demonstrated a proof of concept of this finding in this paper.

We found that fluorescent proteins and fluorescent antibodies delivered using standard methods are also retained in the gel, and furthermore exhibit fluorescent signals following nonspecific proteolysis treatment. We demonstrate the multi-color, large volume capability of proExM by expanding Brainbow samples, which may open up new methods of circuit mapping. ProExM is simple and easily integrated into existing sample workflows.

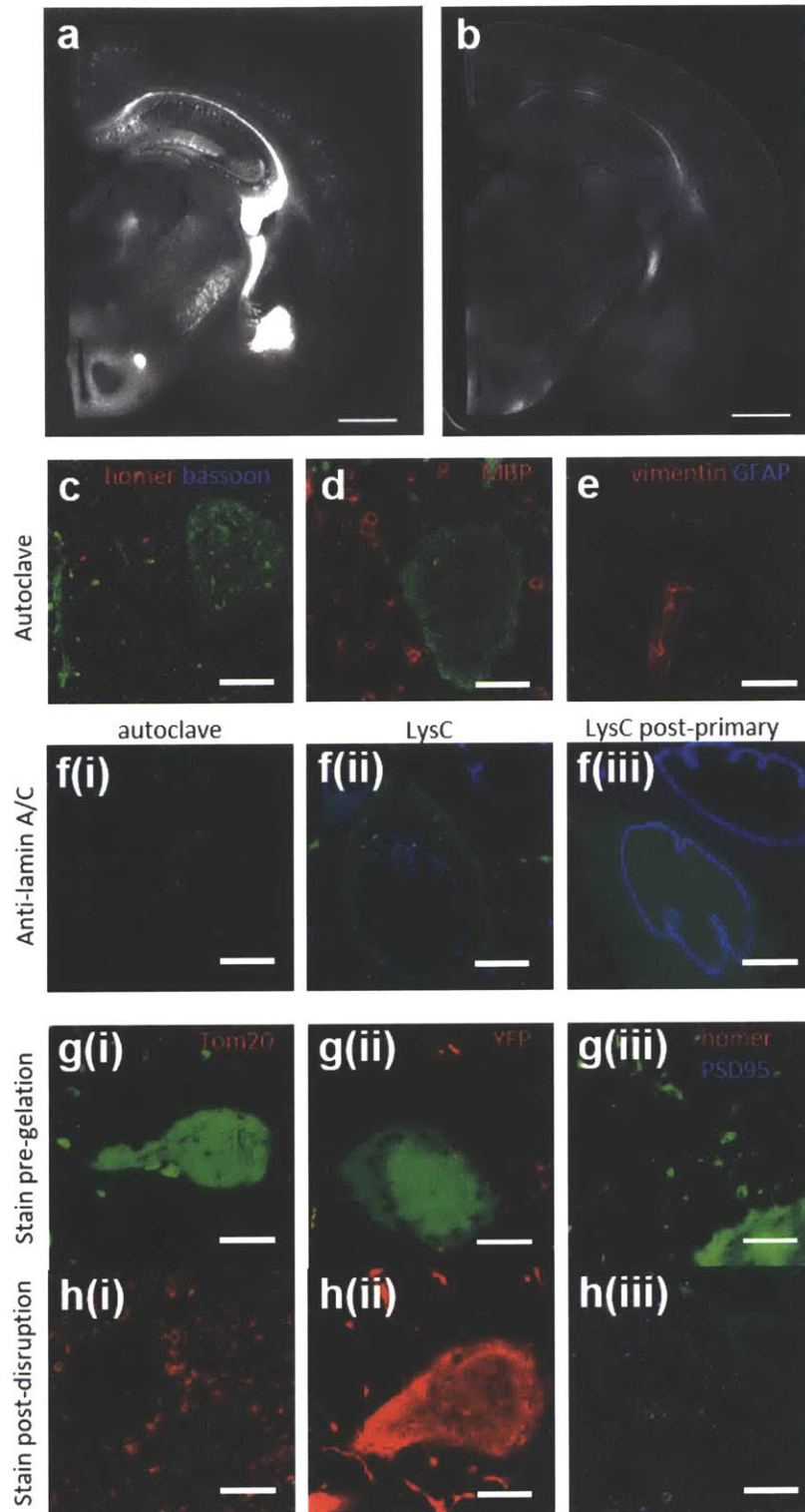
In the original ExM protocol, we conjugate DNA oligonucleotides to secondary antibodies in order to enable attaching fluorophores to the polymer at sites of antibody binding. ProExM eliminates the need for such custom-made antibody labels for ExM; instead, FPs and fluorescent secondary antibodies treated with the cross-linker can be directly visualized after expansion. Thus, proExM does not require end-users to carry out conjugation reactions, resulting in a faster protocol. Like any protocol involving antibody staining, the diffusion of unmodified antibodies will need to be considered. A key feature of ExM is that it does not require custom hardware nor fluorophores for super-resolution imaging; here we continue this line of technology development by additionally enabling the secondary antibodies to be conventional as well. Preservation of endogenous fluorescence allows for the use of transgenic animals, viral expression vectors, and transfection of FPs, all without immunostaining. Distortion was low, perhaps because both the polymer and digestion methods were the same as our original expansion protocol; only the anchoring method was different.

As with our original ExM protocol, samples processed with proExM are optically clear and index matched to water⁴¹. This allows for super-resolution imaging deep into samples, on conventional fluorescence microscopes, limited only by working distance of the objective lens. As an effective sub-diffraction limited imaging modality, ExM protocols exhibit great speed of imaging. Although samples prepared by ExM protocols are larger in size than before expansion (and thus may require longer working distance objectives and tiled acquisition), there is a net win,

since ExM protocols enable voxel sizes of super-resolution microscopy, but imaged at voxel acquisition rates of conventional microscopy. Like ExM, proExM does not require specialized hardware, extensive post-processing, or other enabling aspects of conventional super-resolution methods. As with any super-resolution method, because voxels are smaller they contain fewer fluorophores and are thus dimmer than unexpanded specimens. This effect is offset by the concomitant dilution of autofluorescence and reduced loss due to scattering, though longer exposure times are typically useful, depending on the brightness of the unexpanded specimen. proExM physically magnifies samples equally well along the axial as well as lateral dimensions. Expanded samples are compatible with downstream imaging and analysis strategies such as tomography, deconvolution, or even traditional super-resolution imaging (e.g., PALM, as shown here). Thus proExM will likely find many applications in supporting routine imaging of complex biological samples with nanoscale precision.

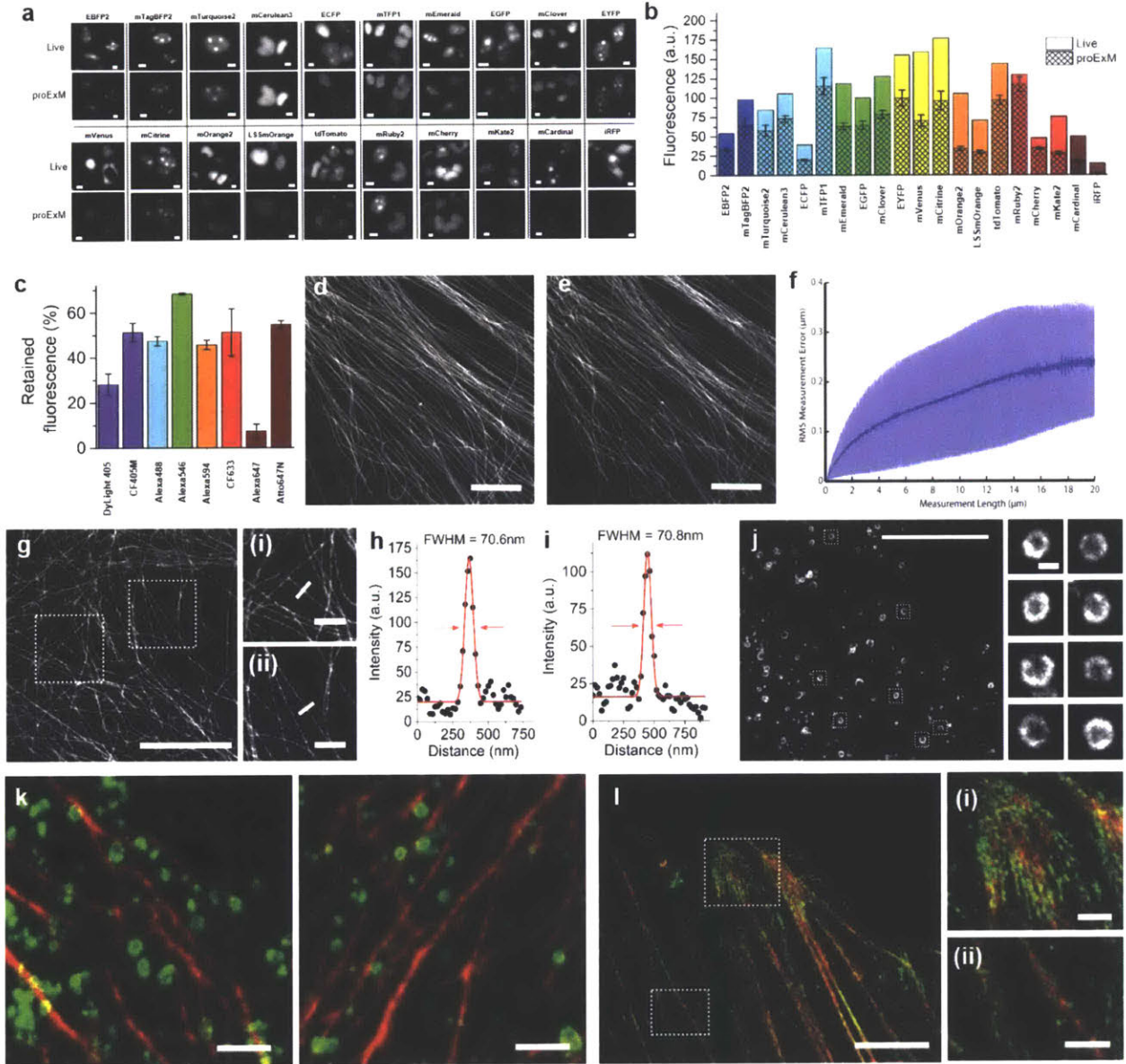
Figures

Figure 3-1. Post-expansion antibody delivery, after epitope-preserving homogenization.



(a, b) Wide-field fluorescence images of Thy1-YFP-expressing mouse brain hemisphere slice before expansion **(a)**, and after autoclave treatment and antibody staining **(b)**. **(c-h)** Confocal micrographs of cortex from Thy1-YFP-expressing mouse brain treated with different disruption methods and antibodies, with anti-GFP (green, staining YFP) as a reference. **(c)** Autoclave method followed by staining against bassoon (blue) and homer (red). **(d)** Autoclaving followed by myelin basic protein staining. **(e)** Autoclaving followed by vimentin (red) and glial fibrillar acidic protein (blue) staining. **(f)** Staining for Lamin A/C after autoclave **(i)** or LysC **(ii)** treatment, or with secondary antibodies applied after LysC homogenization (with primaries previously anchored to the gel using AcX) **(g-h)** Comparison of staining before gelation **(g)** versus after disruption **(h)** using the autoclave method for Tom20 **(i)** and YFP **(ii)**, shown in the red channel in the bottom panel because the endogenous YFP is green), and after disruption using LysC for homer (red) and PSD-95 (blue) **(iii)**. Scale bars: **(a)** 1mm, **(b)** 1mm (3.96mm), **(c-h)** 5 μ m (~21 μ m).

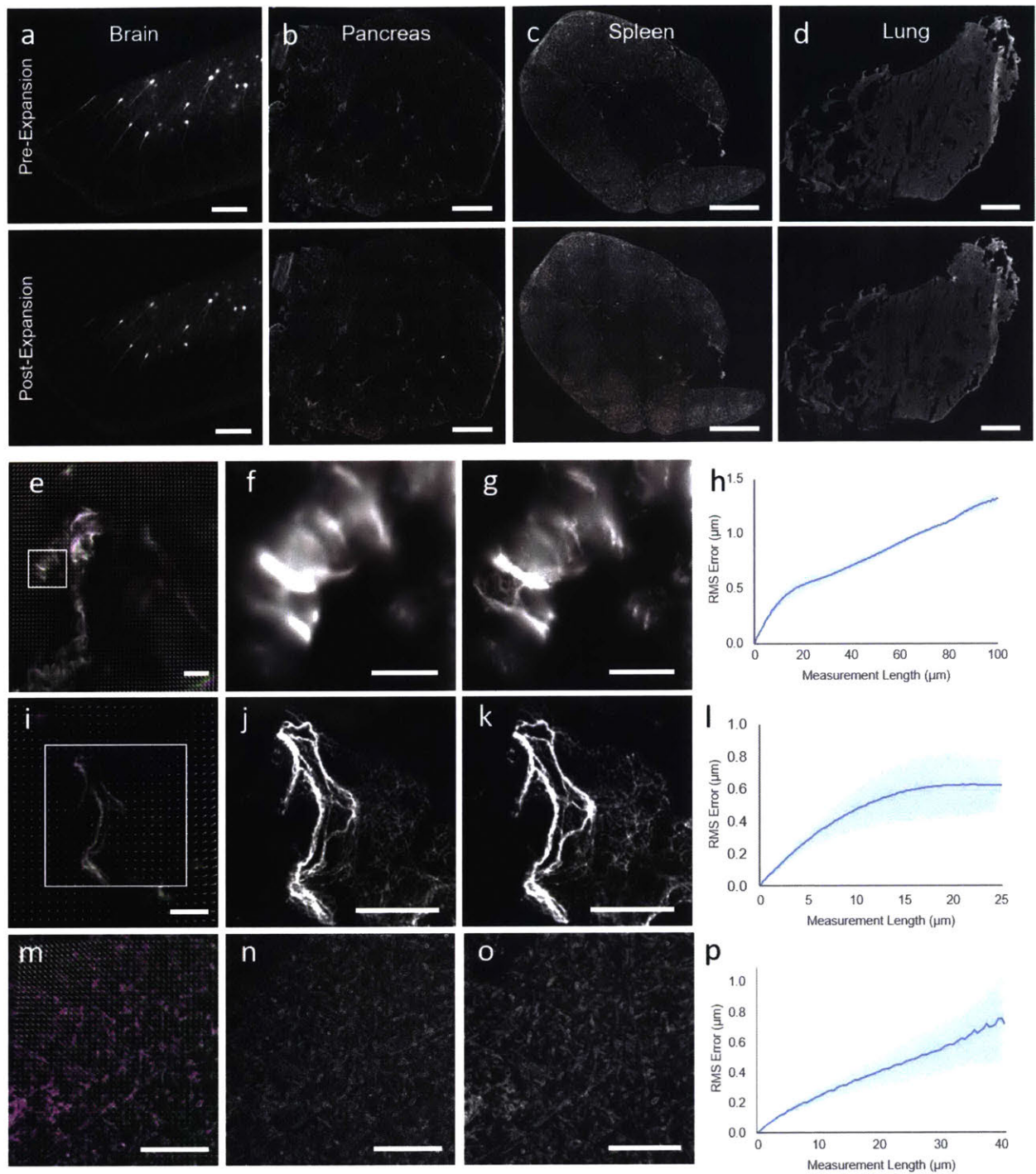
Figure 3-2. Retention of fluorescent protein (FP) and antibody fluorescence signals in proExM and proExM of FP fusions.



(a) Representative images of selected FP-histone fusion proteins in live HEK293FT cells (upper row) and in the same cells after proExM treatment (lower row); iRFP was expressed as N-terminal fusion with nuclear localization sequence (NLS). **(b)** Quantified fluorescence of experiments as in panel **a**, after proExM treatment (crosshatched bars; mean \pm standard deviation; $n = 4$ transfection replicates each). Open bars, literature values of the brightnesses of these fluorophores, normalized to the brightness of EGFP. **(c)** Retention of fluorescence for selected dyes conjugated with antibodies, after proExM treatment (mean \pm standard deviation, $n = 3$ samples each), in mouse

brain slice. **(d)** Super-resolution structured illumination microscopy (SR-SIM) image of immunostained microtubules after the anchoring step vs. **(e)** post-expansion image of the same sample acquired with a spinning disk confocal microscope. **(f)** Root mean square (RMS) length measurement error as a function of measurement length for proExM vs SIM images (blue line, mean; shaded area, standard deviation; $n = 4$ samples). **(g)** Confocal image of mClover- α -tubulin fusion. HeLa cells are used throughout the rest of this figure. Panels **(i and ii)** are magnified views of boxed regions in **(g)**. Linecuts are quantified in panels **h, i**. Solid red lines in **(h, i)** indicate the Gaussian fit used to determine the full width at half maximum (FWHM; illustrated with red arrows). **(j)** Confocal image of mEmerald-clathrin fusion (left) and magnified views of single CCPs in the boxed regions (right). **(k)** Dual color proExM of clathrin (fused to mEmerald, green) and keratin (mRuby2, red). **(l)** Dual color proExM image of actin (mRuby2, red) and paxillin (mEmerald, green) fusions. Panels **(i and ii)** are magnified views of boxed regions in **(f)**. Scale bars: **(a)** 5 μm , **(d)** 5 μm , **(e)** 5 μm (physical size post-expansion, 20.5 μm), **(g)** 5 μm (21.5 μm), **(i-ii)** 1 μm ; **(j)** 10 μm (42.6 μm), insets 200 nm; **(k)** 1 μm (4.3 μm), **(l)** 5 μm (21.5 μm), **(i-ii)** 1 μm .

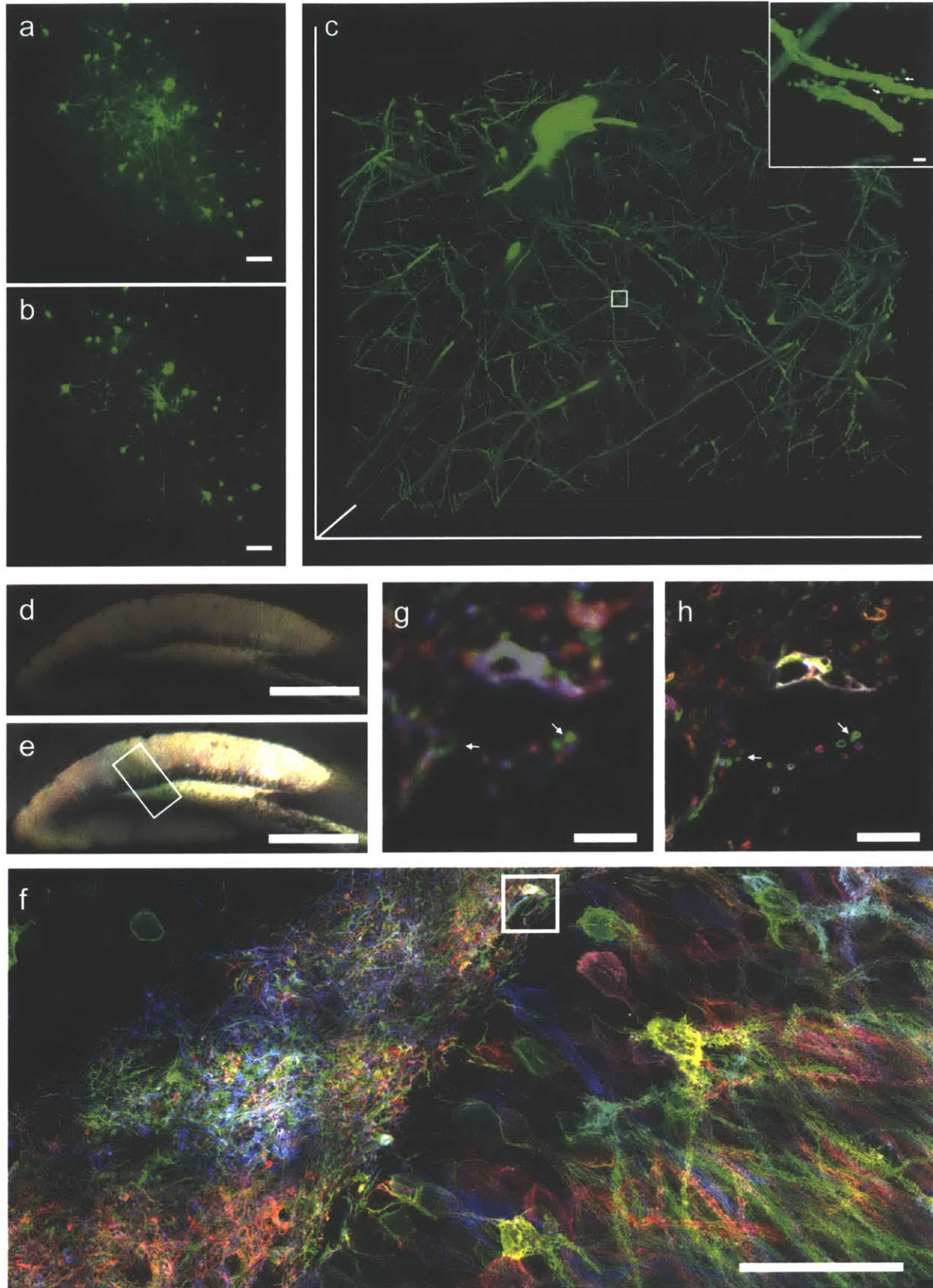
Figure 3-3. Validation of proExM in different mammalian tissue types.



(a-d) Low magnification, wide-field images of pre-expansion (top) and post-expansion (bottom) samples of Thy1-YFP mouse brain **(a)** and vimentin-immunostained mouse pancreas **(b)**, spleen **(c)**, and lung **(d)**. **(e)** Composite fluorescence image of Tom20 in Thy1-YFP mouse brain imaged with super-resolution structured illumination microscopy (SR-SIM) (green) and proExM (purple)

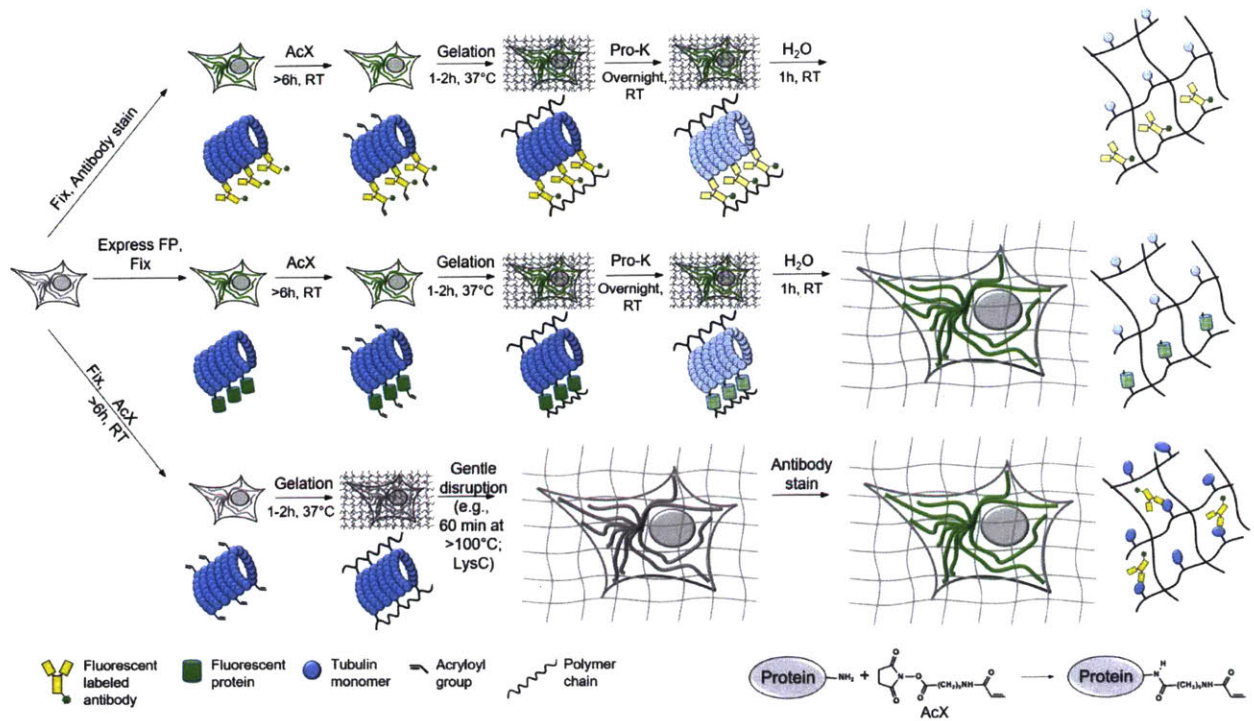
with conventional confocal microscopy with distortion vector field overlaid (white arrows). **(f)** Pre-expansion SR-SIM image showing boxed region in **(a)**. **(g)** Post-expansion confocal image of **(f)**. **(h)** RMS length measurement error as a function of measurement length for proExM vs SR-SIM pre-expansion for Tom20 staining in Thy1-YFP mouse brain (blue line, mean; shaded area, standard deviation; $n = 3$ mouse brain cortex samples). **(i)** High magnification, wide-field fluorescence composite image of vimentin in mouse pancreas before (green) and after (purple) expansion with distortion vector field overlaid (white arrows, see methods). **(j)** Pre-expansion wide-field image showing boxed region in **(i)**. **(k)** Post-expansion image of **(j)**. **(l)** Root mean square (RMS) length measurement error as a function of measurement length for proExM vs widefield pre-expansion images for the different tissue types in **(b-d)** (blue line, mean; shaded area, standard deviation; $n = 3$ samples from pancreas, spleen, and lung). **(m)** Composite fluorescence image of vimentin in mouse pancreas imaged with super-resolution structured illumination microscopy (SR-SIM) (green) and proExM (purple) with conventional confocal microscopy with distortion vector field overlaid (white arrows). **(n)** Pre-expansion SR-SIM image showing boxed region in **(m)**. **(o)** Post-expansion confocal image of **(n)**. **(p)** RMS length measurement error as a function of measurement length for proExM vs SR-SIM pre-expansion for vimentin staining in pancreas (blue line, mean; shaded area, standard deviation; $n = 4$ fields of view from 2 samples). Scale bars: **(a)** top 200 μm , bottom 200 μm (physical size post-expansion, 800 μm), **(b-d)** top 500 μm , bottom 500 μm (2.21 mm, 2.06 mm, 2.04 mm, respectively), **(e, f)** 10 μm , **(g)** 10 μm (40 μm), **(i)** 10 μm , **(j)** 5 μm , **(k)** 5 μm (20.4 μm), **(m)** 5 μm , **(n)** 5 μm , **(o)** 5 μm (20.65 μm).

Figure 3-4. proExM of mammalian brain circuitry.



(a) Wide-field image of GFP fluorescence in virally injected rhesus macaque cortex. (b) Post-expansion wide-field fluorescence image of (a). (c) Volume rendering of confocal microscopy images of subregion of (b). Inset shows a zoom-in of boxed region in (c) showing dendritic spines. (d) Low magnification widefield fluorescence imaging showing immunostained mouse hippocampus expressing virally delivered Brainbow3.0. (e) Post-expansion wide-field image of sample from (d). (f) MIP high resolution confocal microscopy image following expansion of membrane labeled Brainbow3.0 neurons from boxed region in (e). (g) Pre-expansion confocal image showing one optical section of boxed region in (f). (h) Post-expansion image of (g). Scale bars: (a) 100 μm , (b) 100 μm (physical size post-expansion, 413 μm); (c) 300 μm x 254 μm x 25 μm , (c) (i) 1 μm , (d) 500 μm , (e) 500 μm (1980 μm); (f) 5 μm , (g) 5 μm (19.8 μm); (h) 50 μm (198 μm).

Figure 3-5. Workflows for expansion microscopy with protein retention.



Three basic sample processing workflows were explored in this paper. *Top*, samples are chemically fixed and stained with antibodies, using conventional immunostaining protocols, before AcX treatment at room temperature and subsequent ExM processing (gelation, proteinase K treatment, and expansion in water). *Middle*, samples expressing fluorescent proteins (FPs) are chemically fixed (and optionally permeabilized) before AcX treatment, and subsequent ExM processing. *Bottom*, samples treated with AcX, followed by gelation, are then processed with a gentle homogenization procedure (e.g., alkaline hydrolysis and denaturation, or digestion with LysC), and finally antibody staining in the expanded state.

Supplementary Information

Protein	Ex max, nm	Em max, nm	Molecular brightness relative to EGFP, %	Brightness in proExM cells, % of live cells	Addgene plasmid code	Reference
EBFP2	383	448	54	62±4	55243	58
mTagBFP2	399	454	98	65±9	55302	59
mTurquoise2	434	474	85	68±8	36207	60
mCerulean3	433	475	105	69±4	55421	61
ECFP	434	477	39	51±2	55344	62,63
mTFP1	462	492	165	70±7	55488	64
mEmerald	487	509	118	53±4	54112	65
EGFP	489	509	100	65±5	56436	66
mClover	505	515	128	61±4	56533	67
EYFP	514	527	155	64±7 ^c	56592	68
mVenus	515	528	159	44±5	56615	69
mCitrine	516	529	177	54±7	56555	70
mOrange2	549	565	105	32±2	57962	71
LSSmOrange	437	572	71	42±3	37133	72
tdTomato	554	581	144	67±4	58102	73
mRuby2	559	600	130	90±7	55898	67
mCherry	587	610	48	72±3	55056	73
mKate2	588	633	76	37±3	NA ^a	74
mCardinal	604	659	50	36±3	56161	75
iRFP	690	713	15	14±1	NA ^b	76

Supplementary Table 1. Performance of selected FPs in proExM.

^amKate2 gene from Addgene plasmid 37132 was swapped with LSSmOrange gene in Addgene plasmid 37133.

^bcloned as N-terminus fusion with nuclear localization sequence.

^csince EYFP is particularly sensitive to the high Cl^- used to shrink the gel⁷⁷, retention of EYFP fluorescence was measured in fully expanded gel.

Supplementary Table 2. Performance of selected secondary antibody dyes in proExM.

Dye	Ex max, nm	Em max, nm	Brightness in proExM as % of post antibody stain	Source
DyLight405	400	421	28±5	Life Technologies
CF405M	408	452	51±4	Biotium
Alexa488	495	519	48±2	Life Technologies
Alexa546	556	573	68±3	Life Technologies
Alexa594	590	617	46±2	Life Technologies
CF633	630	650	51±10	Biotium
Alexa647	650	668	7±3	Life Technologies
Atto647N	644	669	55±2	Sigma

Supplementary Table 3. Performance of selected photoswitchable and photoactivatable FPs in proExM.

Protein	Ex max, nm	Em max, nm	Molecular brightness relative to EGFP, %	Brightness in proExM cells, % of live cells	Addgene plasmid code	Reference
Dendra2	490	507	68	21±3	57725	78
	553	573	58	ND		
mEos2	506	519	143	45±9	57384	79
	573	584	92	ND		
mKikGR	505	515	102	31±2	57326	80
	580	591	53	ND		
PATagRFP	562	595	76	66±7	NA ^a	81

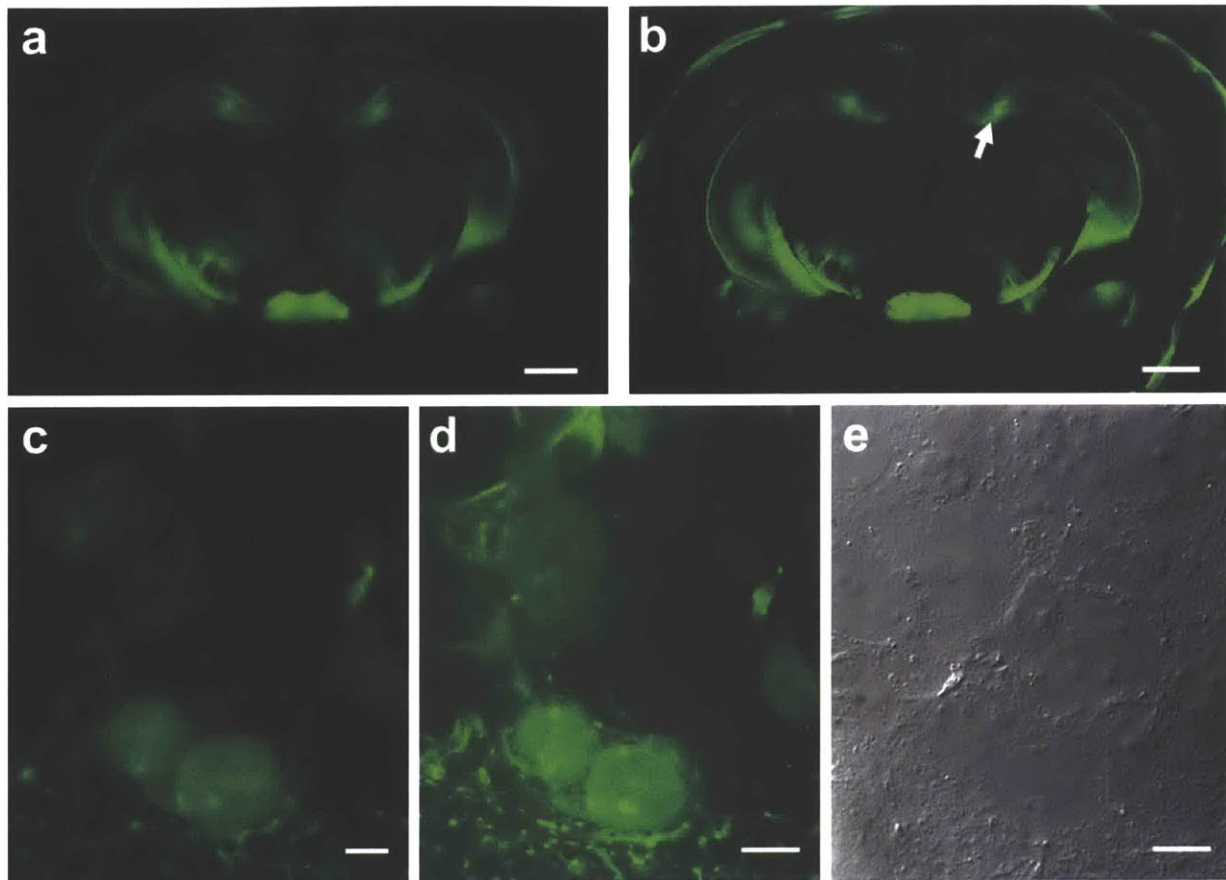
^aPATagRFP gene from Addgene plasmid 31945 was swapped with LSSmOrange gene in Addgene plasmid 37133.

ND, not determined.

Supplementary Table 4. Primary antibodies used.

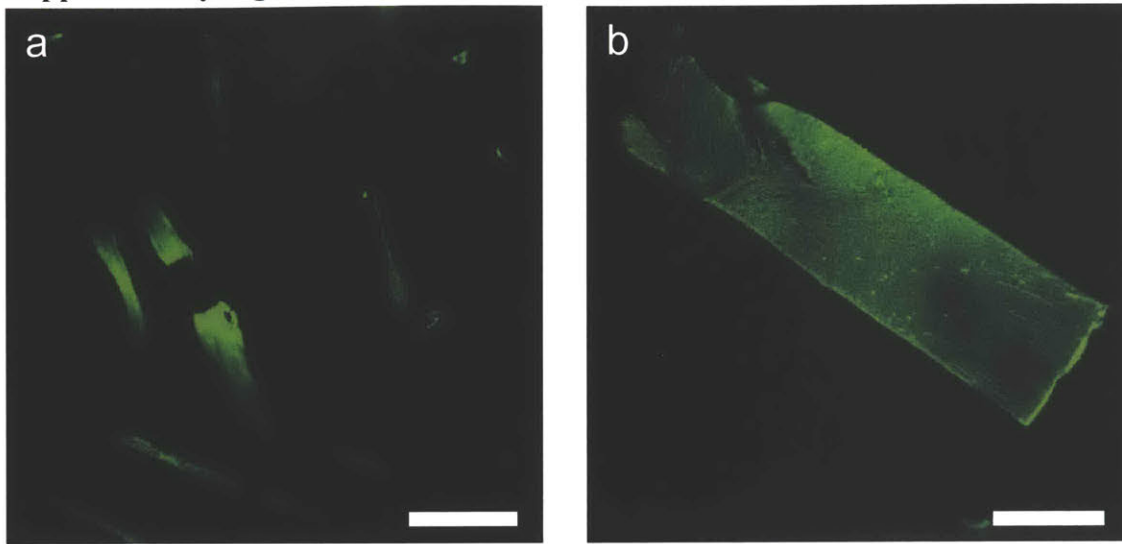
Target	Host	Clonality	Manufacturer	Catalog No.
GFP	chicken	poly	Abcam	ab13970
GFP	rabbit	poly	Life Technologies	A11122
bassoon	mouse	mono	Abcam	ab82958
homer	rabbit	mono	Abcam	ab184955
homer	rabbit	poly	Synaptic Systems	160 003
lamin A/C	mouse	mono	Cell Signaling Technologies	4777S
TOM20	rabbit	poly	Santa Cruz Biotech	sc-11415
post-synaptic density 95	mouse	mono	Neuromab	73-028
glutamic acid decarboxylase	rabbit	poly	Millipore	AB1511
myelin basic protein	rabbit	poly	Abcam	ab40390
vimentin	chicken	poly	Abcam	ab24525
glial fibrillary acid protein	mouse	mono	Santa Cruz Biotech	sc-166458

Supplemental Figure 1. Pre- and post-expansion images of a Thy1-YFP mouse brain slice treated with AcX and LysC mild digestion method.



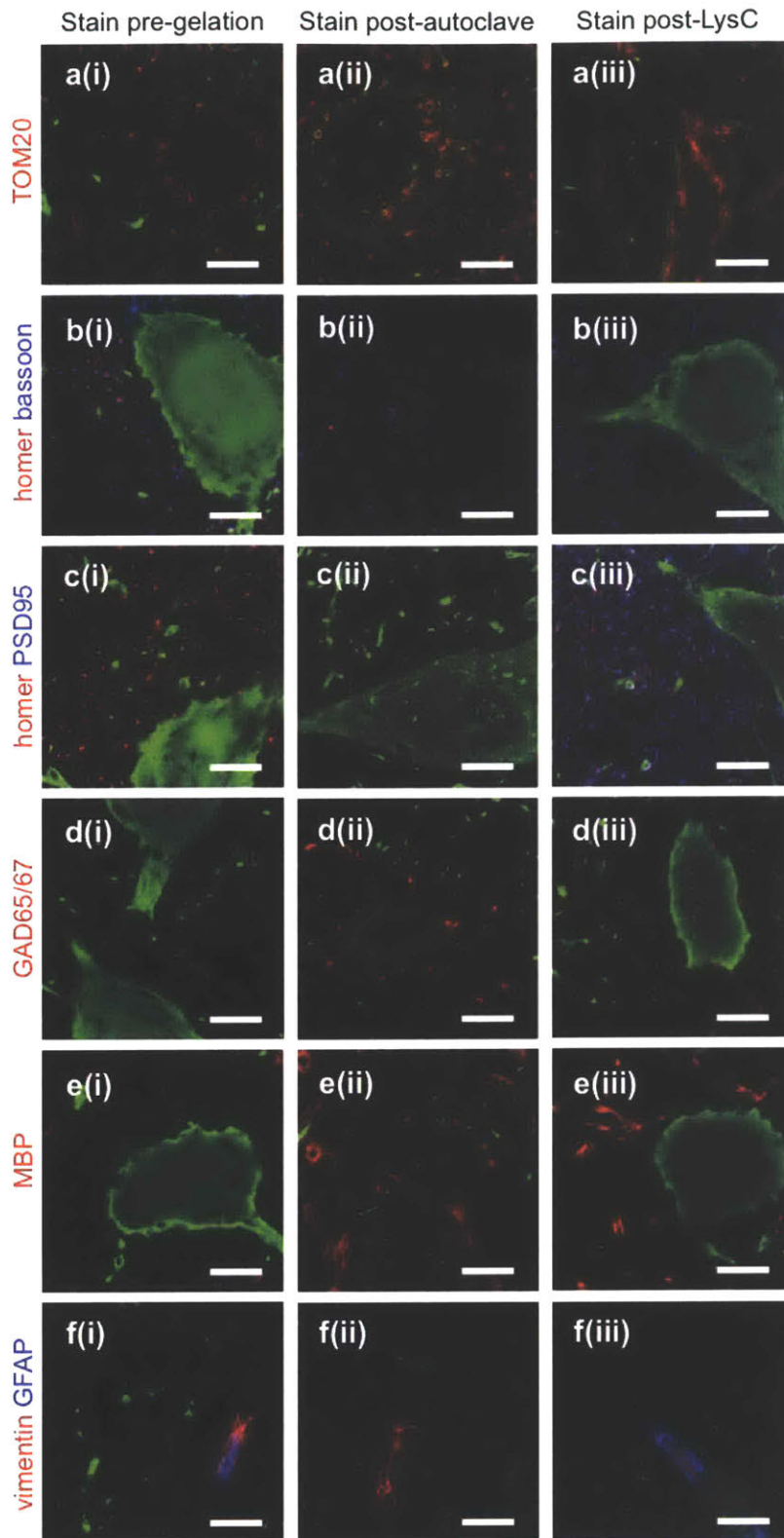
(a) Pre-expansion wide-field image. **(b)** Post-expansion wide-field image. The arrow indicates the location of images **(c-e)**. The bright edge surrounding the slice was the result of scattering at the gel-air interface. **(c)** Pre-expansion confocal image of a selected region of interest in hippocampus. **(d)** Post-expansion confocal image of the same selected region as **(c)**. **(e)** Post-expansion DIC image of the same selected region as shown in **(d)**. Scale bars: **(a)** 1 mm, **(b)** 4 mm (post-expansion units), **(c)** 5 μ m, **(d-e)** 20 μ m (post-expansion units).

Supplementary Figure 2. Incomplete homogenization with autoclave and LysC methods.



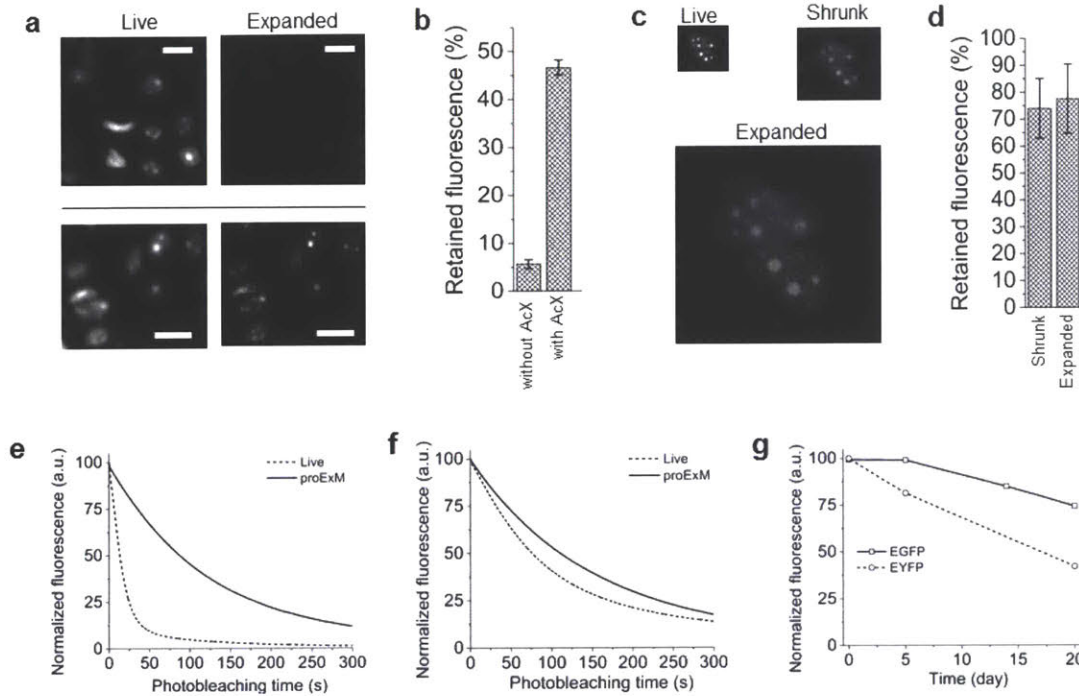
Fluorescence images of Thy1-YFP expressing mouse cerebral cortex, with YFP stained with anti-GFP using confocal imaging after autoclave treatment and antibody staining, showing a discontinuous neurite not residing at the surface of the imaged volume (**a**), and using widefield imaging after LysC treatment and antibody staining, showing defects in the expansion regions containing white matter tracts (**b**). Scale bars; (a) 5 μ m (~20 μ m), (b) 0.5mm (~2mm).

Supplementary Figure 3. Comparison of immunostaining methods with autoclave, LysC, and pre-gelation antibody treatment.

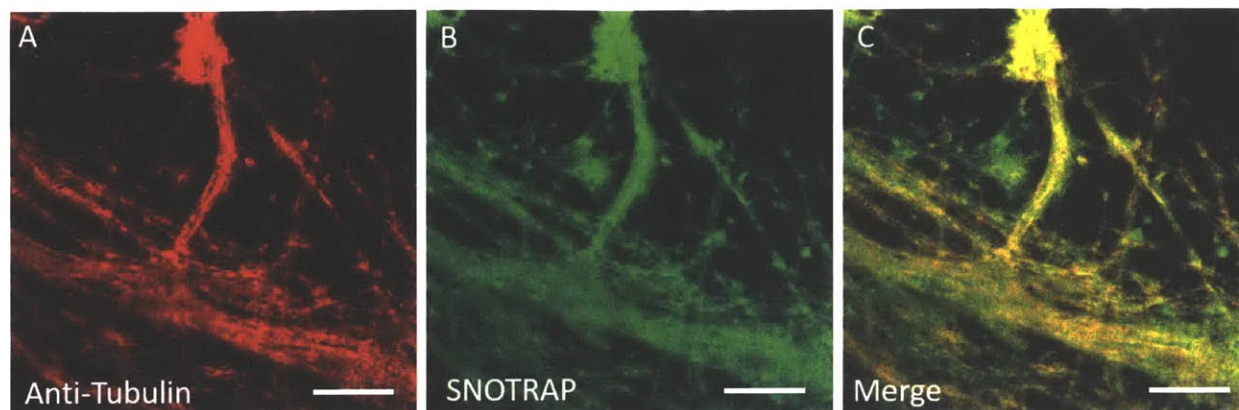


Confocal images of Thy1-YFP expressing mouse cerebral cortex, immunostained pre-gelation followed by AcX treatment, gelation, and proteinase K digestion (proExM), column **(i)**. Thy1-YFP brain samples immunostained after AcX treatment and gelation followed by autoclave treatment, column **(ii)**, or by LysC digestion column **(iii)**. Autoclave and LysC specimens all have YFP stained with anti-GFP (green) in addition to TOM20 (row **(a)**), homer (red) and bassoon (blue) (row **(b)**), homer (red) and post-synaptic density 95 (PSD95, blue) (row **(c)**), glutamic acid decarboxylase (GAD) 65/67 (row **(d)**), myelin basic protein (MBP, row **(e)**), and vimentin (red) and glial fibrillary acidic protein (GFAP, blue) (row **(f)**). Scale bars; 5 μ m (~20 μ m).

Supplementary Figure 4. Control experiments of retention of EGFP and EYFP fluorescence in HEK293FT cells after proExM.

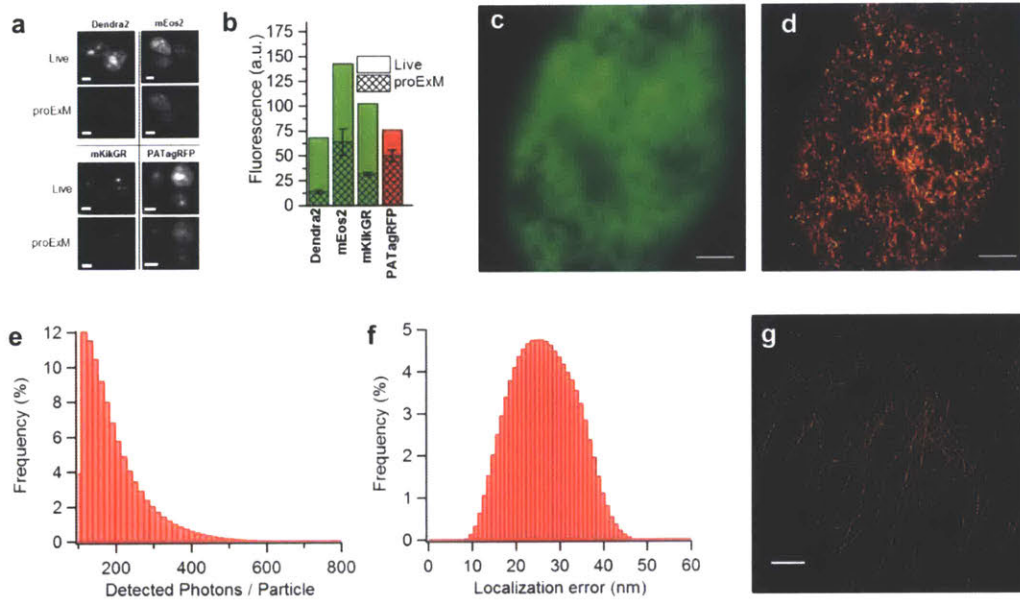


Supplementary Figure 5. ProExM imaging of S-nitrosylation.

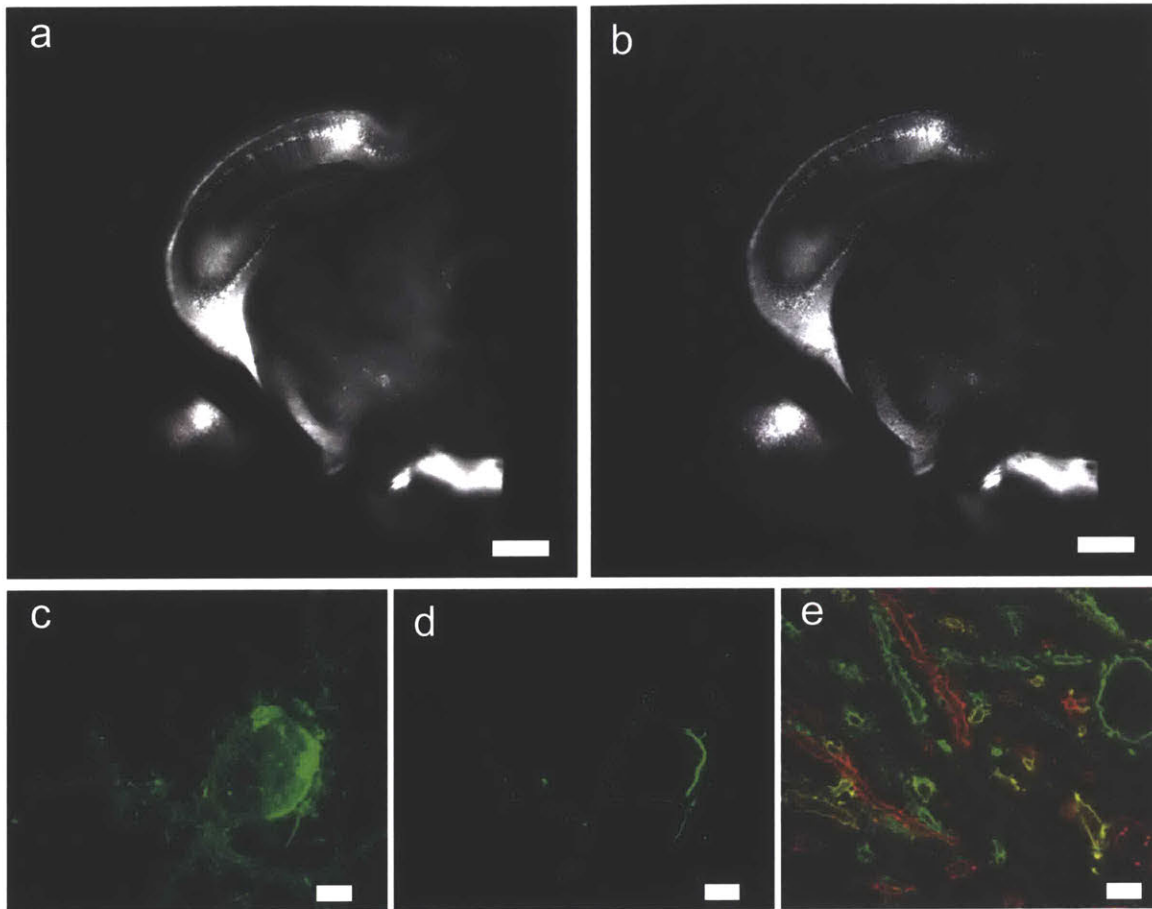


(a) ProExM of tubulin fibers stained with Anti-Tubulin in primary neuron culture. (b) ProExM of fluorescently labeled streptavidin bound to biotinylated cysteine S-nitrosylated proteins chemically tagged via the SNOTRAP method. (c) Color composite of (a) and (b) (tubulin, red; SNOTRAP, green).

Supplementary Figure 6. Performance of selected photoswitchable and photoactivatable FPs in proExM.

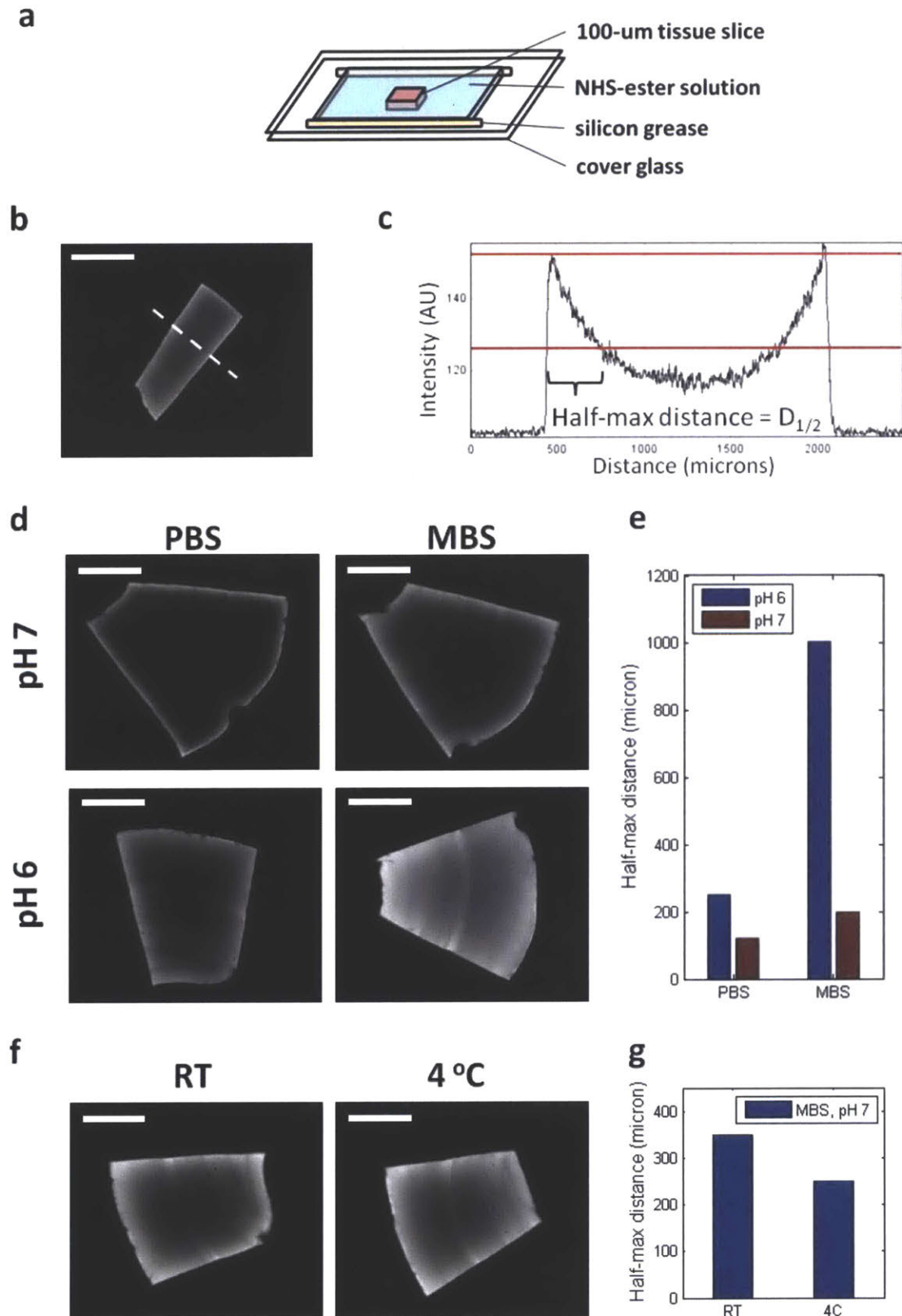


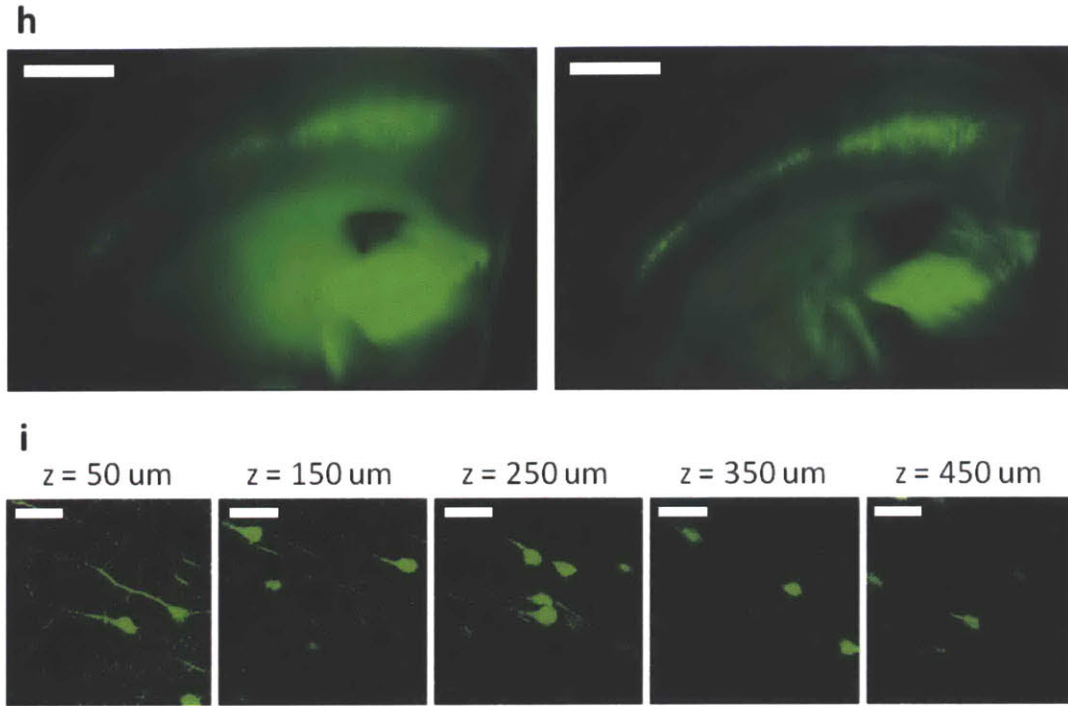
Supplementary Figure 7. Pre- and post- expansion images of a Thy1-YFP mouse brain slice, and mouse brain with Brainbow 3.0 fluorescent proteins, and treated with proExM.



(a) Pre-expansion wide-field image of Thy1-YFP brain slice. **(b)** Post-expansion wide-field image of the slice from **a**. **(c)** Post-expansion maximum intensity projection image ($\sim 10 \mu\text{m}$ in Z) of membrane bound GFP in Brainbow 3.0 mouse brain tissue. **(d)** One Z slice of the image from **c**. **(e)** Post-expansion imaging of two color imaging of membrane bound GFP and membrane bound mCherry in in Brainbow 3.0 mouse tissue. Scale bars: **(a)**, **(b)** $500 \mu\text{m}$ ($20.5 \mu\text{m}$). **(c-e)** $5 \mu\text{m}$ ($\sim 20 \mu\text{m}$).

Supplementary Figure 8. Optimizing AcX penetration depth in fixed brain tissue.





(a) Chamber assay for measuring penetration depth of a NHS-ester mixture (99% AcX + 1% NHS-biotin, which has similar molecular weight and charge as AcX) from the side of a tissue slice. After overnight treatment with the NHS-ester mixture, slices were retrieved, washed and treated with fluorophore-conjugated streptavidin to visualize penetration of NHS-ester mixture. (b) Representative image of a 100- μ m-thick mouse brain slice stained under the chamber assay conditions. Scale bar 1mm. (c) Fluorescent intensity along the line-cut represented as the white dashed line in b. The distance over which the intensity drops from maximum to half of its value ($D_{1/2}$) is a characteristic length for the depth of NHS-ester penetration. (d, e) Staining with MES-based saline (MBS; 100 mM MES + 150 mM NaCl) yields significantly improved depth of NHS-ester penetration than phosphate-based saline (PBS) over all pH levels tested. Scale bar 1 mm. (f, g) Staining at 4°C yields moderately greater depth of penetration than at RT. Scale bar 1 mm. (h) Representative images of native YFP fluorescence in a 500- μ m-thick Thy1-YFP mouse brain slice, before (left) and after (right) proExM. Scale bar 1 mm (pre-expansion units). (i) Confocal imaging demonstrates YFP fluorescence retention at the center of the 500- μ m-thick slice after an overnight AcX treatment with MBS, pH 6.0. Scale bar 100 μ m (post-expansion units).

Methods

Fluorescent Protein Screening

Most of the mammalian plasmids were obtained from Addgene (**Supplementary Table 1 and 3**). To construct the remaining ones, pmKate2-H2B-N1 and pPAtagRFP-H2B-N1 plasmids the respective genes were PCR amplified as *AgeI/NotI* fragments and swapped with the LSSmOrange gene in pH2B-LSSmOrange-N1 (Addgene). To generate NLS-iRFP fusion protein, a PCR-amplified *AgeI/NotI* fragment encoding gene of iRFP was swapped with LSSmKate2 gene in pNLS-LSSmKate2-N1 (Addgene plasmid #31871). HEK293FT (Invitrogen) and HeLa (ATCC CCL-2) cells were cultured in DMEM medium (Cellgro) supplemented with 10% FBS (Invitrogen), 1% penicillin/streptomycin (Cellgro), and 1% sodium pyruvate (BioWhittaker). HEK293FT and HeLa cells were used for ease of transfection, cell lines were authenticated by STR-profiling and checked for mycoplasma contamination by the manufacturer. Cells were transfected using TransIT-X2 transfection reagent (Mirus Bio) according to the manufacturer's protocol. Wide-field imaging of live HEK293FT cells was performed 24 h after transfection using a Nikon Eclipse Ti inverted microscope equipped with 10x NA 0.3 objective lens, a SPECTRA X light engine (Lumencor) with 390/22 nm, 438/24 nm, 475/28 nm, 510/25 nm, 585/29 nm, and 631/28 nm exciters (Semrock), and a 5.5 Zyla camera (Andor), controlled by NIS-Elements AR software. Immediately after live cell imaging cell cultures were fixed with 4% paraformaldehyde for 10 min, and permeabilized with 0.1% Triton-X for 15 min, washed 3 times for 5 minutes with PBS (Cellgro) and treated with 0.1 mg/ml AcX (LifeTechnologies) for at least 6 h, gelled and digested with proteinase K overnight as described below (see "AcX treatment" and "Gelation, digestion and expansion" sections).

Following digestion, the samples were processed by extensively washing with PBS, and then shrunk in 1 M NaCl and 60 mM MgCl₂ (except for YFP, which is chloride sensitive⁸², and thus was measured in the expanded state). For control experiments shown on **Supplementary Fig. 4** gels were washed only with PBS. Registration of pre- and post-sample processing images was carried out with an implementation of the SIFT/RANSAC algorithm, in MATLAB. Automatic Otsu thresholding via CellProfiler⁸³ of fluorescent nuclei allowed for automated measurement of fluorescent intensity in the same set of cells before and after sample processing. Intensity measurements for each nucleus before and after sample processing were normalized by segmented area to account for fluorophore dilution (area was used since epifluorescent optical sectioning mitigates the axial expansion effect on brightness).

Quantification of fluorescent dye retention during ProExM

Fluorescent secondary antibodies (goat anti-rabbit, 10 µg/mL) were purchased from commercial vendors (see **Supplementary Table 2** for list of fluorescent secondary antibodies). Retention (**Fig. 2c**) was quantified via before-after proExM imaging mouse cortex as described below. Cortical sections of wild type (only used for Alexa 488 due to Thy1-YFP crosstalk) and Thy1-YFP brain

slices (50 μm thick) were stained with anti-Homer primary antibody (Synaptic Systems; see **Supplementary Table 4**), and different secondary antibodies described in **Supplementary Table 2**. Epifluorescence images of brain slices were taken with 4x 0.13 NA objective pre-gelation. Following proExM gelation and digestion, the brain slices were washed extensively with PBS (3 x 30 min), and epifluorescence images of the slice were taken again with identical imaging conditions. A region of interest in the cortex was used to determine the loss of fluorescence during proExM processing. Intensity measurements before and after sample processing were normalized by segmented area to account for fluorophore dilution.

Structured illumination microscopy pre-expansion imaging

HeLa cells were fixed with 4% paraformaldehyde for 10 min, washed 3 times for 5 minutes with PBS, and permeabilized with 0.1% Triton-X for 15 min. Microtubules in fixed HeLa were stained with primary antibodies (Sheep Anti-Tubulin, Cytoskeleton ATN02) in blocking buffer 1x PBS with 0.1% Triton X-100 and 2% normal donkey serum (PBT) at a concentration of 10 $\mu\text{g}/\text{mL}$ for 1-4 hours and then washed in PBS three times for 5 minutes each. Specimens were then incubated with secondary antibodies (Donkey Anti-Sheep Alexa 488, Life Technologies, 10 $\mu\text{g}/\text{mL}$) in PBT for 1-4 hours and then washed in PBS three times for 5 minutes. 50 μm brain tissue slices were prepared and stained with primary and secondary antibodies (Rabbit Anti-Tom20, Santa Cruz Biotech sc-11415 and Goat Anti-Rabbit Alexa 568 (Life Technologies)) as described below. Super-resolution structured illumination microscope imaging was performed on a Deltavision OMX Blaze (GE healthcare) SIM microscope with 100x 1.40 NA (Olympus) oil objective. Stained cells were imaged with SlowFade Gold (Invitrogen) antifade reagent for suppression of photobleaching and refractive index matching for pre-expansion imaging.

Measurement Error Quantification

The same fields of view were imaged pre- and post-expansion. Post-expansion images were first registered to the corresponding pre-expansion images by rotation, translation and uniform scaling. In case the specimen tilt changed between pre- and post-expansion imaging, this was corrected using a 3D rotation without scaling using the Fiji 3D Viewer package. These scaled images were then registered again to the pre-expansion images, but this time with a B-spline-based non-rigid registration package in Matlab⁴⁰ to capture any non-uniformities in the expansion process. Control points for registration were automatically generated using scale-invariant feature transform (SIFT) keypoints⁸⁴. SIFT keypoints were generated using the VLFeat open source library⁸⁵, and random sample consensus (RANSAC) was used to estimate a geometric transformation limited to rotation, translation, and scaling. The vector deformation field mapping the scaled post-expansion image to the pre-expansion image expresses the shift of each point in the post-expansion image relative to an ideal uniform expansion. By subtracting the resulting vectors at any two points, we find the relative localization error in using the post-expansion image to measure the distance between those

two points. We sample the entire population of possible point-to-point measurements and find the root-mean-square error for such measurements as a function of measurement length.

Brainbow3.0 injection and antibody staining

Brainbow3.0 rAAV (University of Pennsylvania, Penn Vector Core) injections were performed as previously described⁵¹. Briefly, transgenic mice were anesthetized continuously with isoflurane and head-fixed to a stereotaxic apparatus. Surgery took place under sterile conditions with the animal lying on a heating pad. 2 μ L AAV mix (7.5×10^{12} genome copy/mL) was injected at a rate of 0.2 μ l/min through a 34-gauge injection needle into the brain (e.g., cortex, hippocampus), after which the needle was allowed to rest at the injection site for 5 min to allow viral diffusion. Animals expressed virus for 3-4 weeks, then were perfused (see “Mouse perfusion”).

Primary antibodies against Brainbow 3.0 fluorophores (chicken anti-GFP, guinea-pig anti-mKate2, rat anti-mTFP) were produced by the Cai lab. Slices were permeabilized and blocked with 1x PBS with 0.1% Triton X-100 and 2% normal donkey serum (PBT) for 30 minutes before antibody staining (all incubations at room temperature (RT)). Slices were incubated with primary antibodies for 3 days at 4°C in PBT, and then washed four times 30 minutes with PBT. Slices were incubated with secondary antibodies for 1 day at RT. Secondary antibodies used were: goat Anti-Chicken Alexa 488, goat Anti-Rat Alexa 546 (Life Technologies) and donkey Anti-Guinea Pig CF633 (Biotium), all at 10 μ g/mL.

Mouse perfusion

All solutions below were made up in 1x phosphate buffered saline (PBS). Mice were anesthetized with isoflurane and perfused transcardially with ice cold 4% paraformaldehyde. Brains were dissected out, left in 4% paraformaldehyde at 4°C for one day, before moving to 100 mM glycine. Slices (50 μ m, and 100 μ m) were sliced on a vibratome (Leica VT1000S) and stored at 4°C until staining.

AcX treatment

Acryloyl-X, SE (6-((acryloyl)amino)hexanoic acid, succinimidyl ester, here abbreviated AcX; Thermo-Fisher) was resuspended in anhydrous DMSO at a concentration of 10 mg/mL, aliquoted and stored frozen in a desiccated environment. AcX prepared this way can be stored for up to 2 months. For anchoring, cells and tissue slices are incubated in AcX diluted in PBS at a concentration of 0.1 mg/mL for > 6 hours, at room temperature. For thick tissue (> 100 microns), AcX penetration depth and labeling uniformity can be improved by incubating the sample at lower pH, at lower temperature, and in a 2-(N-morpholino)ethanesulfonic acid (MES)-based saline (100 mM MES, 150 mM NaCl; **Supplementary Figure 8**). Tissue slices can be incubated on a shaker or rocker to ensure mixing during the reaction.

Gelation, digestion and expansion

For AcX anchored fluorescent proteins and antibody staining, the following steps - gelation, digestion and expansion - can be performed as described previously⁴¹. Briefly, monomer solution (1x PBS, 2 M NaCl, 8.625% (w/w) sodium acrylate, 2.5% (w/w) acrylamide, 0.15% (w/w) N,N'-methylenebisacrylamide) was mixed, frozen in aliquots, and thawed before use. Monomer solution was cooled to 4°C before use. Concentrated stocks (10% w/w) of ammonium persulfate (APS) initiator and tetramethylethylenediamine (TEMED) accelerator were added to the monomer solution up to 0.2% (w/w) each. For slices, the inhibitor 4-hydroxy-2,2,6,6-tetramethylpiperidin-1-oxyl (4-hydroxy-TEMPO) was added up to 0.01% (w/w) from a 0.5% (w/w) stock to inhibit gelation during diffusion of the monomer solution into tissue sections. Cells or tissue slices were incubated with the monomer solution plus APS/TEMED (and 4-hydroxy-TEMPO for slices) at 4°C for one minute, 30 minutes for cultured cells, and brain slices respectively, and then transferred to a humidified 37°C incubator for two hours for gelation.

Proteinase K (New England Biolabs) was diluted 1:100 to 8 units/mL in digestion buffer (50 mM Tris (pH 8), 1 mM EDTA, 0.5% Triton X-100, 1 M NaCl) and incubated with the gels fully immersed in proteinase solution overnight at RT (this step can also be performed at 37°C for 4 hours). Digested gels were next placed in excess volumes of doubly de-ionized water for 0.25-2 hours to expand, with longer times for thicker gels. This step was repeated 3-5 times in fresh water, until the size of the expanding sample plateaued.

Fluorescence microscopy after expansion

Post-expansion confocal imaging of cells was performed on an Andor spinning disk (CSU-X1 Yokogawa) confocal system with a 60x 1.40 NA oil objective (**Fig. 2**). To quantify expansion factor for tissue slices and low-magnification before vs. after comparisons, specimens were imaged pre-ExM on a Nikon Ti-E epifluorescence microscope with a 4x 0.13 NA air objective (**Fig 3. a-d, Supp. Fig. 1a-b, Supp. Fig. 2b, Supp. Fig. 4a-g, and Supp. Fig. 7a, 7b**). For **Fig. 4a-b**, tissue slices were imaged on Nikon Ti-E epifluorescence microscope with a 10x 0.45 NA. Otherwise, all other tissues presented were imaged using an Andor spinning disk (CSU-X1 Yokogawa) confocal system with a 40x 1.15 NA water immersion objective (Nikon) with the exception of **Fig. 1, Supp. Fig. 2a, Supp. Fig. 3, and Supp. Fig. 5**, where a Zeiss LSM 710 with 40x 1.1 NA water objective. The Zeiss LSM 710 with 10x 0.3 NA air lens was used for **Supp. Fig. 8i**.

To stabilize the gels against drift during imaging following expansion, gels were placed in glass bottom 6 well plates with all excess liquid removed. If needed for immobilization, liquid low melt agarose (2% w/w) was pipetted around the gel and allowed to solidify, to encase the gels before imaging.

PALM imaging

PALM data was recorded on a custom-built three-camera RAMM frame microscope (ASI) using an Olympus 1.4 NA PLAPON 60x OSC objective, and a custom tube lens (LAO-300.0, Melles Griot), resulting in 100x overall magnification⁸⁶. A 2 mm thick quad-band excitation dichroic

(ZT405/488/561/640rpc, Chroma), a 2 mm thick emission dichroic (T560lpxr, Chroma), and a band-pass emission filter (FF01-609/54-25, Semrock) filtered the emitted light. Dendra2 was photoconverted by 100 μ s long excitation pulses of 405 nm (50 W/cm^2) every 200 ms, which was ramped up to 1.2 ms long pulses every 200 ms during the course of image acquisition. Stroboscopic 405-nm excitation of the Stradus 405-100 laser (Vortran) was achieved using a NI-DAQ-USB-6363 acquisition board (National Instruments), Photoconverted Dendra2 molecules were excited with a 555-nm DPSS laser (CrystaLaser) at estimated sample power levels of 2 kW/cm^2 . Fluorescence was detected using μ Manager (v. 1.4.20)⁸⁷ with a back-illuminated EMCCD camera (Andor Technology, Ixon Ultra DU-897_BV, 17 MHz EM amplifier, Gain 500, full-chip) at 20 frames/s.

Particle localization

Localizer⁸⁸ was used for 8-way adjacency particle detection with 20 GLRT sensitivity and a PSF of 1.3 pixels. The resulting particles were drift corrected using ad-hoc fiducial markers. For each detected particle, integrated fluorescence intensities were converted to photon counts using analysis routines written in Igor Pro version 6.36. The mean and median localization errors were determined using equation 6 in reference⁸⁹.

ProExM of different tissue types

Standard histology preparations of mouse normal fresh frozen tissue sections, postfixed with cold acetone, of pancreas, spleen and lung (5-10 μ m) were obtained from US Biomax (MOFTS036, MOFTS051, and MOFTS031, respectively). Tissues were blocked with 1x PBS with 0.1% Triton X-100 and 2% normal donkey serum (PBT) for 30 minutes before antibody staining. Tissues were stained with primary chicken anti-vimentin (Abcam) for 4 hours at RT and then washed four times 30 minutes with PBT. Slices were incubated with secondary antibodies for 2 hours at RT (Anti-Chicken Alexa 488, Life Technologies). Pre-expansion imaging was performed as described above. Tissues were incubated with 0.05 mg/mL AcX in PBS at RT overnight before gelation, digestion and expansion described above with the exception that digestion was performed at 60°C for 4 hours.

Antibody staining of endogenous proteins

Specimens, either before gelation or after autoclave or LysC treatment, were incubated in 1x PBS with 0.1% Triton X-100 and 2% normal donkey serum (PBT) at room temperature (RT) for 2 hours for blocking, and in the case of pre-gelation specimens, permeabilization. Specimens were incubated with primary antibodies at 3 μ g/mL in PBT, for 4 hours (RT), and then washed four times 30 minutes with PBT. Specimens were incubated with secondary antibodies at 20 μ g/mL in PBT, for 4 hours (RT), and then washed four times at least 30 minutes with PBT. Secondary antibodies used were: goat Anti-Chicken Alexa 488 (Life Technologies), goat Anti-Rabbit Alexa 546 (Life Technologies) and goat Anti-Mouse CF633 (Biotium), except that goat Anti-Chicken

Alexa 546 (Life Technologies) was used for **Fig. 1e, g(ii), h(ii)** and goat Anti-Rabbit Alexa 488 (Life Technologies) was used for **Fig. 1e**.

Specimen disruption using autoclave

After gelation, gels were recovered from gelation chambers and washed in 1M NaCl. Gels were washed for 15 minutes in Disruption Buffer (100mM Tris base, 5% Triton X-100, 1% SDS), then placed in fresh Disruption Buffer and treated by autoclave on liquid sterilization mode with a temperature of 121°C held for one hour. This treatment must be carried out in an autoclave-safe vessel such as polypropylene tubes. Gels were then transferred to well plates for antibody staining and imaging and washed in PBT (1xPBS, 2% normal donkey serum, 0.1% Triton X-100) to remove Disruption Buffer.

Mild digestion with LysC

After gelation, gels were pre-treated in HBSS buffer (with calcium and magnesium, ThermoFisher Scientific) with 600 U/ml collagenase type II (Life Technologies) in 37°C for 2-4 hours. Gels were then washed for 5 minutes in LysC digestion buffer (25 mM Tris-HCl, 1 mM EDTA, pH 8.5) and incubated with 33 µg/ml LysC (Promega) in 37°C for at least 8 hours. Finally, gels were washed in LysC digestion buffer 3x for 30 mins each and were subjected to immunostaining with identical steps that have been described above.

Synthesis of SNOTRAP-biotin

To a stirred 2-(diphenylphosphino)-benzenethiol (100mg, 0.34 mmol) in dry DMF (5 mL) was added biotin-PEG₃-propionic acid (100 mg, 0.22 mmol, ChemPep, Inc.), N,N'-dicyclohexylcarbodiimide (DCC) (70 mg, 0.34 mmol) and dimethylaminopyridine (DMAP) (4 mg, 0.03 mmol) successively. The resulting mixture was stirred for 7 h at room temperature, and the resulting clear solution then concentrated under reduced pressure and purified by flash chromatography (hexane/EtOAc/MeOH gradient) to give the desired product (yield 30%). The SNOTRAP probe was repurified on an 1100 HPLC system with a photodiode array UV detector at 254 nm (Agilent Technologies, Wilmington, DE). HPLC columns and solvent systems were as follows: a semi-preparative Phenomenex Luna C18 (25 cm × 9.4 mm, 10 µm) column was eluted with a linear gradient of 0.1% formic acid in water (A) and acetonitrile (B) at a flow rate of 2.5 mL/min. Solvent composition was initially at 40% for 5 min, 70% at 10 min, 90% at 20 min, and then further to 95% B over 8 min. ¹H NMR (500 MHz, CD₃CN, δ) 7.42-7.38 (m, 9H), 7.23-7.18 (m, 4H), 7.84 (m, 1H), 4.60-4.51 (m, 2H), 3.67-3.51 (m, 12H), 3.2 (m, 3H), 2.8 (m, 2H), 2.55 (t, 2H), 2.15 (t, 2H), 1.57-3.51 (m, 6H); ¹³C NMR (125 MHz, CD₃CN, δ) 199.19, 172.5, 164.5, 144.8, 138.1, 137.0, 134.8, 129.9, 129.6, 129.6, 118.3, 69.2, 63.1, 62.3, 45.9, 42.5, 38.2, 27.1, 23.1, 22.5; ³¹P NMR (202 MHz, CD₃CN, δ) -10.3; HRMS-ESI⁺ (*m/z*): [M + H]⁺ calculated for C₃₇H₄₇N₃O₆PS₂, 724.2638; found, 724.2632.

ProExM of SNOTRAP staining

For SNOTRAP staining, primary neuron culture were washed 3 X 5 minutes using PBS and fixed using cold methanol at -20°C for 15 minutes. Neurons were incubated with 300nM N-ethylmaleimide (NEM) (Thermo Scientific) in PBS-Triton X100 (0.3% v/v) at 37°C for 30 minutes to block the free -SH group on proteins. Cells were then washed 3 X 5 minutes using PBS and incubated with SNOTRAP probe (250uM) in acetonitrile-PBS-triton (50% : 50% v/v) at R.T. for 1 hour, and then further incubated with streptavidin-Alexa 488 (Thermo Scientific) in 1/500 dilution (PBS-Triton) at R.T. for 1 hour and afterwards washed 5 X 5 minutes. Antibody staining for anti-tubulin (Alexa 546 secondary) and proExM was performed as described above.

Animal care

All methods for animal care and use were approved by the Massachusetts Institute of Technology Committee on Animal Care and were in accordance with the National Institutes of Health Guide for the Care and Use of Laboratory Animals. One adult male rhesus macaque (*Macaca mulatta*) weighing 12kg was used for this study, as well as 1 C57BL/6 mouse, 4 Emx1-Cre mice, and 10 Thy1-YFP mice, ages ~1-3 months old. Mice were used without regard for gender.

Macaque procedures

Virus injections were performed with sevoflurane anesthesia using stereotactic coordinates to target 8 injection sites. Viruses (AAV8,) were centrifuged and loaded into 10µL gas-tight syringes (Hamilton) that had been back-filled with silicone oil (Sigma). A total of 3µL of virus was infused into the brain at two locations (deep then 500 µm superficial) at a rate of 100-200 nL/minute using stereotactic micromanipulator arms (David Kopf Instruments) and UMP3 micro-syringe injector pumps (World Precision Instruments). After each injection, the needle and syringe were left in place for 10 minutes before withdrawal. Blunt 33G needles were used for all injections. 1mg Dexamethasone was also administered to prevent brain swelling. Euthanasia took place 4 weeks after viral injection. An overdose of pentobarbital was administered prior to perfusion with phosphate buffered saline (PBS) and 4% paraformaldehyde (PFA). The brain was then extracted, blocked, and stored in a 20% glycerol with 0.1% sodium azide solution, and finally cut into 40µm microtome sections.

Chapter Four: Nanoscale Imaging of RNA with Expansion Microscopy

Introduction

Nanoscale-resolution imaging of RNA throughout cells, tissues, and organs is key for an understanding of local RNA processing, mapping structural roles of RNA, and defining cell types and states. However, it has remained difficult to image RNA in intact tissues with the nanoscale precision required to pinpoint associations with cellular compartments or proteins important for RNA function. Recently we developed an approach to physically magnify tissues, expansion microscopy (ExM)⁴¹. ExM isotropically magnifies tissues, enabling super-resolution imaging on conventional diffraction-limited microscopes. For example, $\sim 4\times$ linear expansion yields ~ 70 nm resolution using a ~ 300 nm diffraction-limited objective lens. In our original protocol, fluorophore tags were first targeted to proteins of interest via antibodies, and then anchored to a swellable polyelectrolyte gel synthesized *in situ*. Isotropic expansion was subsequently enabled by proteolytic treatment to homogenize specimen mechanical properties followed by osmotic swelling of the specimen-gel composite.

Here, we have developed a small molecule linker that enables RNA to be covalently attached to the ExM gel. We show that this procedure, which we call ExFISH, enables RNA fluorescent *in situ* hybridization (FISH), which enables identifying transcripts *in situ* with single molecule precision. In RNA FISH, a set of fluorescent probes complementary to a target strand of mRNA are delivered^{90,91}. Single molecule FISH (smFISH) can be performed with multiple fluorophores delivered to a single mRNA via oligonucleotide probes⁹². In intact tissues, amplification strategies, such as hybridization chain reaction (HCR)^{38,93} and branched DNA amplification^{94,95}, can enable a large number of fluorophores to be targeted to a single mRNA. We show that ExFISH can support smFISH in cell culture, and HCR-amplified FISH in intact mouse brain tissues. We demonstrate the power of ExFISH for revealing nanoscale structures of long non-coding RNAs (lncRNAs), as well as for localizing neural mRNAs to individual dendritic spines. ExFISH will be useful for a diversity of questions relating the structure and location of RNA to biological functions.

Results

ExFISH: Design and Validation of RNA Anchoring Chemistry

We first determined a strategy for covalently linking RNAs directly to the ExM gel. Although transcripts are crosslinked to proteins during fixation, the strong proteolysis of ExM precludes a reliance on proteins for RNA retention (**Supplementary Fig. 1**). We thus reasoned that covalently securing RNA molecules directly to the ExM gel via a small molecule linker would enable the interrogation of these molecules post-expansion. To achieve this aim, we synthesized a reagent from two building blocks: a molecule containing both an amine as well as an alkylating

group that primarily reacts to the N7 of guanine, and a molecule that contains an amine-reactive succinamide ester and a polymerizable acrylamide moiety. Commercially available reagents exist that satisfy each of these two profiles, such as Label-IT Amine (MirusBio) and 6-((Acryloyl)amino)hexanoic acid (Acryloyl-X SE, here abbreviated AcX, Life Technologies; all reagents are listed in **Supplementary Table 1**). We named this molecule, which enables RNA to be covalently functionalized with a free radical polymerizable group, LabelX (**Fig. 1a**). We verified that LabelX does not impede smFISH readout (**Supplementary Fig. 2**). We then designed a procedure where a sample could be treated with LabelX to make its RNAs gel-anchorable, followed by gel formation, proteolysis, and osmotic swelling as performed in the original ExM protocol. Once a sample was thus expanded, the RNAs could then be interrogated through FISH (**Fig. 1b**).

To quantify RNA transcript anchoring yield after expansion, we used smFISH probes targeting mRNAs of varying copy number (7 targets, with copy number ranging from ~10 to ~10,000 per cell, $n = 60$ cells across all 7 targets). smFISH images, taken with probes delivered before (**Fig. 1c**) and after (**Fig. 1d**) expansion, to the same cells, showed no loss of transcript detectability with expansion for both low- and high-copy number transcripts (**Fig. 1e**). The ratio of transcripts detected was near unity at low transcript counts (e.g., in the 10's), however, more transcripts were detected after expansion for highly expressed mRNAs (e.g., in the 1,000's) (**Supplementary Fig. 3, Supplementary Table 2**). This difference arises from the high density of smFISH spots for these targets in the un-expanded state, with the expansion process de-crowding spots that previously were indistinguishable. For example, for smFISH against *ACTB*, we were able to resolve individual *ACTB* mRNA puncta post-expansion even within transcriptional foci in the nucleus (**Fig. 1c**, versus **1d**), which can be dense with mRNA due to transcriptional bursting. Thus, ExFISH is capable of supporting single molecule RNA readout in the expanded state. Since Label-IT also reacts to DNA, the ExFISH process enables uniform expansion of the nucleus (**Supplementary Fig. 4**). The isotropy of ExFISH (**Supplementary Fig. 5**) was numerically similar to that observed when protein targets were labeled and expanded in the original ExM protocol⁴¹. In recent ExM protocols in which proteins are anchored to the same hydrogel as used in ExFISH, with a similar linker^{96,97}, the distortion is small (a few percent distortion, in cells and tissues). These earlier results, since they were obtained with similar polymer chemistry, serve to bound the ExFISH distortion. The expansion factor is slightly lower than in our original ExM paper (i.e., ~3.3× versus ~4×, expansion factors can be found in Figure Legends of this manuscript) due to the salt required to support hybridization of probes.

Nanoscale Imaging of lncRNA with ExFISH

We imaged long non-coding RNAs (lncRNAs) known to serve structural roles in cell biology. We imaged the lncRNA *XIST*, whose role in inactivating the X chromosome may depend on initial association with specific chromatin subregions through a process which is still being revealed⁹⁸. The pre-expansion image (**Fig. 1f**) shows two bright globular fluorescent regions, presumably corresponding to the X chromosomes of HEK cells undergoing inactivation⁹⁸⁻¹⁰⁰, but

post-expansion, individual puncta were apparent both within the globular regions as well as nearby (**Fig. 1g**). We additionally used ExFISH to examine the previously described¹⁰¹ ring-shaped morphology of ensembles of *NEAT1* lncRNAs (**Fig. 1h**), which has been hypothesized to play an important role in gene expression regulation and nuclear mRNA retention¹⁰². Before expansion, *NEAT1* presents in the form of bright, diffraction-limited puncta (**Fig. 1h, Fig. 1i**), but after expansion, the ring-shaped morphology becomes clear (**Fig. 1h, Fig. 1i**). Given the complex 3-D structure of the genome¹⁰³, mapping lncRNAs may be useful in defining key chromatin regulatory complexes and their spatial configurations.

Super-resolved, Multiplexed Imaging of RNA with ExFISH

The combination of covalent RNA anchoring to the ExM gel, and the de-crowding of the local environment that results from expansion, could facilitate strategies that have been proposed for multiplexed RNA readout^{104–106} based upon sequential hybridization with multiple probe sets. In order to facilitate multiple cycles of FISH, we re-embedded expanded specimens in charge-neutral polyacrylamide. This process allowed expanded gels to be immobilized for multi-round imaging, and additionally stabilized the expanded specimen throughout salt concentration changes in the protocol. Such re-embedded samples exhibited similar expansion factors as non-re-embedded samples (i.e., $\sim 3\times$), and were robust to multiple wash-stain cycles as assessed by repeated application of the same probe set (**Fig. 2a, Supplementary Fig. 6**, showing 5 rounds of smFISH staining against *GAPDH* on cultured cells). This stability was observed even under stringent wash conditions designed to minimize cycle-to-cycle crosstalk (e.g., 100% formamide). Across the 5 rounds, there was no distortion of the locations of individual RNA spots from round to round (**Fig. 2b**), nor variance in detection efficiency or signal-to-noise ratio (**Fig. 2c, 2d**). Having validated the cycle-to-cycle consistency, we next demonstrated the capability of multiplexed ExFISH by applying probes for *GAPDH*, *UBC*, *NEAT1*, *USF2*, *ACTB*, and *EEF2* in series, enabling 6 individual RNAs to be identified and localized in the same cell (**Fig. 2e, Supplementary Fig. 6**). Thus, serial FISH is applicable to samples expanded after securing RNA to the swellable polymer as here described, making it straightforward to apply probe sets computationally designed to yield more information per FISH cycle, e.g. MERFISH^{105–107}.

3D Nanoscale Imaging of RNA in Mouse Brain Tissue

ExM allows for facile super-resolution imaging of thick 3-D specimens such as brain tissue on conventional microscopy hardware⁴¹. We applied ExFISH to samples of Thy1-YFP mouse brain tissue²⁶, using the YFP protein to delineate neural morphology (**Fig. 3a, 3b**). Endogenous YFP protein was anchored to the polyacrylate gel via AcX using the proExM protocol⁹⁶, and RNA anchored via LabelX. Since smFISH yields signals too dim to visualize in intact tissues using confocal imaging, we applied the previously described technique of hybridization chain reaction (HCR)³⁸, in particular the next-generation DNA HCR amplifier architecture⁹³ (schematic in **Supplementary Fig. 7**). In samples containing mouse cortical and hippocampal regions, mRNAs for YFP (**Fig. 3c**) and glutamic acid decarboxylase 1 *Gad1* (**Fig. 3d**) were easily visualized using a widefield microscope, with YFP mRNA well localized to YFP-fluorescing cells (**Fig. 3e**), and *Gad1* mRNA localized to a population of cells with characteristic

arrangement throughout specific layers of the cortex and hippocampus¹⁰⁸. Examining brain specimens at high magnification using a confocal spinning disk microscope revealed that individual transcripts could be distinguished due to the physical magnification of ExM (**Fig. 3f**, with YFP and *Gad1* mRNA highlighted), with even highly overexpressed transcripts (e.g., YFP) cleanly resolved into individual puncta (**Fig. 3f**). When FISH probes were omitted, minimal background HCR amplification was observed (**Supplementary Fig. 8**). Given that ExM enables super-resolution imaging on diffraction limited microscopes, which can be scaled to very fast imaging speeds²⁹, we used a commercially available lightsheet microscope on a Thy1-YFP brain slice to enable visualization of multiple transcripts, with single molecule precision, throughout a volume of $\sim 575 \mu\text{m} \times 575 \mu\text{m} \times 160 \mu\text{m}$ thick in just 3 hours ($\sim 6 \times 10^{10}$ voxels in 3 colors; **Supplementary Fig. 9, Supplementary Video 1**).

HCR amplifies a target binding event into a bright fluorescent signal (**Supplementary Fig. 7**). A stringent method for assessing detection accuracy is to label individual RNAs with different probe sets bearing different colors^{109,110}, which shows that 50-80% of mRNAs thus targeted will be doubly labeled, when assessed in cell culture; a 50% co-localization is interpreted as $\sqrt{0.5} \sim 70\%$ detection efficiency (assuming probe independence); this is a lower bound as it excludes false positives. In order to assess the false positive and negative rates for single molecule visualization in expanded tissues, we delivered pairs of probe sets targeting the same transcript with different initiators. This scheme results in amplified fluorescent signals of two different colors from the same target (**Supplementary Fig 10**), giving a measure of the hybridization efficiency. Delivering probe sets against a nonexistent transcript also gives a measure of false positive rate. We delivered a probe set against a missense probe (*Dlg4* reversed, **Fig. 3g**) as well as a nonexistent transcript (mCherry, **Supplementary Table. 3**), using Thy1-YFP mouse brain samples, and found a low but nonzero spatial density of dim, yet amplified, puncta (1 per $61 \mu\text{m}^3$ in unexpanded coordinates, *Dlg4* reversed; 1 per $48 \mu\text{m}^3$, mCherry). Essentially zero of these puncta exhibited co-localization (0/1,209 spots, *Dlg4* reversed; 4/1,540 spots mCherry). In contrast, when a transcript was present (*Actb*), a large fraction of the puncta exhibited co-localization (an average of 58% of probes in one color co-localized with other color, 15,866/27,504 spots, **Fig. 3h, Supplementary Table 3**), indicative of a 75% detection efficiency, comparable to the non-amplified single molecule studies described above.

We used two-color HCR ExFISH against mRNAs to image their position within cellular compartments such as dendritic spines, which require nanoscale resolution for accurate identification or segmentation. We probed the *Dlg4* mRNA, which encodes the prominent postsynaptic scaffolding protein PSD-95, and which is known to be dendritically enriched⁹⁴. We obtained a degree of co-localization (53%, 5,174/9,795 spots) suggesting a high detection efficiency, 73% (**Fig. 3i**). We also probed the mRNA for *Camk2a*, finding a detection efficiency of 78% (co-localization, 61%, 8,799/14,440 spots, **Supplementary Fig 10**). We focused on puncta which were co-localized, thus suppressing false positive errors, and giving a lower-bound on transcript detection (**Supplementary Fig 10**). Focusing on individual dendrites in these expanded samples revealed that individual *Dlg4* (**Fig. 3j**) and *Camk2a* (**Fig. 3k**) mRNAs could indeed be

detected in a sparse subset of dendritic spines as well as fine dendritic processes. To facilitate multiplexed HCR readout, we developed modified HCR hairpins that can be disassembled using toe-hold mediated strand displacement¹¹¹ (**Supplementary Fig. 11**). These modified HCR amplifiers enable multiple cycles of HCR by disassembling the HCR polymer between subsequent cycles. Given that neurons can have tens of thousands of synapses, and mRNAs can be low copy number, the ability to map mRNAs at synapses throughout neuronal arbors may be useful for a diversity of questions in neuroscience ranging from plasticity to development to degeneration.

Discussion

We present a novel reagent, easily synthesized from commercial precursors, that enables RNA to be covalently anchored for expansion microscopy. The resulting procedure, ExFISH, enables RNAs to be probed through single-molecule FISH labeling as well as hybridization chain reaction (HCR) amplification. We validated RNA retention before versus after expansion, finding excellent yield, and de-crowding of RNAs for more accurate RNA counts and localization. This enabled us to visualize, with nanoscale precision and single molecule resolution, RNA structures such as XIST and NEAT1, long non-coding RNAs whose emergent structure has direct implications for their biological roles. The anchoring was robust enough to support serial smFISH, including repeated washing and probe hybridization steps, and multiplexed readout of RNA identity and location, implying that using probes designed according to specific coding strategies^{104–106} would support combinatorial multiplexing, in which each additional cycle yields exponentially more transcript information. The covalent anchoring of RNA to the ExM gel may also support enzymatic reactions to be performed in expanded samples – such as reverse transcription, rolling circle amplification (RCA), fluorescent *in situ* sequencing (FISSEQ)¹¹², and other strategies for transcriptomic readout or SNP detection¹¹³, within intact samples.

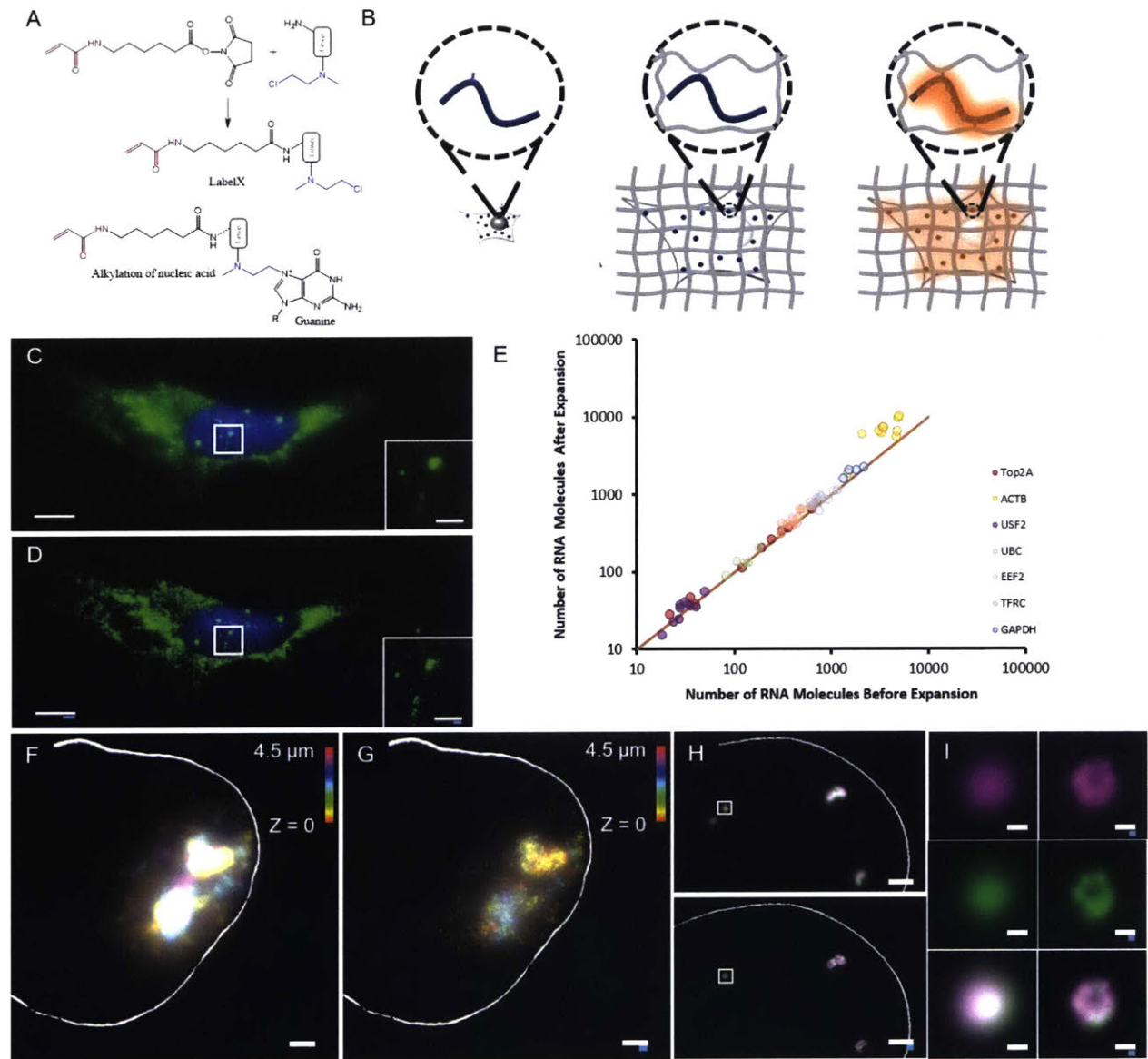
ExM, being a physical form of magnification, enables nanoscale resolution even on conventional diffraction limited microscopes. Expanding samples makes them transparent and homogeneous in index of refraction, in part because of the volumetric dilution, and in part because of washout of non-anchored components⁴¹. Thus, strategies combining ExM with fast diffraction limited methods like lightsheet microscopy²⁹ may result in “best of both worlds” performance metrics: the voxel sizes of classical super-resolution methods, but the voxel acquisition rates of increasingly fast diffraction limited microscopes⁴¹. The de-crowding of RNAs enables another key advantage: reducing the effective size of the self-assembled amplification product of HCR. An HCR amplicon of size 500 nm in the post-expanded sample would, because of the greater distance between RNAs, have an effective size of $500 / 3.5 = \sim 150$ nm. The lower packing density of amplicons facilitates the imaging of more transcripts per experiment¹⁰⁶ with nanoscale precision. Other methods of achieving brighter signals may be possible. For example, brighter fluorophores such as quantum dots¹¹⁴ or bottlebrush fluorophores¹¹⁵ could obviate the need for signal amplification, in principle. The expanded state may enable better delivery of these and other

bulky fluorophores into samples. Other amplification strategies may be possible as well, including enzymatic (e.g., RCA¹¹³, tyramide amplification¹⁰⁸, HRP amplification) as well as nonenzymatic (e.g., branched DNA) methods, although reaction efficiency and diffusion of reagents into the sample must be considered.

ExFISH may find many uses in neuroscience and other biological fields. In the brain, for example, RNA is known to be trafficked to specific synapses as a function of local synaptic activity¹¹⁶ and intron content¹¹⁷, and locally translated^{94,118,119}, and the presence and translation of axonal RNAs remains under investigation¹²⁰. We anticipate that, coupled to straightforward multiplexed coding schemes, this method can be used for transcriptomic profiling of neuronal cell-types *in-situ*, as well as for the super-resolved characterization of neuronal connectivity and synaptic organization in intact brain circuits, key for an integrative understanding of the mechanisms underlying neural circuit function and dysfunction. More broadly, visualizing RNAs within cells, and their relationship with RNA processing and trafficking machinery, may reveal new insights throughout biology and medicine.

Figures

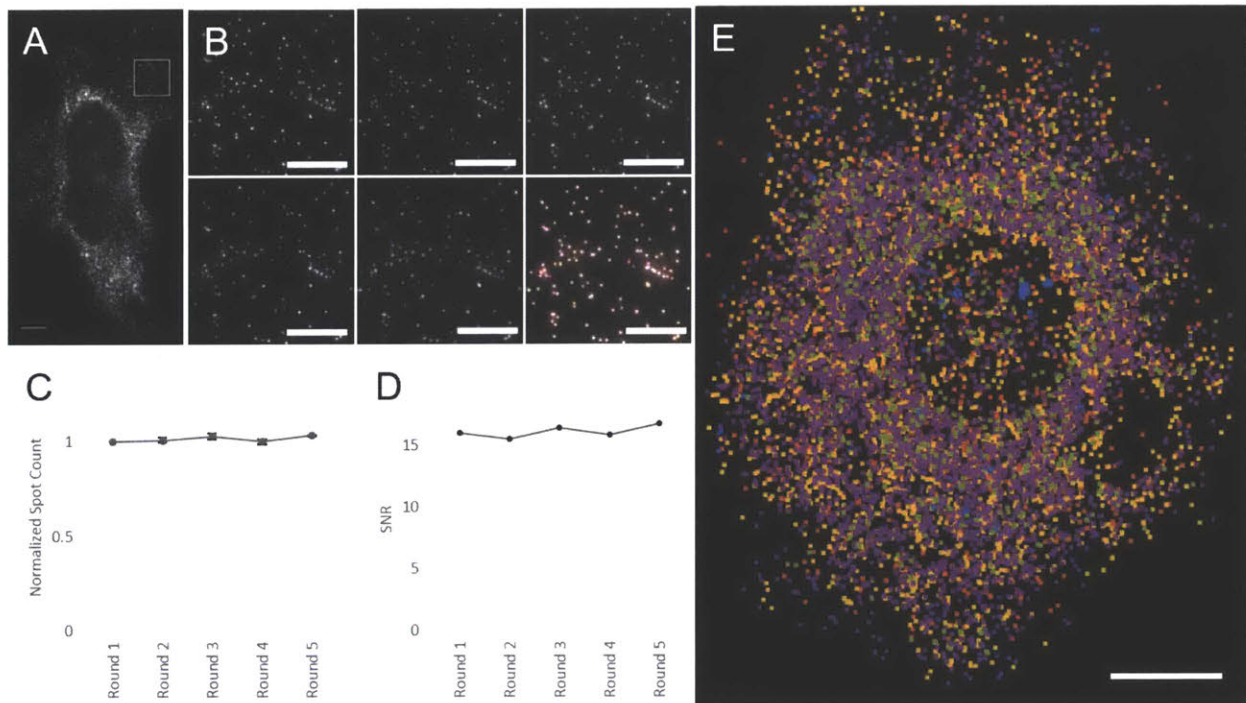
Figure 4-1. Design and validation of ExFISH chemistry.



(a) Acryloyl-X SE (top left) is reacted to Label-IT® amine (top right) via NHS-ester chemistry to form LabelX (middle), which serves to make RNA gel-anchorable by alkylating its bases (e.g., the N7 position of guanines) (bottom). (b) Workflow for ExFISH: biological specimens are treated with LabelX (left), which enables RNA to be anchored to the ExM gel (middle). Anchored RNA can be probed via hybridization (right), after gelation, digestion, and expansion. (c) smFISH image of *ACTB* before expansion. Inset shows zoomed-in region, highlighting transcription sites in nucleus. (d) As in (c), using ExFISH. (e) smFISH counts before versus after expansion for seven different transcripts ($n = 60$ cells; each symbol represents one cell). (f) smFISH image of *XIST*

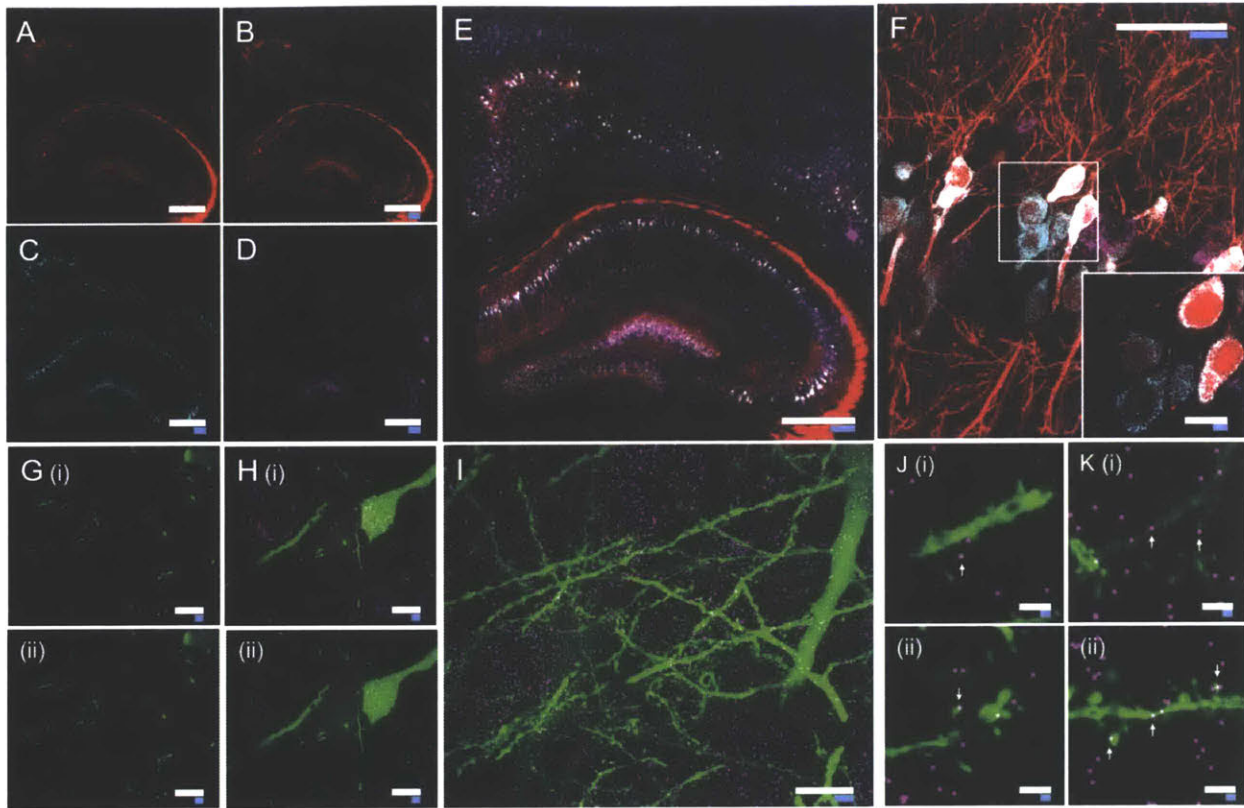
long non-coding RNA (lncRNA) in the nucleus of a HEK293 cell before expansion (white line denotes nuclear envelope in **f-h**). (**g**) As in (**f**), using ExFISH. (**h**) smFISH image before expansion (top), and using ExFISH (bottom), of *NEAT1* lncRNA in the nucleus of a HeLa cell. Magenta and green indicate probesets binding to different parts of the 5' (1-3756 nts) *NEAT1* (see Methods). (**i**) Insets showing a *NEAT1* cluster (boxed region of (**h**)) with smFISH (left) and ExFISH (right). Scale bars (white, in pre-expansion units; blue scale bars are divided by the expansion factor noted)): (**c, d**) 10 μm (expansion factor, 3.3 \times), inset 2 μm ; (**f, g**) 2 μm (3.3 \times), Z scale represented by color coding in pre-expansion units; (**h**) 2 μm (3.3 \times); (**i**) 200 nm (3.3 \times).

Figure 4-2. Serially hybridized and multiplexed ExFISH.

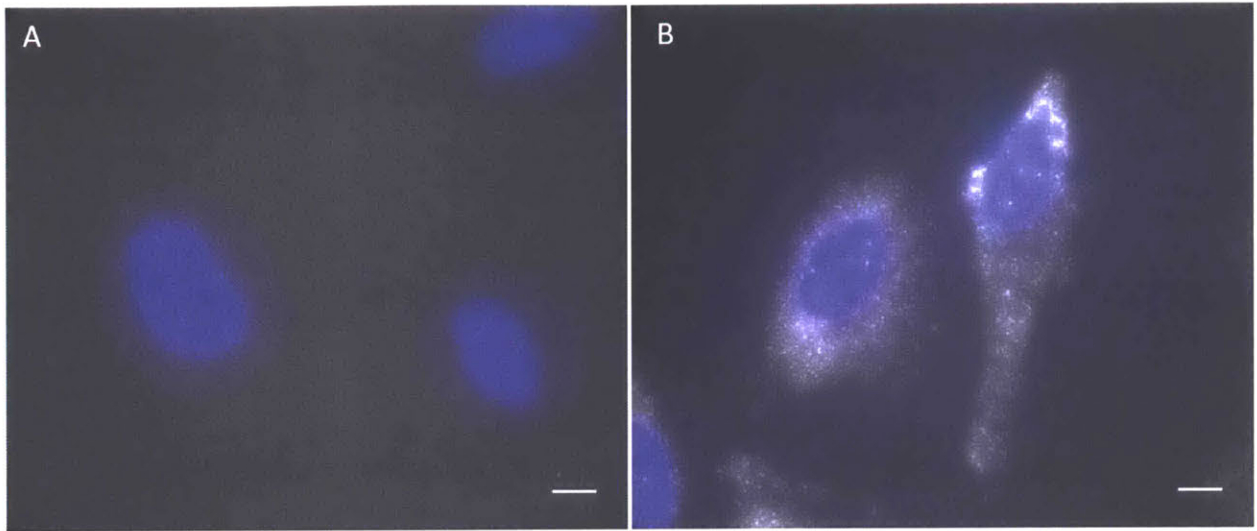


(**a**) Widefield fluorescence image of ExFISH targeting *GAPDH*. (**b**) Boxed region of (**a**), showing 5 repeated re-stainings following probe removal (see Methods); lower right panel, overlay of the 5 images (with each a different color, red, green, blue, magenta, yellow), showing co-localization. (**c**) ExFISH RNA counts for each round, normalized to the round 1 count; plotted is mean \pm standard error; $n = 3$ regions of (**a**). (**d**) Signal-to-noise ratio (SNR) of ExFISH across the five rounds of staining of (**a**), computed as the mean puncta brightness divided by the standard deviation of the background. (**e**) Composite image showing ExFISH with serially delivered probes against six RNA targets in a cultured HeLa cell (raw images in **Supplementary Fig. 6**); colors are as follows: *NEAT1*, blue; *EEF2*, orange; *GAPDH*, yellow; *ACTB*, purple; *UBC*, green; *USF2*, light blue. Scale bars (expanded coordinates): (**a**) 20 μm ; (**b**) 10 μm ; (**e**) 20 μm .

Figure 4-3. Nanoscale imaging of RNA in mammalian brain.

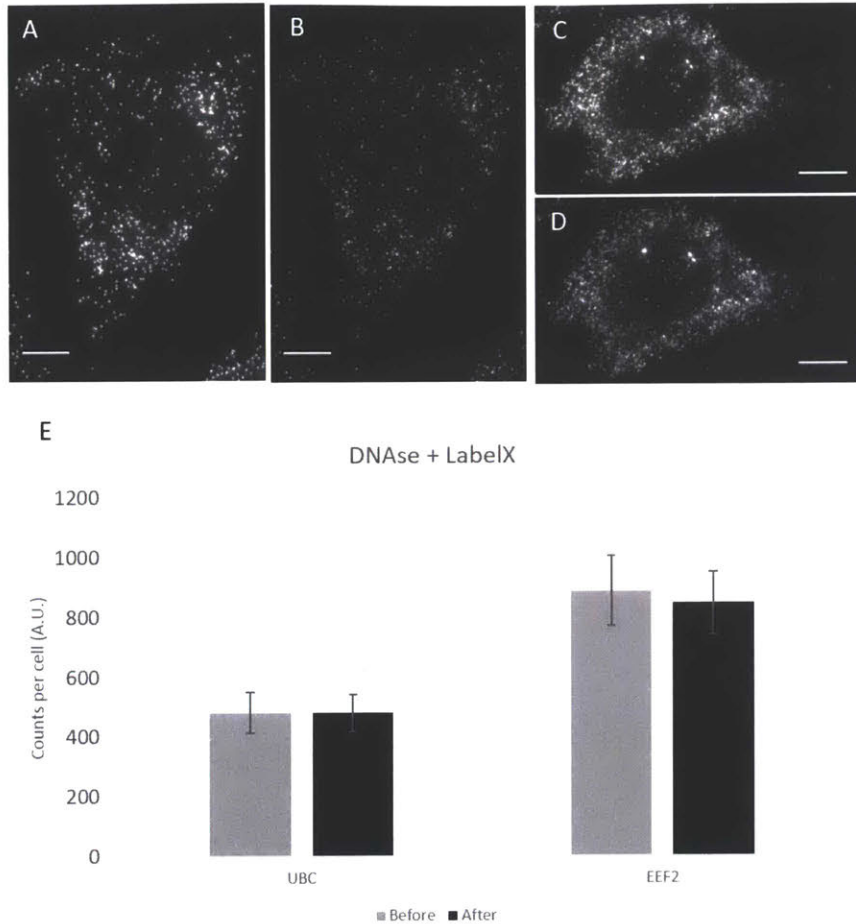


(a) Widefield fluorescence image of Thy1-YFP mouse brain. (b) Post-expansion widefield image of (a). (c) Widefield fluorescence showing HCR-ExFISH of YFP mRNA in the sample of (b). (d) As in (c), but for *Gad1* mRNA. (e) Composite of (b-d), highlighting distribution of *Gad1* versus Thy1-YFP mRNAs. (f) Confocal image of mouse hippocampal tissue from (e) showing single RNA puncta. Inset, one plane of the boxed region (red, YFP protein; cyan, YFP mRNA; magenta, *Gad1* mRNA). (g) Confocal image (i) and processed image (ii) of HCR-ExFISH using a missense *Dlg4* probe, in Thy1-YFP mouse tissue (green, YFP protein). The raw image (i) uses alternating probes in two colors (red, *Dlg4* missense even; blue, *Dlg4* missense odd). The processed image (ii) shows zero co-localized spots (magenta). (h) As in (g), but for HCR-ExFISH targeting *Actb* in Thy1-YFP mouse brain (green, YFP protein; red, *Actb* even, and blue, *Actb* odd in (i); co-localized spots in magenta (ii)). (i) Confocal image of hippocampal tissue showing co-localized *Dlg4* puncta (magenta) overlaid on YFP (green). (j) Dendrites with *Dlg4* mRNA localized to spines (arrows). (i), (ii), two representative examples. (k) As in (j), but with HCR-ExFISH of *Camk2a* mRNA showing transcripts in dendritic spines and processes. Scale bars (white, in pre-expansion units; blue scale bars are divided by the expansion factor noted): (a) 500 μm ; (b-e) 500 μm (expansion factor 2.9 \times); (f) 50 μm (2.9 \times), inset 10 μm ; (g-i) 10 μm (3 \times); (j,k) 2 μm (3 \times). (e,i) maximum-intensity projection (MIP) 27 μm thick (pre-expanded units); (g,h,j,k) MIPs \sim 1.6 μm thick.



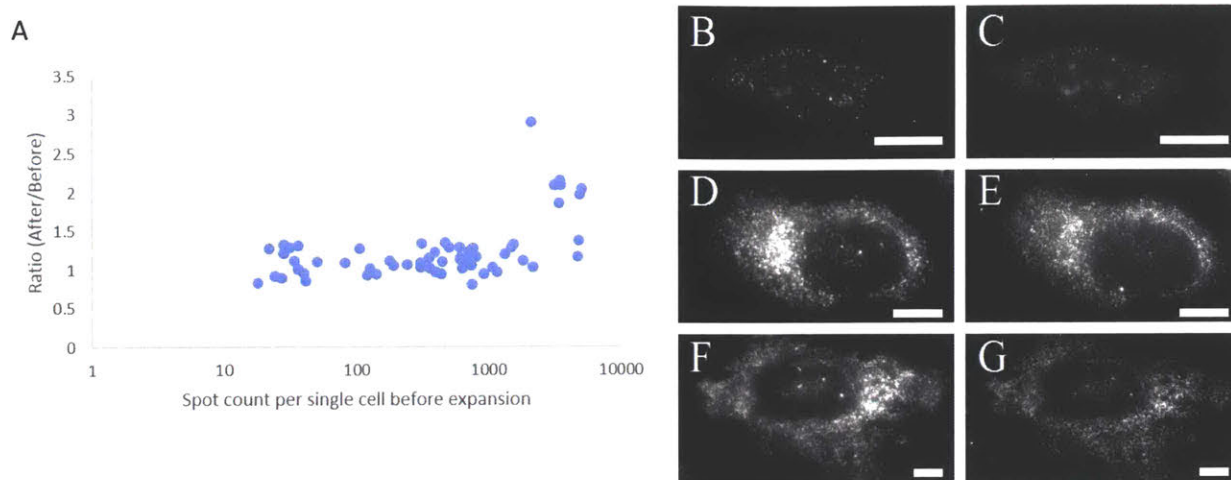
Supplementary Figure 1: Retention of RNA with LabelX.

(a) Epi-fluorescence image of single molecule FISH (smFISH) against *GAPDH* on HeLa cells expanded without LabelX treatment. (b) Epi-fluorescence image of smFISH performed against *GAPDH* on expanded HeLa cells treated with LabelX. Images are maximum intensity projections of 3-D stacks. Nuclei stained with DAPI (shown in blue). Scale bars: 20 μm (post-expanded units).



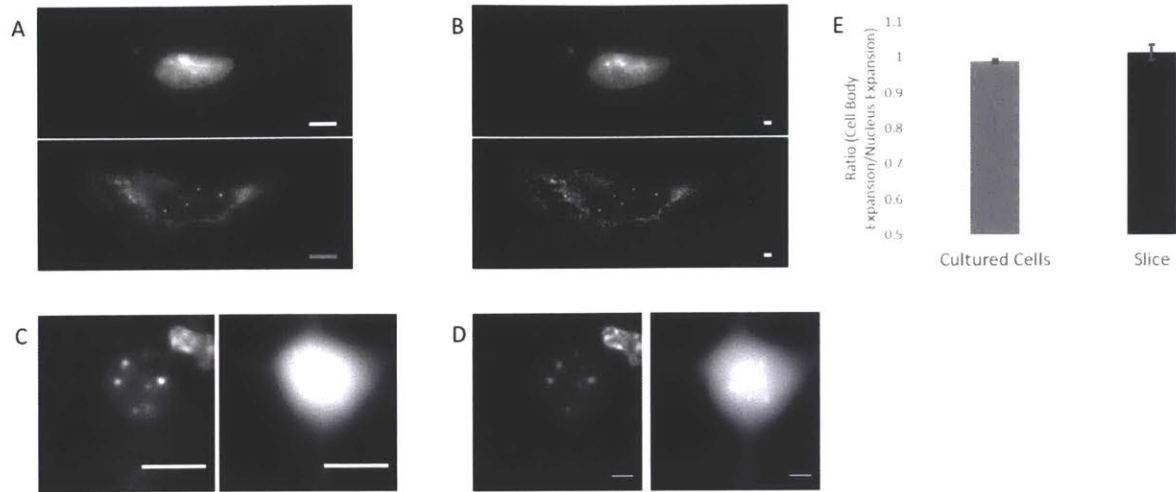
Supplementary Figure 2: Effect of LabelX on fluorescent in-situ hybridization.

To access the effect of LabelX on fluorescent *in situ* hybridization, fixed HeLa cells were stained with smFISH probe-sets, followed by DNase I treatment to remove the staining. The cells were then treated with LabelX and stained again with the same smFISH probe-sets. **(a)** *UBC* staining before LabelX treatment and **(b)** *UBC* staining after probe removal and LabelX treatment. **(c)** *EEF2* staining before LabelX treatment. **(d)** *EEF2* staining after probe removal and LabelX treatment. **(e)** Comparison of smFISH spots counted for individual cells before LabelX, and after probe removal and application of LabelX. The number of RNA molecules detected in a given cell was quantified using an automated spot counting algorithm ($n=7$ cells for each bar). Plotted are mean \pm standard error; no significant difference in spot counts before vs after LabelX ($p > 0.5$ for before vs. after for *UBC*, $p > 0.5$ for before vs. after for *EEF2*; t-test, unpaired, two-tailed). Images in **a-d** are maximum intensity projections of 3-D stacks; scale bars: 10 μm (pre-expanded units).



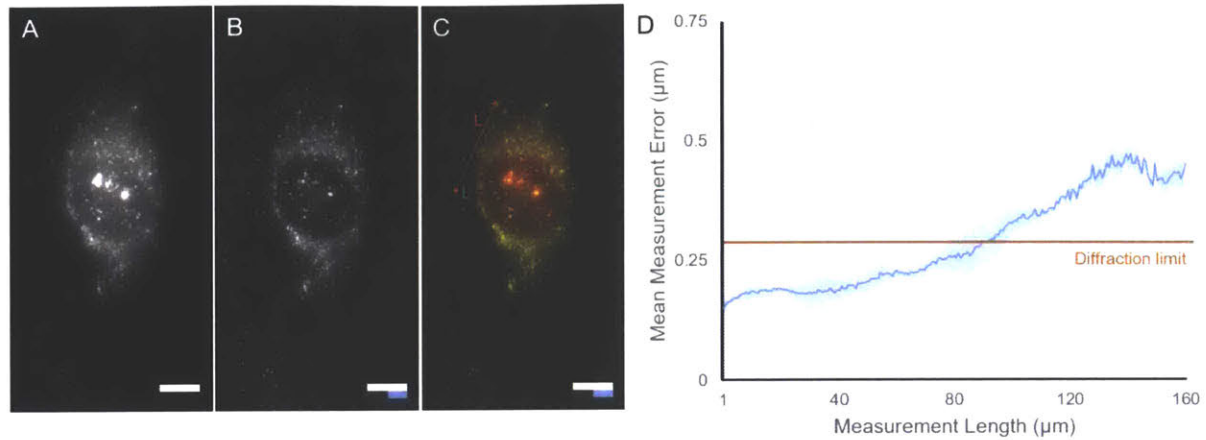
Supplementary Figure 3: High efficiency covalent anchoring of RNA to the ExM polymer gel.

Different RNA species spanning 3 orders of magnitude in abundance were detected via single molecule RNA fluorescent *in situ* hybridization (FISH) in HeLa cells before and after ExM with LabelX treatment (shown in **Fig. 1e**). **(a)** Ratio of FISH spots detected after expansion to spots detected before expansion for single cells. Representative before vs. after ExFISH images shown: **(b,c)** *TFRC*; **(d,e)** *GAPDH*; **(f,g)** *ACTB*. Scale bars, 10 μm (pre-expanded units) in **b, d, f**; **c, e, g**, expanded physical size 21 μm (imaged in PBS).



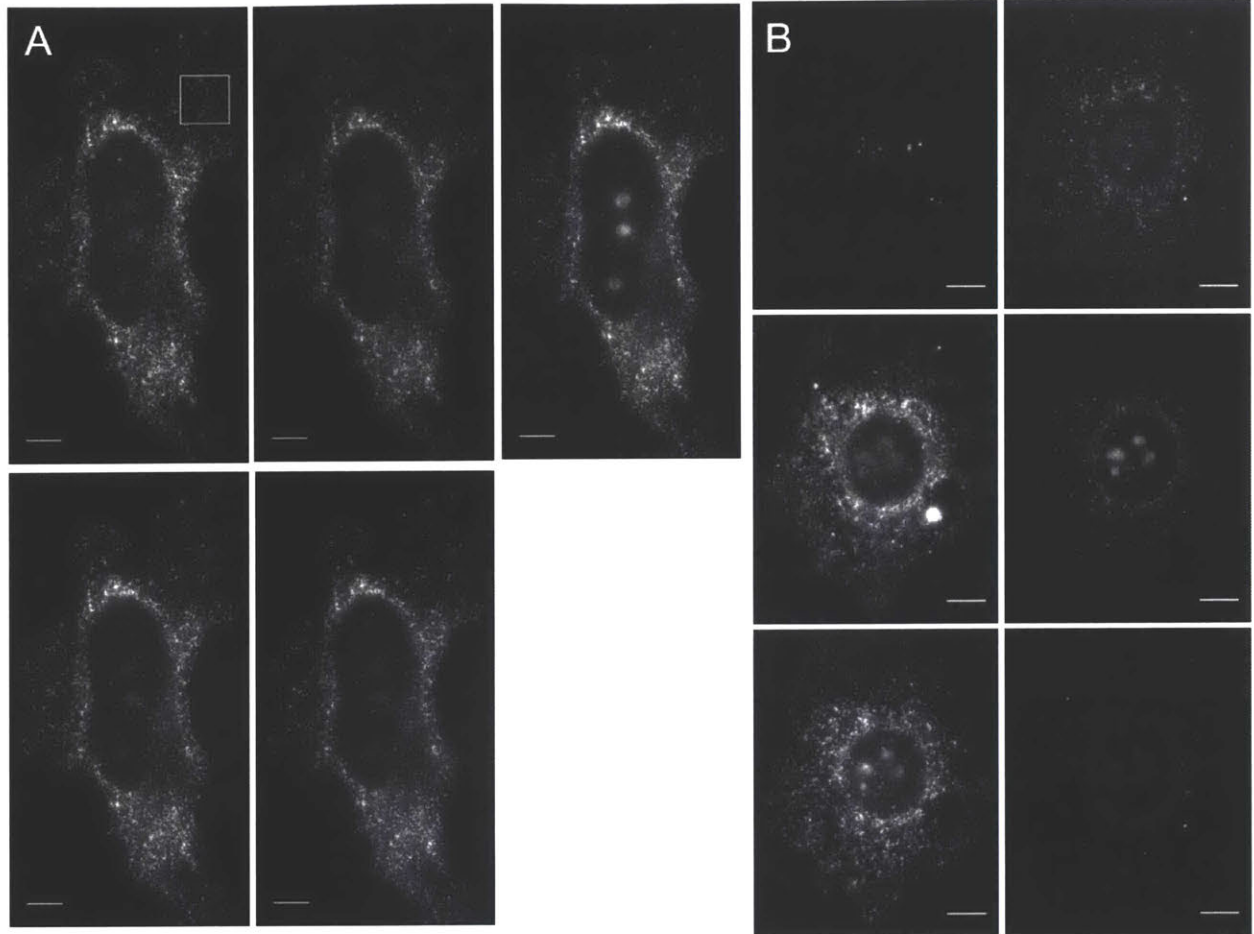
Supplementary Figure 3: LabelX does not impede nuclear expansion.

(a) Pre-expansion widefield image of a cultured HeLa cell stained with DAPI to visualize the nucleus (top panel) and smFISH probes against *ACTB* (bottom panel). (b) Post-expansion widefield image of the same cell as in (a). (c) Pre-expansion widefield image of LabelX treated Thy1-YFP brain slice (left panel, YFP protein) stained with DAPI (right panel) (MIP, 4 μm z-depth). (d) Post-expansion image of the same region as in (c) (MIP, 12 μm). (e) Ratio of the expansion factor of cell bodies for individual cells to the expansion factor of their respective nuclei. smFISH stain is used to outline the boundaries of the cell bodies of cultured cells while the endogenous YFP protein is used to demarcate the cell bodies of neurons in Thy1-YFP brain slices. Plotted are mean ± standard error. The ratio for both cultured cells and brain slices did not significantly deviate from one ($p > 0.05$ for both, 1-sample t-test; $n = 6$, cultured HeLa cells; $n = 7$, cells in 1 brain slice). Scale bars, 10 μm.



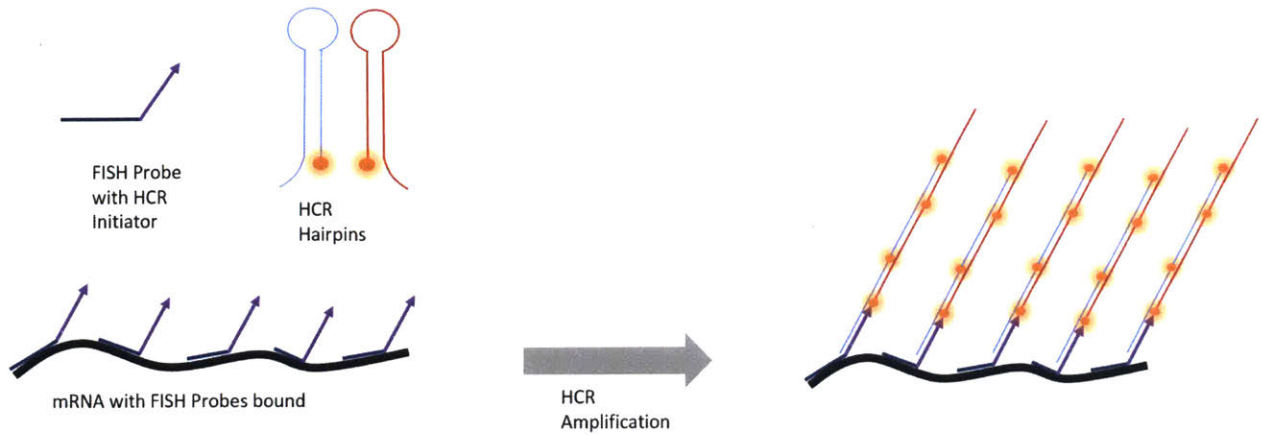
Supplementary Figure 4: Isotropy of ExFISH.

(a) Representative FISH image of *TOP2A* in a single HeLa cell before expansion (MIP of cell thickness). (b) ExFISH image of cell in (a) taken with the same optical parameters. (c) Merged image of (a) and (b) (red and green for before and after expansion respectively); distance measurements between pairs of mRNA spots before (L , red line) and after (L' , green line; note that these lines overlap nearly completely) expansion were used to quantify expansion isotropy. (d) Mean of the absolute value of the measurement error (i.e., $|L-L'|$) plotted against measurement length (L) for all pairs of mRNA spots (mean \pm standard deviation, $N = 4$ samples, 6.8×10^5 measurements). Scale bars: white, $10 \mu\text{m}$ pre-expansion units; blue, white scale bar divided by expansion factor. Orange line indicates diffraction limit of the microscope used (see Methods for details).



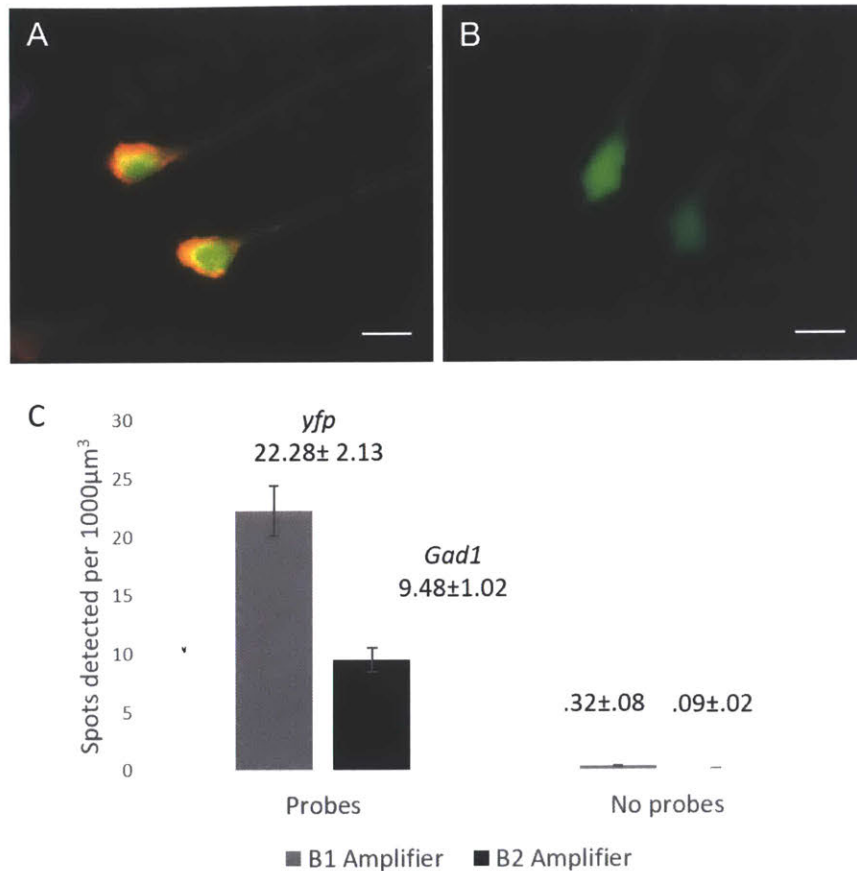
Supplementary Figure 5: Serially hybridized and multiplexed ExFISH.

(a) Five consecutive widefield fluorescence images (top to bottom, then left to right) of *GAPDH*, applied to the cell of Fig. 2a. (b) Widefield fluorescence images showing ExFISH with serially delivered probes against six RNA targets (right to left, then top to bottom: *NEAT1*, *EEF2*, *ACTB*, *UBC*, *GAPDH*, and *USF2*) in a cultured HeLa cell (raw images of composite shown in Fig. 2e). Scale bars: 20 μm in expanded units.



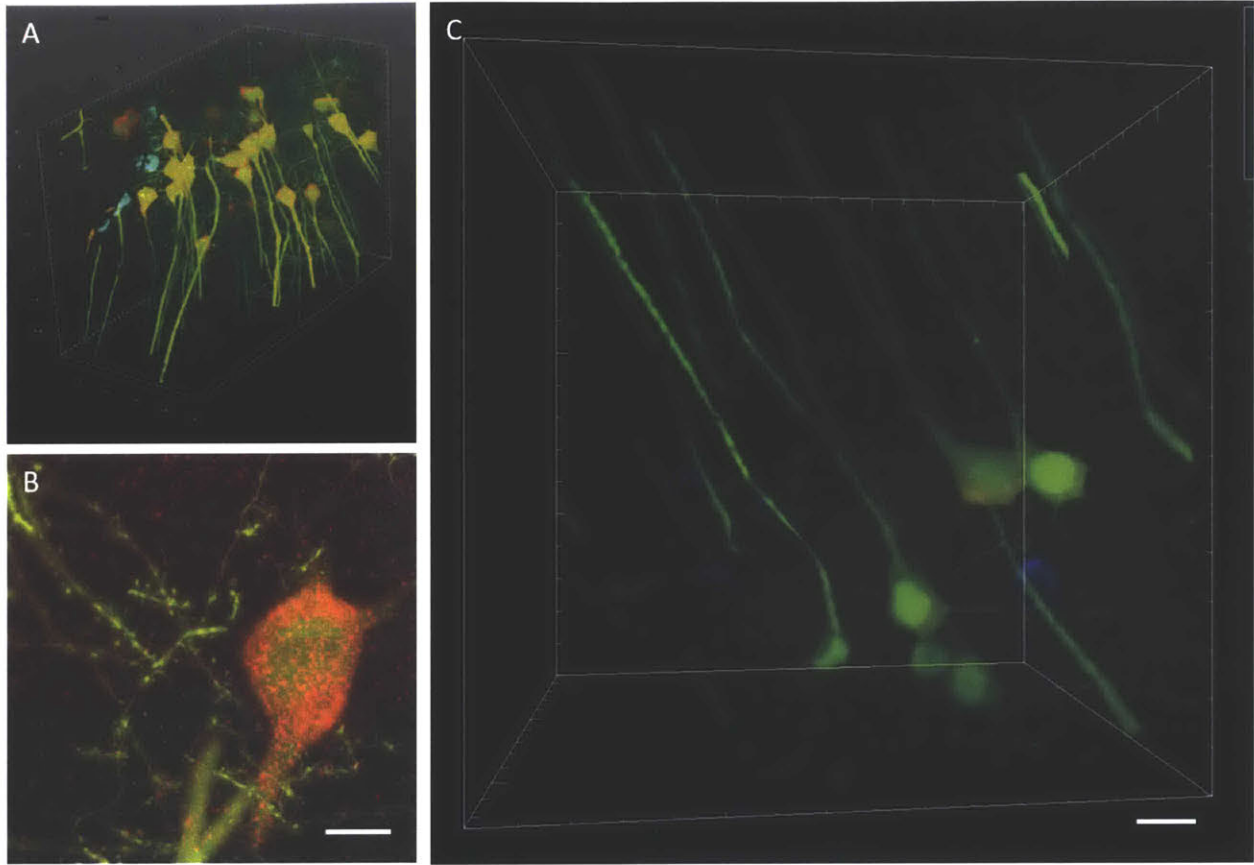
Supplementary Figure 6: Schematic for HCR-mediated signal amplification.

FISH probes bearing HCR initiators are hybridized to a target mRNA. During amplification, metastable DNA hairpins bearing fluorophores assemble into polymer chains onto the initiators, thus amplifying signal downstream of the FISH probe hybridization event.



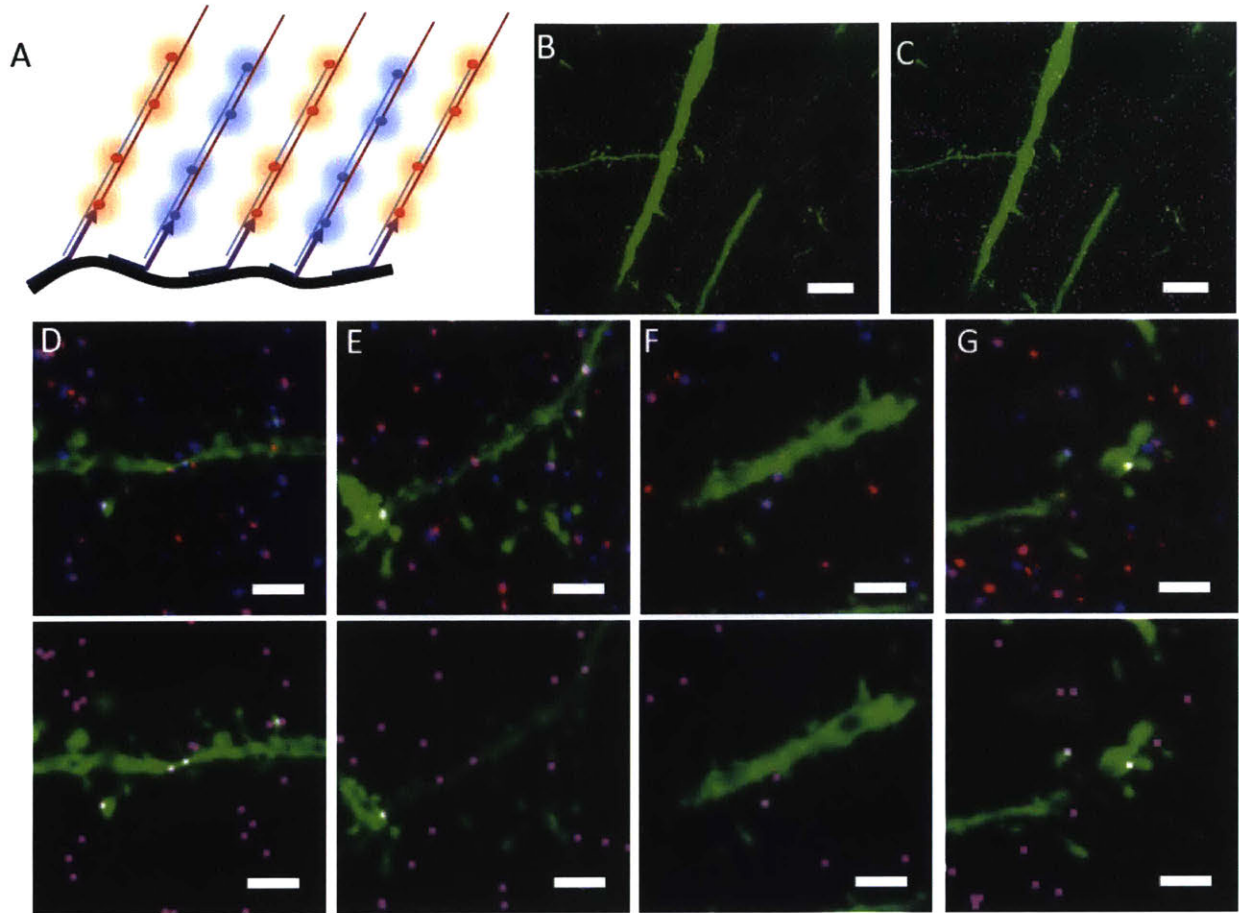
Supplementary Figure 7: HCR Amplification False Positives.

(a) Widefield image of a LabelX treated Thy1-YFP brain slice (YFP protein, green) stained with probes against *YFP* (red) and *Gad1* (magenta) followed by HCR amplification. Probes against *YFP* transcripts were amplified with the B1 amplifier set (see Methods) while probes against *Gad1* transcripts were amplified with the B2 amplifier set (MIP, 59 μm). (b) Widefield image of LabelX treated Thy1-YFP brain slice (YFP protein, green) treated with the same HCR amplifiers as in (a) (namely B1 (red) and B2 (magenta)) without the addition of probes (MIP, 50 μm). (c) HCR spots detected per volume of expanded sample. Analysis was performed on samples which were either treated or not treated with FISH probes followed by HCR amplification. An automated spot counting algorithm (as used in Fig. 1) was used to count HCR spots. The endogenous YFP protein was used to delineate regions used for the analysis. Plotted are mean ± standard error. HCR spot counts are significantly different in the presence of probes than without probes ($p < 0.05$ for both B1 and B2 amplifier sets, Welch's t-test; $n=4$ fields of view each). Scale bars: 50 μm.



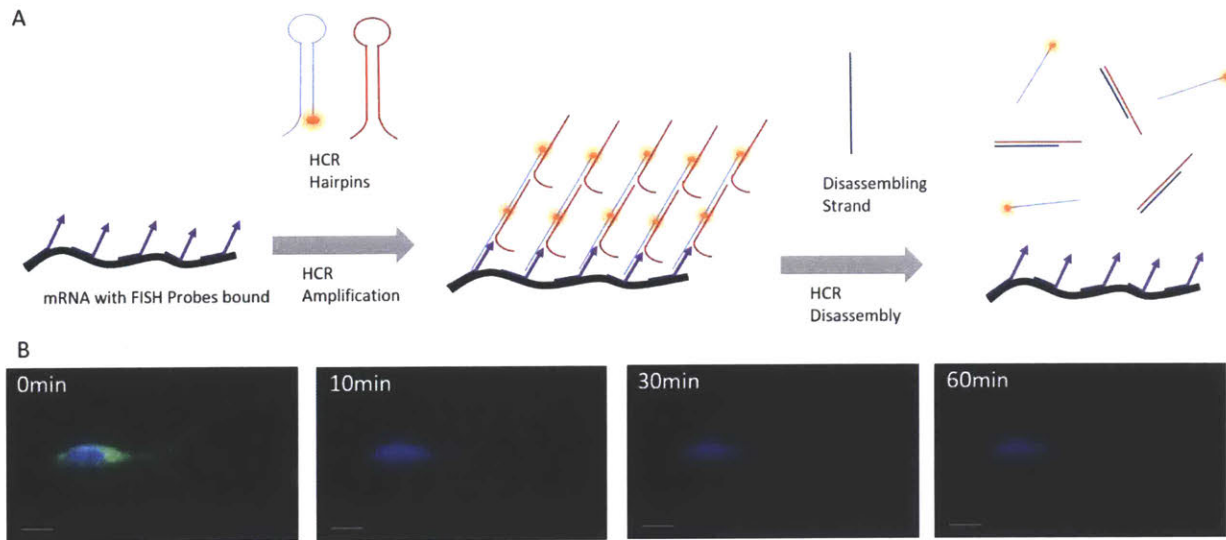
Supplementary Figure 8: Lightsheet microscopy of ExFISH.

(a) Volume rendering of Thy1-YFP (green) brain tissue acquired by lightsheet microscopy with HCR-ExFISH targeting YFP (red) and Gad1 (blue) mRNA. (b) A maximum intensity projection ($\sim 8 \mu\text{m}$ in Z) of a small subsection of the volume, showing the high resolution of imaging and single molecule localization of imaging expanded specimens with lightsheet imaging (scale bar: $10 \mu\text{m}$, in pre-expansion units, expansion factor, $3\times$). (c) Zoom in of the volume rendering in (a) (scale bar: $20 \mu\text{m}$, in pre-expansion units, $3\times$).



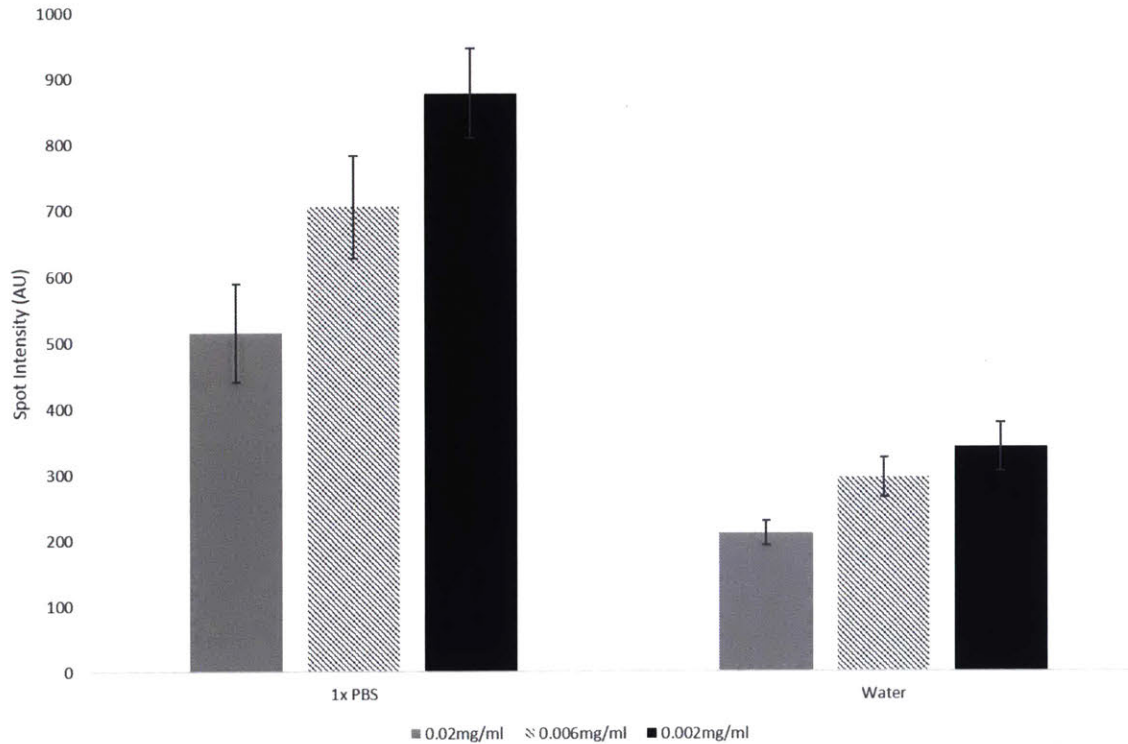
Supplementary Figure 9: Two-color co-localization of FISH probes with HCR amplification in expanded Thy1-YFP brain slices.

(a) Schematic showing two color amplification of the same target. A transcript of interest is targeted by probes against alternating parts of the sequence, and bearing two different HCR initiators, allowing for amplification in two colors. (b) Confocal image showing FISH staining with HCR amplification against the *Camk2a* transcript in two colors (red and blue; YFP fluorescence shown in green). (c) The result of an automated two-color spot co-localization analysis performed on the data set shown in (b). Each purple spot represents a positive co-localization identified by the algorithm and overlaid on the confocal image of YFP. Zoom in of dendrites showing two color FISH staining with HCR amplification against *Camk2a* (d,e) and *Dlg4* (f,g) transcripts. Top row shows the raw two color staining data corresponding to the bottom row showing co-localized spots identified by the automated algorithm (replicated from **Fig. 3j-k** for convenience). Scale bars: (b,c) 10 μm (3 \times); (d-g) 2 μm (3 \times). (b-g) are MIP of $\sim 1.6 \mu\text{m}$ thickness in unexpanded coordinates.



Supplementary Figure 10: HCR reversal via toe-hold mediated strand displacement.

(a) Schematic for HCR amplification and reversal. HCR amplification is initiated with custom-made HCR hairpins bearing toe-holds for toe-hold mediated strand displacement. After amplification, the addition of a disassembling strand initiates the disassembly of the HCR polymers via strand displacement. (b) ExFISH-treated Thy1-YFP brain slice (YFP in blue) is shown stained with YFP FISH probes bearing HCR initiators and amplified with custom made HCR hairpins bearing toe-holds for strand displacement (green dots). The different panels show the state of HCR reversal at different times after the addition of strands to initiate the disassembly of the HCR polymers. Scale bars: 20 μm (in post-expansion units).



Supplementary Figure 11: Dependence of RNA FISH spot intensity on degree of expansion and concentration of LabelX.

HeLa cells, treated with LabelX diluted to different final concentrations of Label-IT Amine concentration, were expanded and stained with a probe-set against *GAPDH*. After staining, the gelled samples were expanded in 1× PBS (~2× expansion ratio) and water (~4× expansion ratio) and the spot intensity for the different samples was quantified. Plotted are mean \pm standard error; $N = 6$ cells.

Methods

Cell Culture and Fixation:

HeLa (ATCC CCL-2) cells and HEK293-FT cells (Invitrogen) were cultured on Nunc Lab-Tek II Chambered Coverglass (Thermo Scientific) in D10 medium (Cellgro) supplemented with 10% FBS (Invitrogen), 1% penicillin/streptomycin (Cellgro), and 1% sodium pyruvate (BioWhittaker). Cells were authenticated by the manufacturer and tested for mycoplasma contamination to their standard levels of stringency, and were here used because they are common cell lines for testing new tools. Cultured cells were washed once with DPBS (Cellgro), fixed with 10% formalin for 10 mins, and washed twice with 1× PBS. Fixed cells were then stored in 70% Ethanol at 4°C until use.

Preparation of LabelX:

Acryloyl-X, SE (6-((acryloyl)amino)hexanoic acid, succinimidyl ester, here abbreviated AcX; Thermo-Fisher) was resuspended in anhydrous DMSO at a concentration of 10 mg/mL, aliquoted and stored frozen in a desiccated environment. Label-IT® Amine Modifying Reagent (Mirus Bio, LLC) was resuspended in the provided Mirus Reconstitution Solution at 1mg/ml and stored frozen in a desiccated environment. To prepare LabelX, 10 µL of AcX (10 mg/mL) was reacted with 100 µL of Label-IT® Amine Modifying Reagent (1 mg/mL) overnight at room temperature with shaking. LabelX was subsequently stored frozen (-20 °C) in a desiccated environment until use.

Mouse perfusion:

All methods for animal care and use were approved by the Massachusetts Institute of Technology Committee on Animal Care and were in accordance with the National Institutes of Health Guide for the Care and Use of Laboratory Animals. All solutions below were made up in 1× phosphate buffered saline (PBS) prepared from nuclease free reagents. Mice were anesthetized with isoflurane and perfused transcardially with ice cold 4% paraformaldehyde. Brains were dissected out, left in 4% paraformaldehyde at 4°C for one day, before moving to PBS containing 100 mM glycine. Slices (50 µm and 200 µm) were sliced on a vibratome (Leica VT1000S) and stored at 4 °C in PBS until use. The mouse used in **Fig. 3** and related analyses was a Thy1-YFP (Tg(Thy1-YFP)16Jrs) male mouse in the age range 6-8 weeks. No sample size estimate was performed, since the goal was to demonstrate a technology. No exclusion, randomization or blinding of samples was performed.

LabelX Treatment of Cultured Cells and Brain Slices:

Fixed cells were washed twice with 1× PBS, once with 20 mM MOPS pH 7.7, and incubated with LabelX diluted to a desired final concentration in MOPS buffer (20 mM MOPS pH 7.7) at 37 °C overnight followed by two washes with 1× PBS. For cells, ranges of LabelX were used that resulted in a Label-IT ® Amine concentration of 0.006-0.02 mg/mL; higher concentrations resulted in somewhat dimmer smFISH staining (**Supplementary Fig. 12**), but otherwise no difference in staining quality was observed with Label-IT ® Amine concentrations in this range. For **Fig. 1e**, **Supplementary Fig 1**, **Supplementary Fig 2**, and **Supplementary Fig 3** fixed cells were incubated with LabelX diluted to a final Label-IT ® Amine concentration of 0.02 mg/mL. For all other experiments in cells, fixed cells were treated with LabelX diluted to a final Label-IT ® Amine concentration of 0.006 mg/mL.

Brain slices, as prepared above, were incubated with 20mM MOPS pH 7.7 for 30 mins and subsequently incubated with LabelX diluted to a final Label-IT ® Amine concentration of 0.1 mg/mL (due to their increased thickness and increased fragmentation from formaldehyde post-fixation) in MOPS buffer (20 mM MOPS pH 7.7) at 37°C overnight. For YFP retention, slices were treated with 0.05 mg/mL AcX in PBS for >6 hours @ RT.

smFISH in Fixed Cultured Cells Before Expansion:

Fixed cells were briefly washed once with wash buffer (10% formamide, 2× SSC) and hybridized with RNA FISH probes in hybridization buffer (10% formamide, 10% dextran sulfate, 2× SSC) overnight at 37 °C. Following hybridization, samples were washed twice with wash buffer, 30mins per wash, and washed once with 1× PBS. Imaging was performed in 1× PBS.

smFISH probe sets targeting the human transcripts for *TFRC*, *ACTB*, *GAPDH*, *XIST*, and 5' portion of *NEAT1* were ordered from Stellaris with Quasar 570 dye. Probe sets against *UBC*, *EEF2*, *USF2*, *TOP2A* and full length *NEAT1* were synthesized, conjugated to fluorophores, and subsequently purified by HPLC as described previously¹²¹. Oligonucleotide sequences for probe sets and accession numbers can be found in **Supplementary Table 4**.

Gelation, Digestion and Expansion:

Monomer solution (1× PBS, 2 M NaCl, 8.625% (w/w) sodium acrylate, 2.5% (w/w) acrylamide, 0.15% (w/w) N,N'-methylenebisacrylamide) was mixed, frozen in aliquots, and thawed before use. Monomer solution was cooled to 4°C before use. For gelling cultured cells treated with LabelX, a concentrated stock of VA-044 (25% w/w, chosen instead of the Ammonium persulfate (APS)/Tetramethylethylenediamine (TEMED) of the original ExM protocol⁴¹ because APS/TEMED resulted in autofluorescence that was small in magnitude but appreciable in the context of smFISH) was added to the monomer solution to a final concentration of 0.5% (w/w) and degassed in 200 µl aliquots for 15 mins. Cells were briefly incubated with the monomer solution plus VA-044 and transferred to a humidified chamber. Subsequently, the humidified chamber was purged with nitrogen gas. To initiate gelation, the humidified chamber was transferred to a 60 °C incubator for two hours. For gelling brain slices treated with LabelX, gelation

was performed as in the original ExM protocol (since, with HCR amplification, the slight autofluorescence of APS/TEMED was negligible). Gelled cultured cells and brain slices were digested with Proteinase K (New England Biolabs) diluted 1:100 to 8 units/mL in digestion buffer (50 mM Tris (pH 8), 1 mM EDTA, 0.5% Triton X-100, 500 mM NaCl) and digestion was carried out overnight at 37 °C. The gels expand slightly in the high osmolarity digestion buffer (~1.5×). After digestion, gels were stored in 1× PBS until use and expansion was carried out as previously described.

smFISH Staining After Expansion:

Expanded gels were incubated with wash buffer (10% formamide, 2× SSC) for 30 mins at room temperature and hybridized with RNA FISH probes in hybridization buffer (10% formamide, 10% dextran sulfate, 2× SSC) overnight at 37 °C. Following hybridization, samples were washed twice with wash buffer, 30 minutes per wash, and washed once with 1× PBS for another 30 mins. Imaging was performed in 1× PBS.

Image Processing and Analysis of smFISH performed on Cultured Cells:

Widefield images of smFISH staining performed before or after expansion were first processed using a rolling-ball background subtraction algorithm (FIJI)¹²² with a 200 pixel radius. Subsequently, maximum intensity Z-projections of these images were generated. Spots were then localized and counted using a code developed by the Raj lab and available online (<http://rajlab.seas.upenn.edu/StarSearch/launch.html>). This image analysis was performed for **Fig. 1c-e, Fig.2a-c, Supplementary Fig. 2-4, 6, 8.**

Analysis of Expansion Isotropy:

smFISH images before and after expansion of *TOP2A* was rigidly aligned via two control points using the FIJI plugin Turboreg¹²³. Spots were localized and counted via a custom spot counting Matlab code developed by the Raj lab (complete source code and instructions can be found at <https://bitbucket.org/arjunrajlaboratory/rajlabimagetools/wiki/Home>). Length measurements were performed among all pairs of points before expansion and the corresponding pairs of points after expansion via a custom Matlab script. Measurement error was defined as the absolute difference between the before and after expansion length measurements (**Supplementary Fig. 5c**).

Re-embedding of Expanded Gels in Acrylamide Matrix:

For serial staining in cells, expanded gels were re-embedded in acrylamide to stabilize the gels in the expanded state. Briefly: gels were expanded in water and cut manually to ~1 mm thickness

with a stainless steel blade. Cut gels were incubated in 3% acrylamide, 0.15% N,N'-Methylenebisacrylamide with 0.05% APS, 0.05% TEMED and 5 mM Tris pH 10.5 for 20 minutes on a shaker. There is a ~30% reduction in gel size during this step. Excess solution is removed from the gels and the gels are dried with light wicking from a laboratory wipe. Gels are placed on top of a bind-silane treated (see below) coverslip or glass bottom plate with a coverslip placed on top of the gels before moving into a container and purged with nitrogen. The container is moved to a 37 °C incubator for gelation for 1.5 hours.

Staining of Re-embedded Gels:

Re-embedded staining of gels were performed with exact conditions as described above for expanded gels, except post-hybridization washes were changed to twice with wash buffer (10% formamide), 60 minutes per wash.

Probes were removed for multiple rounds of hybridization via treatment with DNase I or 100% formamide. For DNase I, samples were treated with DNase I at 0.5 U/□L for 6 hours at RT. For formamide stripping, samples were treated with 100% formamide at 6 hours at 37C.

Bind-silane Treatment of Coverslips:

Coverslips and glass bottom 24 well plates were treated with Bind-Silane, a silanization reagent which incorporates acryloyl groups onto the surface of glass to perform in free radical polymerization. Briefly, 5 □L of Bind-Silane reagent was diluted into 8 mL of ethanol, 1.8 mL of ddH₂O and 200 □L of acetic acid. Coverslips and glass bottom 24 well plates were washed with ddH₂O followed by 100% ethanol, followed by the diluted Bind-Silane reagent. After a brief wash with the diluted Bind-Silane reagent, the cover-slip was dried, then washed with 100% ethanol, and then dried again. Coverslips were prepared immediately before use.

Probe Design for HCR-FISH:

Probe sequences and accession numbers for mRNA targets can be found in **Supplementary Table 4**. Probes were designed for HCR-FISH by tiling the CDS of mRNA targets with 22-mer oligos spaced by 3-7 bases. HCR initiators were appended to tiled sequences via a 2 base spacer (AA). For 2 color probe-sets, even and odd tiled probes were assigned different HCR-initiators to allow for amplification in different color channel.

RNA FISH with Hybridization Chain Reaction (HCR) Amplification:

Gelled samples were incubated with wash buffer (20% formamide, 2× SSC) for 30mins at room temperature and hybridized with HCR initiator tagged FISH probes in hybridization buffer (20% formamide, 10% dextran sulfate, 2× SSC) overnight at 37 °C. Following hybridization, samples were washed twice with wash buffer, 30mins per wash, and incubated with 1× PBS for 2hrs at 37°C. Subsequently, samples were incubated with 1× PBS for at least 6hrs at room temperature. Before HCR amplification, hybridized samples were pre-incubated with

amplification buffer (10% dextran sulfate, 5× SSC, 0.1% Tween 20) for 30 mins. To initiate amplification, HCR hairpin stocks (Alexa 456 and Alexa 647 fluorophores) at 3 μ M were snap-cooled by heating to 95°C for 90 seconds, and leaving to cool at room temperature for 30 mins. Gelled samples were then incubated with HCR hairpins diluted to 60 nM in amplification buffer for 3hrs at room temperature. After amplification, gels were washed with 5× SSCT (5× SSC, 0.1% Tween 20) twice with one hour per wash.

Imaging of Cultured Cells using ExFISH:

Both cultured cells as well as LabelX treated and expanded cultured cells were imaged on a Nikon Ti-E epifluorescence microscope with a SPECTRA X light engine (Lumencor), and a 5.5 Zyla sCMOS camera (Andor), controlled by NIS-Elements AR software. For **Fig. 1c, 1d**, and **Supplementary Fig 3-5** a 40× 1.15 NA water immersion objective was used. For all other experiments with cultured cells, a 60× 1.4 NA oil immersion objective was used.

For imaging smFISH probes labeled with fluorophores, the following filter cubes (Semrock, Rochester, NY) were used: Alexa 488, GFP-1828A-NTE-ZERO; Quasar 570, LF561-B-000; Alexa 594, FITC/TXRED-2X-B-NTE; Atto 647N, Cy5-4040C-000.

Imaging of Expanded Brain Slices:

For epifluorescence imaging of brain sections before and after expansion (**Fig. 3a-e**) and to quantify expansion factors of tissue slices specimens were imaged on a Nikon Ti-E epifluorescence microscope with a 4× 0.2 NA air objective, a SPECTRA X light engine (Lumencor), and a 5.5 Zyla sCMOS camera (Andor), controlled by NIS-Elements AR software.

Post-expansion confocal imaging of expanded brain tissue was performed on an Andor spinning disk (CSU-X1 Yokogawa) confocal system with a 40× 1.15 NA water objective (**Fig. 3f-k, Supplementary Fig. 10**) on a Nikon TI-E microscope body. GFP was excited with a 488 nm laser, with 525/40 emission filter. Alexa 546 HCR amplicons were excited with a 561 nm laser with 607/36 emission filter. Alexa 647 amplicons were excited with a 640 nm laser with 685/40 emission filter.

Gels were expanded in with 3 washes, 15 minutes each of 0.05× SSC. The expansion factor can be controlled with the salt concentration, we found that 0.05× SSC gives 3× expansion, while still giving enough salt for hybridization stability. To stabilize the gels against drift during imaging following expansion, gels were placed in glass bottom 6 well plates with all excess liquid removed. If needed, liquid low melt agarose (2% w/w) was pipetted around the gel and allowed to solidify, to encase the gels before imaging.

Lightsheet imaging was performed on a Zeiss Z.1 lightsheet microscope. Briefly, the sample was fixed on a custom-made plastic holder using super glue and mounted on the freely rotating stage of the Z.1 lightsheet. Lightsheets were generated by two illumination objectives (5×, NA 0.1), and the fluorescence signal detected by a 20× water immersion objective (NA 1.0). Both lightsheets were used for data collection. The image volume dimensions of a single tile were

1400×1400×1057 pixels, with a voxel size of 227 nm laterally and 469 nm axially. The laserlines used for excitation were 488 nm, 561 nm and 638 nm. The individual laser transmissions were set to 5%, with the maximum output of 50 mW (488 nm and 561 nm) and 75 mW (638 nm). Optical filters used to separate and clean the fluorescence response included a Chroma T560lpxr as a dichroic, and a Chroma 59001m for GFP and 59007m for Alexa 546 and Alexa 647. Two PCO.Edge 5.5m sCMOS cameras were used to capture two fluorescence channels simultaneously. Tiled datasets were taken with the Zeiss ZEN Software, and subsequently merged and processed with FIJI, Arivis Vision4D and Bitplane Imaris.

Two Color Analysis in Slices:

A sliding window averaging (or minimization) scheme in Z (3 optical sections) was used to suppress movement artifacts before spot detection processing. RNA puncta were detected via a custom 3D spot counting Matlab code developed by the Raj lab; complete source code and instructions can be found at <https://bitbucket.org/arjunrajlaboratory/rajlabimagnetools/wiki/Home>.

Spot centroids were extracted from both color channels, and spots were determined to be co-localized if their centroids were within a 3 pixel radius in the x,y dimensions and a 2 pixel radius in the z dimension.

HCR Reversal via Toe-Hold Mediated Strand Displacement:

HCR amplification commences upon the addition of two HCR metastable amplifier hairpins. We designed a pair of HCR amplifiers, B2H1T and B2H2 (see below for sequence), where B2H1T bears a 6bp toe-hold for strand displacement. To initiate HCR amplification, aliquots of these amplifiers at 3 μ M were snap-cooled by heating to 95 °C for 90 seconds, and leaving to cool at room temperature for 30 mins. Gelled samples were then incubated with HCR hairpins diluted to 60nM in amplification buffer for 3hrs at room temperature. After amplification, gels were washed with 5× SSCT (5× SSC, 0.1% Tween 20) twice with one hour per wash. Subsequently, HCR reversal was initiated by the addition of a displacement strand (see below for sequence) at 200 nM in 5× SSCT.

B2H1T:

*ggCggTTTACTggATgATTgATgAggATTTACgAggAgCTCAgTCCATCCTCgTAAATCCTCA
TCAATCATCAAATAG*

B2H2:

/5'-Alexa546-C12/

*CCTCgTAAATCCTCATCAATCATCCAgTAAACCgCCgATgATTgATgAggATTTACgAggA
TggACTgAgCT*

Displacement Strand:

CTATTGATGATTGATGAGGATTTAcGAGGATGGAcTGAGcT

References

1. Heintzmann R, Ficz G. Breaking the resolution limit in light microscopy. *Methods Cell Biol.* 2013;114:525-544. doi:10.1016/B978-0-12-407761-4.00022-1.
2. Ribault C, Sekimoto K, Triller A. From the stochasticity of molecular processes to the variability of synaptic transmission. *Nat Rev Neurosci.* 2011;12(7):375-387. doi:10.1038/nrn3025.
3. Südhof TC. THE SYNAPTIC VESICLE CYCLE. *Annu Rev Neurosci.* 2004;27(1):509-547. doi:10.1146/annurev.neuro.26.041002.131412.
4. Shapira M, Zhai RG, Dresbach T, et al. Unitary assembly of presynaptic active zones from Piccolo-Bassoon transport vesicles. *Neuron.* 2003;38(2):237-252. doi:10.1016/S0896-6273(03)00207-1.
5. Betzig E, Patterson GH, Sougrat R, et al. Imaging intracellular fluorescent proteins at nanometer resolution. *Science.* 2006;313(2006):1642-1645. doi:10.1126/science.1127344.
6. Rust MJ, Bates M, Zhuang XW. Sub-diffraction-limit imaging by stochastic optical reconstruction microscopy (STORM). *Nat Methods.* 2006;3(10):793-795. doi:10.1038/Nmeth929.
7. Xu K, Babcock HP, Zhuang X. Dual-objective STORM reveals three-dimensional filament organization in the actin cytoskeleton. *Nat Methods.* 2012;9(2):185-188. doi:10.1038/nmeth.1841.
8. Vaughan JC, Jia S, Zhuang X. Ultrabright photoactivatable fluorophores created by reductive caging. *Nat Methods.* 2012;9(12):1181-1184. doi:10.1038/nmeth.2214.
9. Schermelleh L, Heintzmann R, Leonhardt H. A guide to super-resolution fluorescence microscopy. *J Cell Biol.* 2010;190:165-175. doi:10.1083/jcb.201002018.
10. HELL SW, WICHMANN J. Breaking the Diffraction Resolution Limit By Stimulated-Emission - Stimulated-Emission-Depletion Fluorescence Microscopy. *Opt Lett.* 1994;19(11):780-782. doi:10.1364/OL.19.000780.
11. Hell SW. Far-field optical nanoscopy. In: *2010 23rd Annual Meeting of the IEEE Photonics Society, PHOTONICS 2010.* ; 2010:3-4. doi:10.1109/PHOTONICS.2010.5698725.
12. Dyba M, Jakobs S, Hell SW. Immunofluorescence stimulated emission depletion microscopy. *Nat Biotechnol.* 2003;21(11):1303-1304. doi:10.1038/nbt897.
13. Chmyrov A, Keller J, Grotjohann T, et al. Nanoscopy with more than 100,000 "doughnuts". *Nat Methods.* 2013;10:737-740. doi:10.1038/nmeth.2556.
14. Andresen M, Stiel AC, Fölling J, et al. Photoswitchable fluorescent proteins enable monochromatic multilabel imaging and dual color fluorescence nanoscopy. *Nat Biotechnol.* 2008;26(9):1035-1040. doi:10.1038/nbt.1493.
15. Grotjohann T, Testa I, Reuss M, et al. rsEGFP2 enables fast RESOLFT nanoscopy of living cells. *Elife.* 2012;2012(1). doi:10.7554/eLife.00248.
16. Tanaka T, Fillmore D, Sun ST, Nishio I, Swislow G, Shah A. Phase Transitions in Ionic

- Gels. *Phys Rev Lett*. 1980;45:1636-1639. doi:10.1103/PhysRevLett.45.1636.
17. Germroth PG, Gourdie RG, Thompson RP. Confocal microscopy of thick sections from acrylamide gel embedded embryos. *Microsc Res Tech*. 1995;30(6):513-520. doi:10.1002/jemt.1070300608.
 18. Chung K, Wallace J, Kim S-Y, et al. Structural and molecular interrogation of intact biological systems. *Nature*. 2013;497(7449):332-337. doi:10.1038/nature12107.
 19. Ohmine I. Salt effects on the phase transition of ionic gels. *J Chem Phys*. 1982;77:5725. doi:10.1063/1.443780.
 20. Buchholz FL. Preparation Methods of Superabsorbent Polyacrylates. In: *Superabsorbent Polymers*. Vol 573. ; 1994:2-27. doi:doi:10.1021/bk-1994-0573.ch002.
 21. Huang B, Jones SA, Brandenburg B, Zhuang X. Whole-cell 3D STORM reveals interactions between cellular structures with nanometer-scale resolution. *Nat Methods*. 2008;5:1047-1052. doi:10.1038/nmeth.1274.
 22. Rego EH, Shao L, Macklin JJ, et al. PNAS Plus: Nonlinear structured-illumination microscopy with a photoswitchable protein reveals cellular structures at 50-nm resolution. *Proc Natl Acad Sci*. 2012;109:E135-E143. doi:10.1073/pnas.1107547108.
 23. Bates M, Huang B, Dempsey GT, Zhuang X. Multicolor super-resolution imaging with photo-switchable fluorescent probes. *Science*. 2007;317:1749-1753. doi:10.1126/science.1146598.
 24. Olivier N, Keller D, Gönczy P, Manley S. Resolution Doubling in 3D-STORM Imaging through Improved Buffers. *PLoS One*. 2013;8. doi:10.1371/journal.pone.0069004.
 25. Cole RW, Jinadasa T, Brown CM. Measuring and interpreting point spread functions to determine confocal microscope resolution and ensure quality control. *Nat Protoc*. 2011;6(12):1929-1941. doi:10.1038/nprot.2011.407.
 26. Feng G, Mellor RH, Bernstein M, et al. Imaging neuronal subsets in transgenic mice expressing multiple spectral variants of GFP. *Neuron*. 2000;28:41-51. doi:10.1016/S0896-6273(00)00084-2.
 27. Dani A, Huang B, Bergan J, Dulac C, Zhuang X. Superresolution Imaging of Chemical Synapses in the Brain. *Neuron*. 2010;68:843-856. doi:10.1016/j.neuron.2010.11.021.
 28. Rollenhagen A, Lübke JHR. The mossy fiber bouton: the “common” or the “unique” synapse? *Front Synaptic Neurosci*. 2010;2:2. doi:10.3389/fnsyn.2010.00002.
 29. Huisken J, Swoger J, Del Bene F, Wittbrodt J, Stelzer EHK. Optical sectioning deep inside live embryos by selective plane illumination microscopy. *Science*. 2004;305:1007-1009. doi:10.1126/science.1100035.
 30. Newman GR, Jasani B, Williams ED. A simple post-embedding system for the rapid demonstration of tissue antigens under the electron microscope. *Histochem J*. 1983;15:543-555. doi:10.1007/BF01954145.
 31. Micheva KD, Smith SJ. Array Tomography: A New Tool for Imaging the Molecular Architecture and Ultrastructure of Neural Circuits. *Neuron*. 2007;55:25-36. doi:10.1016/j.neuron.2007.06.014.
 32. Ribak CE. Aspinous and sparsely-spinous stellate neurons in the visual cortex of rats

contain glutamic acid decarboxylase. *J Neurocytol.* 1978;7:461-478.
doi:10.1007/BF01173991.

33. Houser CR, Crawford GD, Salvaterra PM, Vaughn JE. Immunocytochemical localization of choline acetyltransferase in rat cerebral cortex: a study of cholinergic neurons and synapses. *J Comp Neurol.* 1985;234:17-34. doi:10.1002/cne.902340103.
34. Tighilet B, Hashikawa T, Jones EG. Cell- and lamina-specific expression and activity-dependent regulation of type II calcium/calmodulin-dependent protein kinase isoforms in monkey visual cortex. *J Neurosci.* 1998;18:2129-2146.
35. Hendry SHC, Jones EG, Emson PC, Lawson DEM, Heizmann CW, Streit P. Two classes of cortical GABA neurons defined by differential calcium binding protein immunoreactivities. *Exp Brain Res.* 1989;76:467-472. doi:10.1007/BF00247904.
36. Hozák P, Sasseville AM, Raymond Y, Cook PR. Lamin proteins form an internal nucleoskeleton as well as a peripheral lamina in human cells. *J Cell Sci.* 1995;108 (Pt 2:635-644.
37. Fritschy JM, Weinmann O, Wenzel A, Benke D. Synapse-specific localization of NMDA and GARA(A) receptor subunits revealed by antigen-retrieval immunohistochemistry. *J Comp Neurol.* 1998;390:194-210. doi:10.1002/(SICI)1096-9861(19980112)390:2<194::AID-CNE3>3.0.CO;2-X.
38. Choi HMT, Chang JY, Trinh LA, Padilla JE, Fraser SE, Pierce NA. Programmable *in situ* amplification for multiplexed imaging of mRNA expression. *Nat Biotechnol.* 2010;28:1208-1212. doi:10.1038/nbt.1692.
39. Preibisch S, Saalfeld S, Tomancak P. Globally optimal stitching of tiled 3D microscopic image acquisitions. *Bioinformatics.* 2009;25:1463-1465. doi:10.1093/bioinformatics/btp184.
40. Kroon D-J. B-spline Grid, Image and Point based Registration. Matlab Central.
41. Chen F, Tillberg PW, Boyden ES. Expansion microscopy. *Science (80-).* 2015;347(6221):543-548. doi:10.1126/science.1260088.
42. Laemmli UK. Cleavage of structural proteins during the assembly of the head of bacteriophage T4. *Nature.* 1970;227(5259):680-685. doi:10.1038/227680a0.
43. N C A Hunt B Jasani RA. High temperature antigen retrieval and loss of nuclear morphology: a comparison of microwave\rand autoclave techniques. *J Clin Pathol.* 1996;49:767-770. doi:10.1136/jcp.49.9.767.
44. Jekel PA, Weijer WJ, Beintema JJ. Use of endoproteinase Lys-C from *Lysobacter* enzymogenes in protein sequence analysis. *Anal Biochem.* 1983;134(2):347-354. doi:10.1016/0003-2697(83)90308-1.
45. Wu CC, MacCoss MJ, Howell KE, Yates JR. A method for the comprehensive proteomic analysis of membrane proteins. *Nat Biotechnol.* 2003;21(5):532-538. doi:10.1038/nbt819.
46. Sniegowski JA, Phail ME, Wachter RM. Maturation efficiency, trypsin sensitivity, and optical properties of Arg96, Glu222, and Gly67 variants of green fluorescent protein. *Biochem Biophys Res Commun.* 2005;332(3):657-663. doi:10.1016/j.bbrc.2005.04.166.
47. Bokman SH, Ward WW. Renaturation of *Aequorea* gree-fluorescent protein. *Biochem*

Biophys Res Commun. 1981;101(4):1372-1380.

48. Seneviratne U, Nott A, Bhat VB, et al. S-nitrosation of proteins relevant to Alzheimer's disease during early stages of neurodegeneration. *Proc Natl Acad Sci U S A.* March 2016;1521318113-. doi:10.1073/pnas.1521318113.
49. Rego EH, Shao L, Macklin JJ, et al. Nonlinear structured-illumination microscopy with a photoswitchable protein reveals cellular structures at 50-nm resolution. *Proc Natl Acad Sci U S A.* 2012;109(3):E135-43. doi:10.1073/pnas.1107547108.
50. Bossi M, Fölling J, Belov VN, et al. Multicolor far-field fluorescence nanoscopy through isolated detection of distinct molecular species. *Nano Lett.* 2008;8(8):2463-2468. doi:10.1021/nl801471d.
51. Cai D, Cohen KB, Luo T, Lichtman JW, Sanes JR. Improved tools for the Brainbow toolbox. *Nat Methods.* 2013;10(6):540-547. doi:10.1038/nmeth.2450.
52. Livet J, Weissman TA, Kang H, et al. Transgenic strategies for combinatorial expression of fluorescent proteins in the nervous system. *Nature.* 2007;450(7166):56-62. doi:10.1038/nature06293.
53. Schnell U, Dijk F, Sjollem KA, Giepmans BNG. Immunolabeling artifacts and the need for live-cell imaging. *Nat Methods.* 2012;9:152-158. doi:10.1038/nmeth.1855.
54. Hackstadt T. Steric hindrance of antibody binding to surface proteins of *Coxiella burnetti* by phase I lipopolysaccharide. *Infect Immun.* 1988;56(4):802-807.
55. Jiménez N, Post JA. A Novel Approach for Intracellular 3D Immuno-Labeling for Electron Tomography. *Traffic.* 2012;13(7):926-933. doi:10.1111/j.1600-0854.2012.01363.x.
56. Randall KJ, Pearse G. A dual-label technique for the immunohistochemical demonstration of T-lymphocyte subsets in formalin-fixed, paraffin-embedded rat lymphoid tissue. *Toxicol Pathol.* 2008;36(6):795-804. doi:10.1177/0192623308322311.
57. Kakimoto K, Takekoshi S, Miyajima K, Osamura RY. Hypothesis for the mechanism for heat-induced antigen retrieval occurring on fresh frozen sections without formalin-fixation in immunohistochemistry. *J Mol Histol.* 2008;39(4):389-399. doi:10.1007/s10735-008-9177-y.
58. Ai H, Shaner NC, Cheng Z, Tsien RY, Campbell RE. Exploration of new chromophore structures leads to the identification of improved blue fluorescent proteins. *Biochemistry.* 2007;46(20):5904-5910. doi:10.1021/bi700199g.
59. Subach OM, Cranfill PJ, Davidson MW, Verkhusha V V. An Enhanced Monomeric Blue Fluorescent Protein with the High Chemical Stability of the Chromophore. Rao J, ed. *PLoS One.* 2011;6(12):e28674. doi:10.1371/journal.pone.0028674.
60. Goedhart J, von Stetten D, Noirclerc-Savoye M, et al. Structure-guided evolution of cyan fluorescent proteins towards a quantum yield of 93%. *Nat Commun.* 2012;3:751. doi:10.1038/ncomms1738.
61. Markwardt ML, Kremers G-J, Kraft CA, et al. An improved cerulean fluorescent protein with enhanced brightness and reduced reversible photoswitching. *PLoS One.* 2011;6(3):e17896. doi:10.1371/journal.pone.0017896.

62. Heim R, Prasher DC, Tsien RY. Wavelength mutations and posttranslational autoxidation of green fluorescent protein. *Proc Natl Acad Sci U S A*. 1994;91(26):12501-12504.
63. Heim R, Tsien RY. Engineering green fluorescent protein for improved brightness, longer wavelengths and fluorescence resonance energy transfer. *Curr Biol*. 1996;6(2):178-182.
64. Rose RC, Bode AM. Ocular ascorbate transport and metabolism. *Comp Biochem Physiol A Comp Physiol*. 1991;100(2):273-285.
65. Cubitt AB, Woollenweber LA, Heim R. Understanding structure-function relationships in the *Aequorea victoria* green fluorescent protein. *Methods Cell Biol*. 1999;58:19-30.
66. Cormack BP, Valdivia RH, Falkow S. FACS-optimized mutants of the green fluorescent protein (GFP). *Gene*. 1996;173(1 Spec No):33-38.
67. Lam AJ, St-Pierre F, Gong Y, et al. Improving FRET dynamic range with bright green and red fluorescent proteins. *Nat Methods*. 2012;9(10):1005-1012. doi:10.1038/nmeth.2171.
68. Ormö M, Cubitt AB, Kallio K, Gross LA, Tsien RY, Remington SJ. Crystal structure of the *Aequorea victoria* green fluorescent protein. *Science*. 1996;273(5280):1392-1395.
69. Nagai T, Ibata K, Park ES, Kubota M, Mikoshiba K, Miyawaki A. A variant of yellow fluorescent protein with fast and efficient maturation for cell-biological applications. *Nat Biotechnol*. 2002;20(1):87-90. doi:10.1038/nbt0102-87.
70. Griesbeck O, Baird GS, Campbell RE, Zacharias DA, Tsien RY. Reducing the environmental sensitivity of yellow fluorescent protein. Mechanism and applications. *J Biol Chem*. 2001;276(31):29188-29194. doi:10.1074/jbc.M102815200.
71. Shaner NC, Lin MZ, McKeown MR, et al. Improving the photostability of bright monomeric orange and red fluorescent proteins. *Nat Methods*. 2008;5(6):545-551. doi:10.1038/nmeth.1209.
72. Shcherbakova DM, Hink MA, Joosen L, Gadella TWJ, Verkhusha V V. An orange fluorescent protein with a large Stokes shift for single-excitation multicolor FCCS and FRET imaging. *J Am Chem Soc*. 2012;134(18):7913-7923. doi:10.1021/ja3018972.
73. Shaner NC, Campbell RE, Steinbach PA, Giepmans BNG, Palmer AE, Tsien RY. Improved monomeric red, orange and yellow fluorescent proteins derived from *Discosoma* sp. red fluorescent protein. *Nat Biotechnol*. 2004;22(12):1567-1572. doi:10.1038/nbt1037.
74. Shcherbo D, Murphy CS, Ermakova G V, et al. Far-red fluorescent tags for protein imaging in living tissues. *Biochem J*. 2009;418(3):567-574. doi:10.1042/BJ20081949.
75. Chu J, Haynes RD, Corbel SY, et al. Non-invasive intravital imaging of cellular differentiation with a bright red-excitable fluorescent protein. *Nat Methods*. 2014;11(5):572-578. doi:10.1038/nmeth.2888.
76. Filonov GS, Piatkevich KD, Ting L-M, Zhang J, Kim K, Verkhusha V V. Bright and stable near-infrared fluorescent protein for in vivo imaging. *Nat Biotechnol*. 2011;29(8):757-761. doi:10.1038/nbt.1918.
77. Wachter RM, Remington SJ. Sensitivity of the yellow variant of green fluorescent protein to halides and nitrate. *Curr Biol*. 1999;9(17):R628-9.

78. Gurskaya NG, Verkhusha V V, Shcheglov AS, et al. Engineering of a monomeric green-to-red photoactivatable fluorescent protein induced by blue light. *Nat Biotechnol.* 2006;24(4):461-465. doi:10.1038/nbt1191.
79. McKinney SA, Murphy CS, Hazelwood KL, Davidson MW, Looger LL. A bright and photostable photoconvertible fluorescent protein. *Nat Methods.* 2009;6(2):131-133. doi:10.1038/nmeth.1296.
80. Habuchi S, Tsutsui H, Kochaniak AB, Miyawaki A, van Oijen AM. mKikGR, a monomeric photoswitchable fluorescent protein. *PLoS One.* 2008;3(12):e3944. doi:10.1371/journal.pone.0003944.
81. Subach F V, Patterson GH, Renz M, Lippincott-Schwartz J, Verkhusha V V. Bright monomeric photoactivatable red fluorescent protein for two-color super-resolution sptPALM of live cells. *J Am Chem Soc.* 2010;132(18):6481-6491. doi:10.1021/ja100906g.
82. Wachter RM, James Remington S. Sensitivity of the yellow variant of green fluorescent protein to halides and nitrate. *Curr Biol.* 1999;9(17):R628-R629. doi:10.1016/S0960-9822(99)80408-4.
83. Carpenter AE, Jones TR, Lamprecht MR, et al. CellProfiler: image analysis software for identifying and quantifying cell phenotypes. *Genome Biol.* 2006;7(10):R100. doi:10.1186/gb-2006-7-10-r100.
84. Lowe DG. Distinctive Image Features from Scale-Invariant Keypoints. *Int J Comput Vis.* 2004;60(2):91-110. doi:10.1023/B:VISI.0000029664.99615.94.
85. Vedaldi A, Fulkerson B. Vlfeat. In: *Proceedings of the International Conference on Multimedia - MM '10.* New York, New York, USA: ACM Press; 2010:1469. doi:10.1145/1873951.1874249.
86. English BP, Singer RH. A three-camera imaging microscope for high-speed single-molecule tracking and super-resolution imaging in living cells. In: Mohseni H, Agahi MH, Razeghi M, eds. *SPIE Nanoscience + Engineering.* International Society for Optics and Photonics; 2015:955008. doi:10.1117/12.2190246.
87. Edelstein A, Amodaj N, Hoover K, Vale R, Stuurman N. Computer control of microscopes using μ Manager. *Curr Protoc Mol Biol.* 2010;Chapter 14:Unit14.20. doi:10.1002/0471142727.mb1420s92.
88. Dedecker P, Duwé S, Neely RK, Zhang J. Localizer: fast, accurate, open-source, and modular software package for superresolution microscopy. *J Biomed Opt.* 2012;17(12):126008. doi:10.1117/1.JBO.17.12.126008.
89. Mortensen KI, Churchman LS, Spudich JA, Flyvbjerg H. Optimized localization analysis for single-molecule tracking and super-resolution microscopy. *Nat Methods.* 2010;7(5):377-381. doi:10.1038/nmeth.1447.
90. Femino AM, Fay F, Fogarty K, Singer R. Visualization of Single RNA Transcripts *in situ*. *Science (80-).* 1998;280(5363):585-590. doi:10.1126/science.280.5363.585.
91. Levsky JM, Singer RH. Fluorescence *in situ* hybridization: past, present and future. *J Cell Sci.* 2003;116(Pt 14):2833-2838. doi:10.1242/jcs.00633.
92. Raj A, van den Bogaard P, Rifkin SA, van Oudenaarden A, Tyagi S. Imaging individual

- mRNA molecules using multiple singly labeled probes. *Nat Methods*. 2008;5(10):877-879. doi:10.1038/nmeth.1253.
93. Choi HMT, Beck VA, Pierce NA. Next-generation *in situ* hybridization chain reaction: Higher gain, lower cost, greater durability. *ACS Nano*. 2014;8(5):4284-4294. doi:10.1021/nn405717p.
 94. Cajigas IJ, Tushev G, Will TJ, Tom Dieck S, Fuerst N, Schuman EM. The Local Transcriptome in the Synaptic Neuropil Revealed by Deep Sequencing and High-Resolution Imaging. *Neuron*. 2012;74(3):453-466. doi:10.1016/j.neuron.2012.02.036.
 95. Wang F, Flanagan J, Su N, et al. RNAscope: A novel *in situ* RNA analysis platform for formalin-fixed, paraffin-embedded tissues. *J Mol Diagnostics*. 2012;14(1):22-29. doi:10.1016/j.jmoldx.2011.08.002.
 96. Tillberg PW, Chen F, Piatkevich KD, et al. Expansion Microscopy of Biological Specimens with Protein Retention.
 97. Chozinski TJ, Halpern AR, Okawa H, et al. Expansion microscopy with conventional antibodies and fluorescent proteins. *Nat Methods*. 2016;(April):1-7. doi:10.1038/nmeth.3833.
 98. Engreitz JM, Pandya-Jones A, McDonel P, et al. The Xist lncRNA exploits three-dimensional genome architecture to spread across the X chromosome. *Science*. 2013;341(6147):1237973. doi:10.1126/science.1237973.
 99. Panning B, Dausman J, Jaenisch R. X chromosome inactivation is mediated by Xist RNA stabilization. *Cell*. 1997;90(5):907-916.
 100. Plath K, Mlynarczyk-Evans S, Nusinow DA, Panning B. Xist RNA and the mechanism of X chromosome inactivation. *Annu Rev Genet*. 2002;36:233-278. doi:10.1146/annurev.genet.36.042902.092433.
 101. Mito M, Kawaguchi T, Hirose T, Nakagawa S. Simultaneous multicolor detection of RNA and proteins using super-resolution microscopy. *Methods*. November 2015. doi:10.1016/j.ymeth.2015.11.007.
 102. Clemson CM, Hutchinson JN, Sara SA, et al. An architectural role for a nuclear noncoding RNA: NEAT1 RNA is essential for the structure of paraspeckles. *Mol Cell*. 2009;33(6):717-726. doi:10.1016/j.molcel.2009.01.026.
 103. Lieberman-Aiden E, van Berkum NL, Williams L, et al. Comprehensive mapping of long-range interactions reveals folding principles of the human genome. *Science*. 2009;326(5950):289-293. doi:10.1126/science.1181369.
 104. Lubeck E, Cai L. Single-cell systems biology by super-resolution imaging and combinatorial labeling. *Nat Methods*. 2012;9(7):743-748. doi:10.1038/nmeth.2069.
 105. Lubeck E, Coskun AF, Zhiyentayev T, Ahmad M, Cai L. Single-cell *in situ* RNA profiling by sequential hybridization. *Nat Methods*. 2014;11:360-361. doi:10.1038/nmeth.2892.
 106. Chen KH, Boettiger AN, Moffitt JR, Wang S, Zhuang X. Spatially resolved, highly multiplexed RNA profiling in single cells. *Science (80-)*. 2015;348(6233):aaa6090-aaa6090. doi:10.1126/science.aaa6090.
 107. Beliveau BJ, Joyce EF, Apostolopoulos N, et al. Versatile design and synthesis platform

- for visualizing genomes with Oligopaint FISH probes. *Proc Natl Acad Sci U S A*. 2012;109:21301-21306. doi:10.1073/pnas.1213818110.
108. Lein ES, Hawrylycz MJ, Ao N, et al. Genome-wide atlas of gene expression in the adult mouse brain. *Nature*. 2007;445(7124):168-176. doi:10.1038/nature05453.
 109. Batish M, van den Bogaard P, Kramer FR, Tyagi S. Neuronal mRNAs travel singly into dendrites. *Proc Natl Acad Sci*. 2012;109(12):4645-4650. doi:10.1073/pnas.1111226109.
 110. Cabili MN, Dunagin MC, McClanahan PD, et al. Localization and abundance analysis of human lncRNAs at single-cell and single-molecule resolution. *Genome Biol*. 2015;16:20. doi:10.1186/s13059-015-0586-4.
 111. Zhang DY, Seelig G. Dynamic DNA nanotechnology using strand-displacement reactions. *Nat Chem*. 2011;3(2):103-113. doi:10.1038/nchem.957.
 112. Lee JH, Daugharthy ER, Scheiman J, et al. Highly Multiplexed Subcellular RNA Sequencing *in situ*. *Science (80-)*. 2014;343(6177):1360-1363. doi:10.1126/science.1250212.
 113. Ke R, Mignardi M, Pacureanu A, et al. *In situ* sequencing for RNA analysis in preserved tissue and cells. *Nat Methods*. 2013;10(9):857-860. doi:10.1038/nmeth.2563.
 114. Bruchez M, Moronne M, Gin P, et al. Semiconductor nanocrystals as fluorescent biological labels. *Science*. 1998;281(5385):2013-2016. doi:10.1126/science.281.5385.2013.
 115. Fouz MF, Mukumoto K, Averick S, et al. Bright Fluorescent Nanotags from Bottlebrush Polymers with DNA-Tipped Bristles. *ACS Cent Sci*. 2015;1(8):431-438. doi:10.1021/acscentsci.5b00259.
 116. Steward O, Wallace CS, Lyford GL, Worley PF. Synaptic activation causes the mRNA for the leg Arc to localize selectively near activated postsynaptic sites on dendrites. *Neuron*. 1998;21(4):741-751. doi:10.1016/S0896-6273(00)80591-7.
 117. Buckley PT, Lee MT, Sul JY, et al. Cytoplasmic Intron Sequence-Retaining Transcripts Can Be Dendritically Targeted via ID Element Retrotransposons. *Neuron*. 2011;69(5):877-884. doi:10.1016/j.neuron.2011.02.028.
 118. Steward O, Schuman EM. Compartmentalized synthesis and degradation of proteins in neurons. *Neuron*. 2003;40(2):347-359. doi:10.1016/S0896-6273(03)00635-4.
 119. Buxbaum AR, Wu B, Singer RH. Single -Actin mRNA Detection in Neurons Reveals a Mechanism for Regulating Its Translatability. *Science (80-)*. 2014;343(6169):419-422. doi:10.1126/science.1242939.
 120. Jung H, Yoon BC, Holt CE. Axonal mRNA localization and local protein synthesis in nervous system assembly, maintenance and repair. *Nat Rev Neurosci*. 2012;13(5):308-324. doi:10.1038/nrn3210.
 121. Raj A, Tyagi S. *Detection of Individual Endogenous RNA Transcripts in situ Using Multiple Singly Labeled Probes*. Vol 472. 1st ed. Elsevier Inc.; 2010. doi:10.1016/S0076-6879(10)72004-8.
 122. Schindelin J, Arganda-Carreras I, Frise E, et al. Fiji: an open-source platform for biological-image analysis. *Nat Methods*. 2012;9(7):676-682. doi:10.1038/nmeth.2019.

123. Thévenaz P, Ruttimann UE, Unser M. A pyramid approach to subpixel registration based on intensity. *IEEE Trans Image Process.* 1998;7(1):27-41. doi:10.1109/83.650848.